Editorial corner – a personal view
The way to autonomic self-healing polymers and composites

*A. Pegoretti**

Department of Materials Engineering and Industrial Technologies, University of Trento, via Mesiano 77, 38100 Trento, Italy

Low-velocity impacts on fibre reinforced polymer composites may cause irreversible damages such as surface scratches, micro cracks or small internal flaws that can seriously impair the load carrying ability of structural components. In fact, these cracks can grow under subcritical loading conditions (such as fatigue or creep) and ultimately lead to failure. Repairing these small damages is often a difficult task since it requires non-destructive inspections an intervention under maintenance procedures. A big challenge for polymer scientists and engineers is to develop new polymeric matrices having the built-in ability to partially repair damages occurring during its service life time. An ideal self-healing polymer is able, after having been damaged, to autonomously restore its initial mechanical performances without the need of external stimuli like temperature, radiation, pressure, etc. This process is quite common in nature, since damage to a living tissue generally elicits a healing response.

Self-healing applied to thermosetting matrices and composites is an emerging area of research, with the first significant papers being published in early 2000's and with the 1st International Conference on Self-Healing Materials organized by the Delft University of Technology (NL) in 2007. The first report of a man-made self healing polymer was by the group of prof Scott White of the University of Illinois at Urbana-Champaign. They developed an epoxy system containing microcapsules filled with a healing agent (liquid monomer). When a crack propagates, the microcapsule will rupture, the monomer will fill the crack and eventually undergo a polymerisation process, initiated by (Grubbs') catalyst particles dispersed in the system. This model system proved to work quite well, as the service life time of such material under fatigue conditions is significantly improved. On the other hand, it also presents a number of drawbacks related to the Grubbs' catalyst (high cost, partial deactivation by the amine curing agent, decomposition above 120°C) and to the stability of the microcapsules (diffusion and leakage of the healing agent, decomposition of the capsules above 170°C). A number of research groups world wide is trying to improve the microencapsulation-based approach or to develop new approaches to self-healing. A possible alternative strategy is based on the development of reversible crosslinked polymers through self-assembly chemistry in which the material is repaired by the re-association of the self-assemblable bonds broken by the crack.

At a present, there are no commercially available products having a self-healing ability and the challenge for materials scientists and engineers is fascinating.

Prof. Dr. Alessandro Pegoretti
Member of International Advisory Board

*Corresponding author, e-mail: alessandro.pegoretti@unitn.it

Modelling tensile force oscillation during the tensile test of PET specimens

L. M. Vas, F. Ronkay*, T. Czigány

Department of Polymer Engineering, Faculty of Mechanical Engineering, Budapest University of Technology and Economics, Műegyetem rkp. 3. Budapest H-1111, Hungary

Abstract. Force oscillation occurring during the tensile testing of poly(ethylene terephthalate) (PET), resulting in periodical cavitation of the test specimens, has been studied. A mathematical model has been developed to describe the phenomenon, wherein special fibre bundles are assigned to the amorphous molecular chains. In order to model the local periodical transformations and the rate dependent viscoelastic behaviour the coupled fibre bundle cells were supplemented with a two-element Maxwell model. Using the parameters determined from the measurements the model was compared to the measured force-elongation diagrams and it has been concluded that the simple model can be well used to describe the phenomenon.

Keywords: modelling and simulation, stress oscillation, viscoelastic properties

1. Introduction

The viscoelastic properties of the polymers have been widely studied [1]. Recently its modelling also came to the front [2]. Stress oscillation occurring during the tensile testing of poly(ethylene terephthalate) (PET) – also denoted as self-oscillation – was described first in 1970, in conjunction with necking induced by the static loading of amorphous PET [3]. Stress oscillation means that under certain conditions the stress arising during necking is not constant anymore, but exhibits a periodic fluctuation vs. time [4]. The reasons of stress oscillation have not been clarified in the literature and are hotly debated [5]. Among possible explanations one can find local heating caused by orientational elongation [6–10]; oscillation of local deformation rate during necking within a critical stress range [11]; orientation crystallization induced by adiabatic heat formation [12].

Karger-Kocsis *et al.* [13, 14] studied the oscillation phenomenon in sPP. In their opinion necking, which is a prerequisite of stress oscillation in any polymer, produces an elongated, random network. This network closely resembles partially crystalline thermoplastic elastomers. The deformation of this complex system is strongly inhomogeneous. This, by itself, induces a shear deformation process. According to their explanation, when some small crystallites disintegrate during the tensile elongation the shear deformation is amplified further and cavities are formed at the crossing of shear bands. If the density of micro-waves of crossings reaches a critical value the material is weakened and its load-bearing capacity drops because of the abrupt cavitation. This explains the stress drop in the amplitude of stress oscillation. According to this explanation shear bands cannot easily cross each other on the sample surface, which is in agreement with

the experimental observation that cavities always appear inside the test specimen.

According to Ebener *et al.* [15] oscillation arises if the test specimen can store enough elastic energy. For this the initial length of the test specimen should be large enough. Elastic energy storage-capacity can also be achieved by the application of an external spring. According to his measurements, if the deformation rate is increased during the oscillation, the mean stress and the amplitude decrease, while local heat removal results in the increase of the mean stress. In his opinion during the deformation – a high degree of orientation occurs and heat is released – the polymer may crystallize partially in both the transparent and non-transparent parts. As the local deformation rate is higher during the formation of the non-transparent bands, crystallization is easier here. Not all non-transparent bands were found, however, to be partially crystalline.

In our earlier study [16] we traced back the origin of the oscillation to the cavitation of the test specimen. We observed that the cavitation occurs simultaneously with the stress oscillation, in a periodic manner, before reaching the stress peaks. Due to the formation of the cavities the heat conductivity of the material decreases considerably, the temperature of the deformation zone increases abruptly (with 36–40°C), resulting in a drop of the strength and in elongation. During neck propagation, however, the material cools down, the strength increases again, so the process becomes periodical. Our conclusions were corroborated by SEM (scanning electron microscopy) and AE (acoustic emission) measurements. In order to describe the phenomenon a physical model was constructed, which traces back the phenomenon to changes of the molecular structure. According to this model shear forces arise between the molecular chains orienting under the effect of stress and, as a result, the material splits into molecular bundles. Ordering of the molecules into bundles is accompanied by significant crystallization. Micro-cracks (crazes) between the bundles decrease the heat conductivity of the material considerably and this leads to local heating.

In this article the changes in the orientation of the molecular chains are modelled by fibre bundles. Fibres of a bundle consisting of partially ordered, homogeneous (uniform) fibres can be classified according to their initial state and according to the properties of their environment. Fibres belonging to the same class form a partial bundle, a so-called fibre bundle cell. In this article a pre-stressed, breaking fibre bundle (so-called EH bundle) is used [17, 18], with independent fibres, the strings defined by the clamping points are well ordered, but the individual fibres may be either pre-stressed with a statistically variable ε_0 elongation ($\varepsilon_0 > 0$), or may be loose, i.e. crimped ($-1 < \varepsilon_0 < 0$). In order to describe the viscoelastic behaviour of the test specimen a two-element Maxwell model is used [19].

The main goal of this study is to develop a simple mathematical model to describe the force-elongation curve. Aim was to model two phenomena known and explained: 1. Oscillation occurs just over a strain rate; 2. Oscillation is connected with forming crazes where amorphous molecular chains like fibres get stressed/strained and create bundles of chains and voids among them.

2. Experimental results

2.1. Material and equipment

In our experiments standard 'dumb-bell' specimens were injection molded from PET (SkyPET-BL 8050, SK Chemicals) pellets using an Arburg All-rounder 270C injection moulding machine. Zone temperatures of the injection moulding machine were: 235/240/245/250/255°C, injection pressure was 500 bar. The mould was cooled by 15°C water. Tensile testing of the specimens was performed by a Zwick Z020 universal tensile tester at room temperature. Cavities and crazing appearing in the material were studied by a JEOL JSM 6380LA electron microscope.

2.2. Measurements

Tensile tests were performed at a tensile rate of 60 mm/min, the initial gauge length of the test specimens was 115 mm. Tensile curve shown in Figure 1 was obtained during the test. As shown by the figure, after a uniform neck propagation an oscillation of about constant amplitude (5.8 MPa) and cycle time (1.14 s) appears in the stress. The lower limiting value of the oscillation is 21.2 MPa, its upper limiting value is 27 MPa. The slope of the
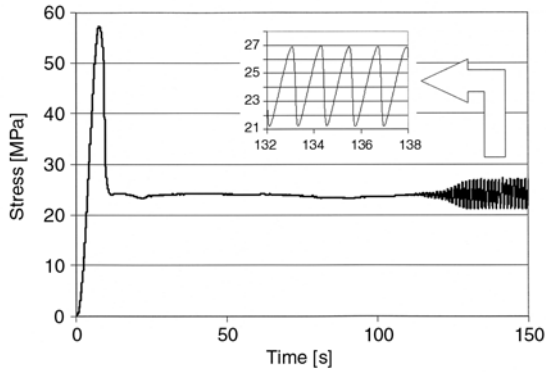
Figure 1. Tensile curve of PET at a tensile rate of 60 mm/s
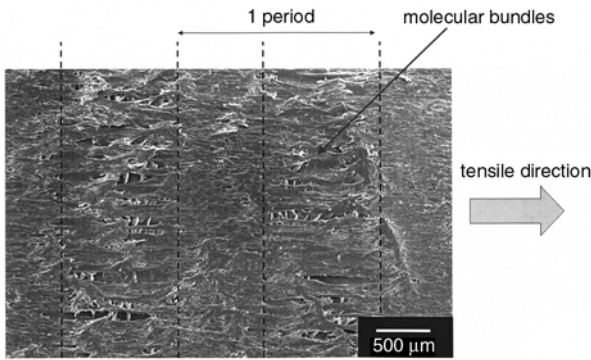

Figure 2. SEM micrograph of the longitudinal section of the specimen

tangent at the initial portion of the curve is 4.5 MPa/s, in the initial portions of the oscillating period it is, however, 6 MPa/s.

Figure 2 shows the longitudinal section of a specimen which has undergone oscillation. One can see that the cavitation occurs periodically. Between the cavities parallel with the load molecular bundles can be observed with a thickness between 10 and 150 µm. The bands perpendicular to the tensile elongation without cavities are formed during the increasing stress interval of the stress oscillation period, while the bands containing cavities are formed during the stress drop interval.

3. Modelling the force oscillation and discussion

Based on the tensile tests of PET specimens the force oscillation appears only after the initiation of necking, above a certain tensile rate, indicating a load peak, therefore it can be characterized by a critical stress (σ_{crit}). When neglecting the initial load peak the force-elongation curve increases monotonously. Two forms of this is shown in Fig-
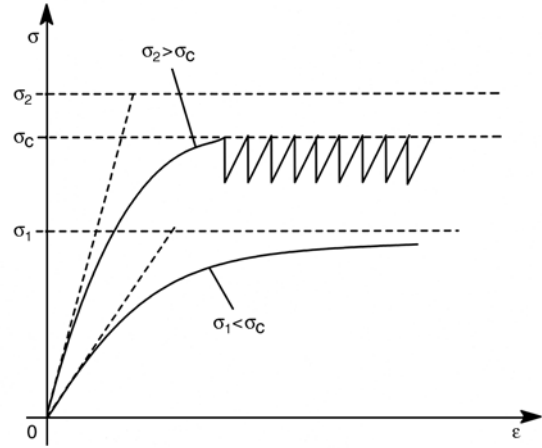

Figure 3. Force responses to be modelled

ure 3. In one case the asymptotic stress (σ_1) is less than $\sigma_c = \sigma_{crit}$ therefore oscillation does not take place. In the other case this stress (σ_2) is exceed σ_{crit} hence reaching σ_{crit} the oscillation starts.

Based on these an analogous mechanical model was developed in order to describe mathematically the characteristics and the force oscillation shown in Figure 1 and to study the phenomenon analytically.

3.1. Mechanical model

As shown by the experiments crazing and void formation occurs periodically. It means that the molecular chains in the amorphous phase assemble into micro-bundles in front of the deformation zones forming voids, some of which may develop into macro-cavities. Amorphous chains can be considered as part of an EH type fibre bundle [17, 18] consisting of crimped fibres which are perfectly flexible and do not transmit tensile force while being crimped (Figure 4).

It is assumed that the EH bundle cell is enclosed into a rigid box which remains intact until exposed to a critical force level. Then the box opens and extends telescopically, but a force is transmitted only when the fibres are straightened (see Figure 4). For the sake of simplicity let us consider the
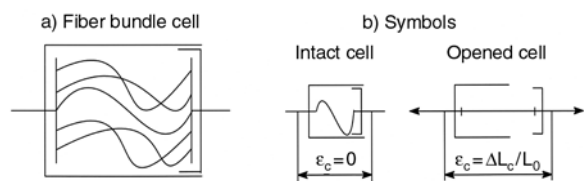

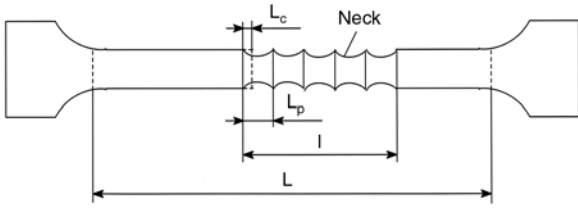**Figure 4.** Fiber bundle cell and its symbols in intact and opened states
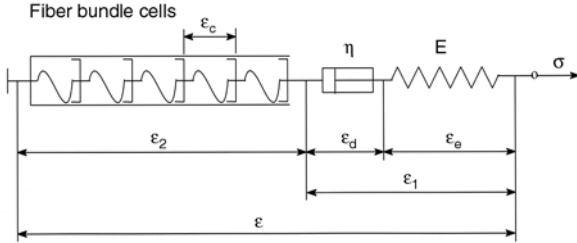
Figure 5. Specimen with neck periods

Figure 6. Analogous mechanical model

fibres as inextensible, the boxes as rigid and the level of crimping uniform. In this case the deformation of the intact cell is zero, while that of the opened cell is described in Equation (1):

$$\varepsilon_c = \frac{\Delta L_c}{L_0} = \frac{L_p - L_c}{L_0} = \frac{L_p - L_p(1 + \varepsilon_{f_0})}{L_0} = -\varepsilon_{f_0}\frac{L_p}{L_0} \quad (1)$$

where L_0 is the gauge length of the test specimen, L_c and L_p are the lengths of the intact and open cells respectively, $\varepsilon_{f_0} < 0$ is the crimping of the fibres (see Figure 5). Note that L_p is a kind of period length measurable on the neck.

In order to model the periodical local transitions and the viscoelastic rate-dependent behaviour of the specimen a stiff box containing a number of serially connected fibre bundle cells and a two-element Maxwell model [19] are used, respectively (see Figure 6).

3.2. Force oscillation response

Modelling the tensile test the constant rate elongation of the model shown in Figure 6 is described with Equation (2):

$$u(t) = \varepsilon(t) = \frac{L - L_0}{L_0} = \frac{\Delta L}{L_0} = \frac{vt}{L_0} = \dot{\varepsilon}_0 t \quad (2)$$

where u is the relative extension of the specimen measured between the grips and $\dot{\varepsilon}_0$ is the strain rate. The response of the model changes in time intervals because the fibre cells open one after another

periodically causing jump-like drops in the force. The strain rate is equal to $\dot{u}$, the rate of extension of the specimen measured between the grips, as described in Equation (3):

$$\dot{u} = \dot{\varepsilon}_0 = \frac{v}{L_0} \quad (3)$$

where v and L_0 are the speed of the moving grip and the gauge length of the specimen, respectively.

In the first time interval up to the first load peak $(0 \le t \le t_1)$ every cell is closed, hence only the spring $(E = E_0)$ and the dashpot $(\eta = \eta_0)$ of the Maxwell model deform (Figure 6: $\varepsilon_2 = 0$, $\varepsilon = \varepsilon_1$), which can be described by Equation (4):

$$\dot{\varepsilon} = \frac{\dot{\sigma}}{E_0} + \frac{\sigma}{\eta_0} \quad (4)$$

The general solution of Equation (4) for a stimulus according to Equation (2) can be derived easily in Equation (5):

$$\sigma(t) = \sigma(0)e^{-t/\tau_0} + E_0\dot{\varepsilon}_0\tau_0(1 - e^{-t/\tau_0})\xrightarrow[t \to \infty]{}$$

$$E_0\dot{\varepsilon}_0\tau_0 = \eta_0\dot{\varepsilon}_0 = \sigma_{Lim} \quad (5)$$

which tends to a constant stress value (σ_{Lim}), where τ_0 is a time constant, which is described by Equation (6):

$$\tau_0 = \frac{\eta_0}{E_0} \quad (6)$$

Supposing that $\sigma(0) = 0$, the stress-strain relationship for the first interval $(0 \le t \le t_1)$ is given by Equation (7):

$$\sigma(t) = E_0\dot{\varepsilon}_0\tau_0(1 - e^{-t/\tau_0}) \quad (7)$$

The initial slope in this interval depends on the strain rate and is described by Equation (8):

$$\dot{\sigma}(0) = E_0\dot{\varepsilon}_0 = \dot{\sigma}_0 \quad (8)$$

Consequently, increasing the strain rate increases both the initial slope ($\dot{\sigma}_0$) and the asymptotic stress value (σ_{Lim}), therefore, if the strain rate is large enough the stress reaches the critical stress in a finite time $(0 < t_1 < \infty)$ (Equation (9)):
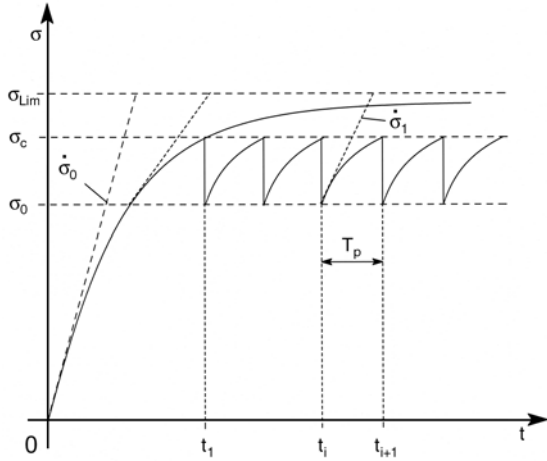
$$\sigma(t_1) = \sigma_{crit} \quad (9)$$

Figure 7. Model response

Reaching the critical stress at time point t_1 the first fibre cell opens and the strain of the spring decreases suddenly by ε_c, up to the entire straightening of the fibres ($\varepsilon_e(t_1) > \varepsilon_c$), and the stress drops to σ_0 (Figure 7). In the real PET material a neck forms at the first force peak, where the extension is cumulated, the strain becomes essentially localized, hence the strain rate increases: $\dot{\varepsilon}_1 > \dot{\varepsilon}_0$. Hence, if the length of the neck formed at t_1 is l_1, and assuming that the local extension (Δl) in the (t_1, $t_1+\Delta t$) interval is equal to that of the specimen or the entire model (ΔL_1), i.e. if the extension of the propagating neck outside of the given section is negligible, which is described in Equation (10):

$$\Delta l = l - l_1 = \Delta L_1 = L - L_1 = v\Delta t \tag{10}$$

where $L_1 = L(t_1)$. Accordingly the local strain and strain rate are (see Figure 6) described in Equations (11) and (12):

$$\Delta\varepsilon_1 = \frac{\Delta l}{l_1} = \frac{v}{l_1}\Delta t = \dot{\varepsilon}_1\Delta t \tag{11}$$

$$\dot{\varepsilon}_1 = \frac{v}{l_1} = \frac{v}{L_0}\frac{L_0}{l_1} = \dot{\varepsilon}_0\frac{L_0}{l_1} > \dot{\varepsilon}_0 \tag{12}$$

As another consequence a kind of hardening takes place because of the increase in the orientation. Therefore, in an analogous way, the model parameters are supposed to change as well: $E = E_1$ and $\eta = \eta_1$.

On the basis of the considerations above Equation (13) is valid for the second time interval ($t_1 < t \leq t_2$):

$$\dot{\varepsilon}_1 = \frac{\dot{\sigma}}{E_1} + \frac{\sigma}{\eta_1} \tag{13}$$

The general solution of Equation (13) is in Equation (14), which is similar to that of Equation (5):

$$\sigma(t) = \sigma(t_1+0)e^{-(t-t_1)/\tau_1} + E_1\dot{\varepsilon}_1\tau_1(1-e^{-(t-t_1)/\tau_1}) \xrightarrow[t\to\infty]{}$$

$$E_1\dot{\varepsilon}_1\tau_1 = \eta_1\dot{\varepsilon}_1 = \sigma_{Lim_1} \tag{14}$$

where τ_1 is a new time constant (Equation (15)):

$$\tau_1 = \frac{\eta_1}{E_1} \tag{15}$$

Here $\sigma(t_1+0) = \sigma_0$, hence the stress-strain relationship and the initial slope for the second interval ($t_1 < t \leq t_2$) are given by Figure 7 and it is described in Equations (16) and (17):

$$\sigma(t) = \sigma_0 e^{-(t-t_1)/\tau_1} + E_1\dot{\varepsilon}_1\tau_1(1-e^{-(t-t_1)/\tau_1}) \tag{16}$$

$$\dot{\sigma}(t_1+0) = E_1\dot{\varepsilon}_1 - \frac{\sigma_0}{\tau_1} = \dot{\sigma}_1 \tag{17}$$

It can be assumed that the phenomena in the next and further intervals are similar to those in the second interval, consequently the force process is periodical.

3.3. Method of determining the model parameters

Pre-set data of the tensile test are L_0 and v. From measurements performed on the PET specimens the following data can be determined directly: σ_{crit}, σ_0, $\dot{\sigma}_0$, $\dot{\sigma}_1$, $\dot{\varepsilon}_0$, $\dot{\varepsilon}_1$, l_0, t_1, …, t_n, and T_p (see Table 1). Model parameters, such as E_0, E_1, η_0, η_1, ε_c and ε_{f_0} can be calculated from Equation (1–17).

If σ_0 is known E_0 can be determined from Equation (8) and solving the Equation (18) τ_0 can be obtained:

$$\sigma_{crit} = E_0\dot{\varepsilon}_0\tau_0(1-e^{-t_1/\tau_0}) \tag{18}$$

and from Equation (6) η_0 can be calculated. Equation (19) is given by Equation (16) for the ($i+1$)-th time interval at t_{i+1}:

Table 1. Test results

v	L_0	σ_{crit}	σ_0	$\dot{\sigma}_0$	$\dot{\sigma}_1$	σ_{lim}
[mm/min]	[mm]	[MPa]	[MPa]	[MPa/s]	[MPa/s]	[MPa]
60	115	27	21.1	4.5	7.2	36.3

$\dot{\varepsilon}_0$	$\dot{\varepsilon}_1$	l_1	L_c	L_p	t_1	T_p
[1/s]	[1/s]	[mm]	[mm]	[mm]	[s]	[s]
0.01	0.04	26	0.02	1.32	9.24	1.14

Table 2. Parameters obtained by model fitting

E_0	E_1	η_0	η_1	ε_c	ε_{f_0}	τ_0	τ_1
[MPa]	[MPa]	[MPas]	[MPas]	[–]	[–]	[s]	[s]
483.0	523.8	4174.5	853.7	0.01	–0.98	8.64	1.63
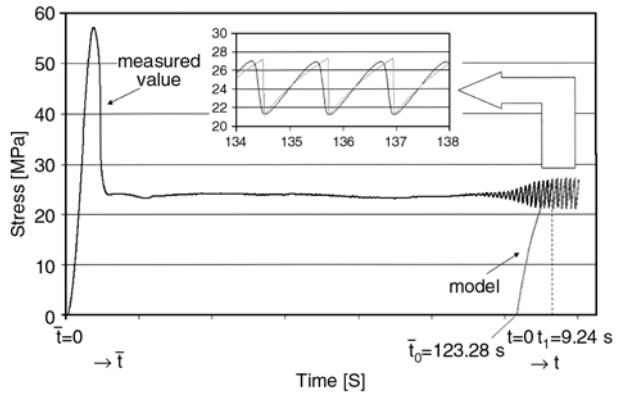
Figure 8. Comparison of the measured values and the model

$$\sigma_{crit} = \sigma_0 e^{-(t_{i+1}-t_1)/\tau_1} + E_1 \dot{\varepsilon}_1 \tau_1 (-e^{-(t_{i+1}-t_1)/\tau_1}) \qquad (19)$$

Equation (20) is given by expressing E_1 form Equation (17) and substituting into Equation (16) and taking into consideration that $T_p = t_{i+1} - t_i$:

$$\sigma_{crit} = \sigma_0 e^{-T_p/\tau_1} + (\dot{\sigma}_1 \tau_1 + \sigma_0)(1-e^{-T_p/\tau_1}) \qquad (20)$$

Solving Equation (20) τ_1 is obtained, then from Equation (15) and (17) η_1 and E_1 can be calculated respectively. Finally, the negative strain (ε_c) stored as crimping or loosening in the fiber cells can be calculated in the Equation (21):

$$\sigma_{crit} - \sigma_0 = E_1 \varepsilon_c \rightarrow \varepsilon_c = \frac{\sigma_{crit} - \sigma_0}{E_1} \qquad (21)$$

The length of the L_p period can be measured on the neck, therefore the length of the intact cell (L_c) and the fibre crimping (ε_{f_0}), as a negative strain can be determined from Equations (22) and (23):

$$L_c = L_p - \varepsilon_c L_0 \qquad (22)$$

$$\varepsilon_{f_0} = -\varepsilon_c \frac{L_0}{L_p} \qquad (23)$$

As a cross-check it is worth to calculate the cycle time from Equation (20) and to compare it with the measured value in Equation (24):

$$T_p = t_{i+1} - t_i = \tau_1 \ln \frac{\eta_1 \dot{\varepsilon}_1 - \sigma_0}{\eta_1 \dot{\varepsilon}_1 - \sigma_{crit}} =$$
$$\tau_1 \ln \frac{\dot{\sigma}_1 \tau_1}{\dot{\sigma}_1 \tau_1 + \sigma_0 - \sigma_{crit}} \qquad (24)$$

Substituting the model parameters calculated from the measured data (Table 2) into the equations above the oscillation curve predicted by the model is obtained.

Figure 8 compares the measured tensile curve with the points predicted by the model. As the model describes only the established oscillation, a better picture is obtained if the curve starts not in the true $t = 0$ origin, but only immediately before the onset of the oscillation. As shown by Figure 8 the amplitude and frequency of the model curve are exactly identical with the corresponding values of the observed stress oscillation. The shape disagreement between the two curves is due to the fact that in the fibre bundle cells in the simplified model contain only idealized, inextensible fibres of uniform crimping, not real fibre bundles containing fibres of variable crimping, which would round off the sharp peaks of the curves.

4. Conclusions

Stress oscillation occurring during the tensile test of PET has been studied and modelled. A mathematical model was created to describe the oscillation. The amorphous molecular chains were described as apart of modelling by special EH-type fibre bundles containing crimped fibres enclosed into rigid boxes. These boxes open up at a certain critical force value, when the crimped fibres straighten and begin to bear the load. In order to model the periodic local transformation and the rate-dependent viscoelastic behaviours of the test specimens the connected fibre bundle cells were supplemented by a two-element Maxwell model.

Using the parameters determined from the measurements the model was compared to the real tensile curve and concluded that simple model can be well used to describe the phenomenon.

Acknowledgements

References

[1] Nagy P., Vas L. M.: Relationship between constant strain rate and stress relaxation behavior of polypropylene. Express Polymer Letters, **1**, 84–91 (2007).
DOI: 10.3144/expresspolymlett.2007.15

[2] Felhős D., Xu D., Schlarb A. K., Váradi K., Goda T.: Viscoelastic characterization of an EPDM rubber and finite element simulation of its dry rolling friction. Express Polymer Letters, **2**, 157–164 (2008).
DOI: 10.3144/expresspolymlett.2008.21

[3] Kechek'yan A. S., Adrinova G. P., Kargin V. A.: Periodic oscillation during stretching of polyethyleneterephthalate. Polymer Science U.S.S.R., **12**, 2743–2757 (1970).

[4] Karger-Kocsis J., Benevolenski O. I., Moskala E. J.: Toward understanding the stress oscillation phenomenon in polymers due to tensile impact loading. Journal of Materials Science, **36**, 3365–3371 (2001).
DOI: 10.1023/A:1017935323058

[5] Karger-Kocsis J.: Fracture and fatigue behavior of amorphous (co)polyesters as a function of molecular and network variables. in 'Handbook of thermoplastic polyesters' (ed.: Fakirov S.) Vol1, Wiley-VHC, Weinheim, 734–756 (2002).
DOI: 10.1002/3527601961.ch16a

[6] Barenblatt G. I.: Self-oscillating neck propagation in polymers. Bulletin of the Russian Academy of Sciences: Mechanics of Solids, **5**, 110–118 (1970).

[7] Adrinova G. P., Kechekyan A. S., Kargin V. A.: Self-oscillation mechanism of necking on extension of polymers. Journal of Polymer Science, Part A-2: Polymer Physics, **9**, 1919–1933 (1971).
DOI: 10.1002/pol.1971.160091101

[8] Roseen R.: Temperature effect at self-oscillating necking during extension of polyethylene terephthalate (PETP). Journal of Materials Science, **9**, 929–933 (1974).
DOI: 10.1007/BF00570385

[9] Toda A.: Oscillation and instability of neck propagation in poly(ethylene terephthalate) films. Polymer, **34**, 2306–2314 (1993).
DOI: 10.1016/0032-3861(93)90813-P

[10] Toda A.: Oscillatory neck propagation in polymerfilms. 2. Polymer, **35**, 3638–3642 (1994).
DOI: 10.1016/0032-3861(94)90540-1

[11] Pakula T., Fischer E. W.: Instabilities of the deformation process during cold drawing of poly(ethylene terephthalate) and other polymers. Journal of Polymer Science: Polymer Physics Edition, **19**, 1705–1726 (1981).
DOI: 10.1002/pol.1981.180191104

[12] Godovsky Y. K.: Thermodynamic behavior of solid polymer in plastic deformation and cold drawing. in 'Thermophysical properties of polymers' (ed.: Godovsky Y. K.) Springer-Verlag, Berlin, 221–229 (1992).

[13] Karger-Kocsis J., Shang P. P.: A modulated DSC study on the stress oscillation phenomenon in a syndiotactic polypropylene. Journal of Thermal Analysis and Calorimetry, **69**, 499–507 (2002).
DOI: 10.1023/A:1019903605228

[14] Gutierrez M. C. G., Karger-Kocsis J., Riekel C.: Stress oscillation-induced modulated phase transformation and yielding in syndiotactic polypropylene. Chemical Physics Letters, **398**, 6–10 (2004).
DOI: 10.1016/j.cplett.2004.09.023

[15] Ebener H., Pleuger B., Petermann J.: Stress and strain oscillations in syndiotactic polypropylene and in poly(ethyleneterephthalate). Journal of Applied Polymer Science, **71**, 813–817 (1999).
DOI: 10.1002/(SICI)1097-4628(19990131)71:5<813::AID-APP15>3.0.CO;2-P

[16] Ronkay F., Czigány T.: Cavity formation and stress-oscillation during the tensile test of injection molded specimens made of PET. Polymer Bulletin, **57**, 989–998 (2006).
DOI: 10.1007/s00289-006-0670-8

[17] Vas L. M., Császi F.: Use of composite-bundle theory to predict tensile properties of yarns. Journal of the Textile Institute, **84**, 448–463 (1993).
DOI: 10.1080/00405009308658977

[18] Vas L. M., Rácz Zs.: Modeling and testing the fracture process of impregnated carbon fiber roving specimens during bending part I. Fiber bundle model. Journal of Composite Materials, **38**, 1757–1785 (2004).
DOI: 10.1177/0021998304044767

[19] Aklonis J. J., MacKnight W. J., Shen M.: Introduction to polymer viscoelasticity. Wiley-Interscience, New York (1972).

Fluorination of poly(dimethylsiloxane) surfaces by low pressure CF₄ plasma – physicochemical and antifouling properties

A. L. Cordeiro¹*, M. Nitschke¹, A. Janke¹, R. Helbig¹, F. D'Souza², G. T. Donnelly²,
P. R. Willemsen², C. Werner¹

¹Leibniz Institute of Polymer Research Dresden, Max Bergmann Center of Biomaterials Dresden; Hohe Str. 6; Dresden, Germany
²TNO Science and Industry, Bevesierweg MML (Harssens), Den Helder, The Netherlands

Abstract. Fluorinated surface groups were introduced into poly(dimethylsiloxane) (PDMS) coatings by plasma treatment using a low pressure radio frequency discharge operated with tetrafluoromethane. Substrates were placed in a remote position downstream the discharge. Discharge power and treatment time were tuned to alter the chemical composition of the plasma treated PDMS surface. The physicochemical properties and stability of the fluorine containing PDMS were characterized by X-ray photoelectron spectroscopy (XPS), atomic force microscopy (AFM) and contact angle measurements. Smooth PDMS coatings with a fluorine content up to 47% were attainable. The CF₄ plasma treatment generated a harder, non-brittle layer at the top-most surface of the PDMS. No changes of surface morphology were observed upon one week incubation in aqueous media. Surprisingly, the PDMS surface was more hydrophilic after the introduction of fluorine. This may be explained by an increased exposure of oxygen containing moieties towards the surface upon re-orientation of fluorinated groups towards the bulk, and/or be a consequence of oxidation effects associated with the plasma treatment. Experiments with strains of marine bacteria with different surface energies, *Cobetia marina* and *Marinobacter hydrocarbonoclasticus*, showed a significant decrease of bacteria attachment upon fluorination of the PDMS surface. Altogether, the CF₄ plasma treatments successfully introduced fluorinated groups into the PDMS, being a robust and versatile surface modification technology that may find application where a minimization of bacterial adhesion is required.

Keywords: coatings, plasma treatment, poly(dimethylsiloxane), fluorination, marine bacteria

1. Introduction

Low pressure plasma based processes are a versatile tool for surface modification of polymers. Depending on the plasma parameters, plasma etching or material deposition can predominate [1]. In the intermediate case, a surface layer with a thickness of few tens of nanometers is modified [2]. This type of plasma treatment is relevant for a wide variety of applications. With a simple one-step procedure the surface properties of the polymer can be changed significantly while the bulk properties remain unchanged. On the other hand, there are well-known drawbacks of this technique, as the heterogeneity of the obtained surface chemistry [3] and the lack of longterm stability (hydrophobic recovery) [4]. However, low pressure plasma treatment of polymers is an attractive approach, at least from a technological point of view, and many strategies were proposed to avoid or minimize the unfavourable mentioned side-effects. These

---

include the covalent grafting of appropriate molecules onto plasma activated surfaces or the durable adsorption of polyelectrolytes on charged surfaces (as obtained for example after ammonia plasma treatment) [5]. In addition to modification of surface chemical composition, plasma techniques have also been used to modify the surface morphology (roughening) of polymeric surfaces aiming for example at changes in wetting behaviour [6–8].

Poly(dimethylsiloxane) (PDMS) is a commercially available type of silicone rubber widely used in the fabrication of medical [9] and microfluidic devices [10], and as foul-release coating to control marine biofouling [11, 12]. Foul-release coatings are currently a successful non-toxic, environmentally friendly alternative to classical biocide-containing coatings [12]. Commercially available foul-release coatings are based on silicone elastomers since these possess a combination of properties that minimize the chemical and mechanical locking of the fouling species [13].

In this paper we report on the fluorination of PDMS (Sylgard 184) by application of tetrafluoromethane (CF₄) plasma to combine the bulk elasticity of PDMS with a desirable surface chemistry, without introducing changes in surface roughness. Towards this goal, a customized low pressure plasma set-up with a sample position far away from the excitation volume of the discharge was used to fabricate surfaces with a particularly high fluorine content consisting mainly of CF_2 and CF_3 moieties. This approach based on remote plasma configuration ensures an especially smooth but efficient treatment. The properties and stability of the fluorine containing PDMS were characterized in detail concerning chemical composition by X-ray photoelectron spectroscopy (XPS), morphology and elasticity by atomic force microscopy (AFM) and wetting by contact angle measurements. The antifouling potentialities of the CF₄ plasma treated PDMS towards microbes were evaluated by testing the attachment and adhesion strength of two species of bacteria (*Marinobacter hydrocarbonoclasticus* and *Cobetia marina*). These bacteria form biofilms that coat surfaces when in contact with sea water – either when surfaces are immersed in the sea (e.g. ship hulls) or are exposed to sea water (as in cooling systems) [14].

2. Experimental

2.1. Materials

The silicone elastomer Sylgard 184 and the Primer 1200 OS were purchased from Dow Corning (Germany). Tetrafluoromethane (99.99%) was obtained from Messer Griesheim (Germany). For stability tests and surface characterization experiments an artificial sea water (ASW*) solution was prepared using the five main components of natural sea water as described in ASTM D 1141–98 (24.53 g/l NaCl; 5.20 g/l $MgCl_2$; 4.09 g/l Na_2SO_4; 0.695 g/l KCl; 1.16 g/l $CaCl_2$) [15]. The ASW* solution was prepared using high purity salts and autoclaved before use. For the assays with marine bacteria, SSP growth medium (containing sea salt and peptone) was purchased from Sigma Aldrich (Germany), and natural sea water (SW) was collected in Den Helder, The Netherlands.

2.2. Sample preparation

Poly(dimethylsiloxane) (PDMS) coatings were prepared on inorganic carriers of variable dimensions for further modification by low pressure CF₄ plasma treatment. The PDMS coatings were fabricated using the two-part elastomer Sylgard 184. The elastomer was prepared using a ratio base to curing agent 10:1 (weight), following the suggestion of the manufacturer. The base and curing agent were mixed using a homogeneizer (Kontes; USA) for 3 min and then degassed under vacuum until all air bubbles were removed (ca. 30 min). The polymer was then deposited onto either silicon wafers of different sizes for physicochemical analysis, or onto standard microscope glass slides (26×76 mm²) for biological testing.

Silicon wafers were coated by pouring defined amounts of pre-polymer (depending on the wafer dimensions) onto the cleaned surface. The pre-polymer was air-spread for complete, homogeneous coverage of the surface. The coatings were cured at 65°C for 5 h 45 min.

For preparation of PDMS coatings onto standard microscopy slides used to test bacteria biofilm formation and release, an *in-house* film preparation system was developed (Figure 1). This consists of a metallic base onto which the glass slides were

Figure 1. *In-house* developed setup for preparation of homogeneous PDMS coatings with defined thickness onto standard microscope slides

assembled using an adhesive foil. Since the bacterial adhesion strength tests implied exposing the coatings to high shear, there was a need to improve adhesion between PDMS and glass to avoid failure during testing. This was achieved by applying a thin layer of the adhesion promoter Primer 1200 OS onto the clean glass surface. After assembly of the cleaned slides into the film preparation system, a thin layer of the adhesion promoter was applied onto the glass surface by using a fiber-free tissue (following the instructions of the provider). After 30 min, Sylgard 184 was poured onto the immobilized microscope slides and spread until homogeneous coverage of the surface. PDMS coatings with desired, well-defined thickness were then obtained using the film applicator. The metallic base containing the immobilized samples was incubated at 65°C for 45 min, after which the samples were removed from the metallic holder and further cured at 65°C for 5 h.

2.3. MicroGlider®

The topography and thickness of the PDMS coatings prepared onto standard microscope slides was examined using a MicroGlider (Fries Research & Technology GmbH, Germany). The MicroGlider operates on the principle of chromatic aberration. It functions as an optical profilometer (2D) and as an imaging measuring instrument (3D) by means of a scanning process. The MicroGlider was applied for the evaluation of surface morphology and thickness of the PDMS coatings because of its large-scale vertical resolution (from 10 nm to 300 μm), and the possibility to investigate large sample areas (up to 100×100 mm^2). The lateral resolution is, however, determined by the spot size of the reflected light on the sample and is about 1–2 μm.

2.4. Plasma treatment

The low pressure plasma set-up is shown schematically in Figure 2. The vacuum system consists of a quartz tube with an inner diameter of 20 mm and a length of 300 mm on top of a cylindrical part with an inner diameter of 200 mm and a length of 800 mm connected to a rotary vane pump. Tetrafluoromethane (CF_4) is introduced into the chamber by a gas flow control system. Pressure is measured by a capacitive vacuum gauge. The control unit is connected to a butterfly valve between the pump and the chamber and allows to set a particular pressure for a given gas flow. For plasma generation electrodes are attached to the outer surface of the quartz tube. The electrodes are connected to a 13.56 MHz radio frequency (RF) generator (Hüttinger PFG300RF) via an automatic matching network. This leads to a discharge operated in the small diameter tube. The distance between the discharge and the electrically grounded sample holder in the bottom part of the chamber was set to 60 cm.
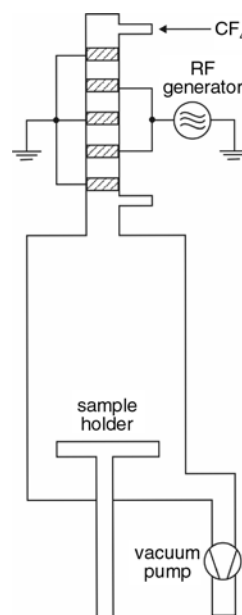

Figure 2. Low pressure plasma set-up

For the investigations of this work the set-up was operated with a CF_4 flow of 42 standard cm^3/min and a pressure of $7 \cdot 10^{-2}$ mbar. Distinct parameter sets regarding the effective RF power and the treatment time were applied.

2.5. X-ray photoelectron spectroscopy

XPS was carried out using an Amicus spectrometer (Kratos Analytical, UK) equipped with a non-monochromatic Mg K_α X-ray source operated at 240 W and 8 kV. The kinetic energy of the photoelectrons was determined using an analyzer with a pass energy of 75 eV. The take-off angle between the sample surfaces's normal and the electron optical axis of the spectrometer was 0°. In this case, the information depth is about 8 nm. Spectra were referenced to the 1s peak of aliphatic carbon at 285 eV. A satellite subtraction procedure was applied. Quantitative elemental compositions were determined from peak areas using experimentally determined sensitivity factors and the spectrometer transmission function. High-resolution spectra were deconvoluted by means of CasaXPS (Casa Software Ltd., UK).

2.6. Atomic force microscopy

Morphological features of the PDMS surface before and after CF_4 plasma treatment were characterized by atomic force microscopy (AFM) in tapping mode (Nanoscope IIIa Dimension 3100, Veeco, USA) using silicon cantilevers (Budget Sensors, Bulgaria) with a tip radius lower than 10 nm and a resonance frequency of about 75 kHz. To investigate the possible effect of aqueous media on the morphology of the plasma treated surfaces, these were imaged in deionized water (DIW) and artificial sea water (ASW*) in contact mode using Pointprobe silicon-SPM-sensors (Nanosensors, Germany) with a spring constant of about 0.2 N/m and tip radius lower than 10 nm.

The root-mean-square-roughness (RMS) and the average roughness (Sa) of 10×10 μm^2 scanned areas were calculated using the NanoScope software V530v3sr3.

Scratches on the PDMS surface were produced before imaging either upon tip engagement or application of high forces, depending on the surface mechanical properties. Nanoindentation measurements with five different loads (195, 391, 586, 782,

977 nN) were carried out to estimate both thickness and hardness of the top-most layer generated by the plasma treatment.

2.7. Contact angle measurements

Advancing and receding water contact angle measurements were carried out using a DataPhysics OCA 20 apparatus (DataPhysics, Germany) using the sessile drop method. The results presented are the average of measurements carried out onto 3 replicates. 3 to 5 individual water droplets were measured onto each replicate.

Static contact angle measurements using the captive bubble technique were carried out by attaching sessile air bubbles to the coating surface immersed in ASW* using a microsyringe. The water contact angle was obtained by averaging at least five different measurements done at different locations on each replicate and subtracted to 180°. A minimum of 3 replicates per chemistry were analyzed. The samples were conditioned in ASW* for three hours prior to measurement.

2.8. Biological tests with marine bacteria

The potential of the CF_4 plasma treated PDMS surfaces for inhibition of initial cell attachment and decrease of cell adhesion strength was investigated using biofilms of single marine bacterial species, *Cobetia marina* (collection code DSMZ 4741) and *Marinobacter hydrocarbonoclasticus* (DSMZ 8798). The bacterial strains were kept on sea salt peptone agar at 28°C and stored in the dark. Suspension cultures were prepared from the agar stocks. Briefly, untreated and plasma treated PDMS coated microscope slides were immersed in recirculating sterile (UV treated) deionized water for 7 days and then pre-conditioned in sterile artificial seawater (ASW) for 1 h prior to bacterial assay. Conditioned slides (in replicate) were immersed in 8 ml bacterial suspensions of 0.2 optical density (at 595 nm) in polystyrene quadriPERM plates (Greiner Bio-one Ltd). The plates were incubated at 28°C on a rotary shaker (150 rpm). After 1 h incubation, the slides were gently dipped in sterile seawater (SW) to remove suspended cells. The slides were transferred back into quadriPERM plates containing 8 ml of sterile SW with added growth medium and incubated again for 4 h at 28°C under gentle shaking (150 rpm). At the end of incubation

the slides were again gently rinsed, then placed into slide holders and partially air-dried. The attached biomass was quantified by staining the attached cells with 1.5 µM of the fluorochrome SYTO13 (Invitrogen) and measuring absorption with a Tecan plate reader (GENios, Magellan software) [16].

The adhesion strength of adhered bacteria was quantified using a rotating drum test that was originally designed for the determination of antifouling performance of marine antifouling coatings as described in ASTM D 4939 [17]. After the growth step, replicate slides were mounted on the surface of a custom-made high-speed rotating drum [18]. The drum was then rotated with the surface speed of ~340 m/min for 10 min in SW. This rotational speed of the drum exposes the bacteria to shear stress (turbulent flow), removing bacteria cells from the surfaces. The remaining bacteria were quantified using the stain SYTO13 as described above. The results were expressed as the percentage of bacteria removed or detached by shear stress [(RFU of attached bacteria before release – RFU of bacteria remaining after release)/RFU of attached bacteria before release ×100]. Confidence limits of 95% were calculated.

3. Results and discussion

3.1. Coating preparation

PDMS coatings were prepared on inorganic carriers of variable dimensions for further surface modification by low pressure CF_4 plasma treatment. The PDMS coatings to be used for biological testing were prepared onto standard microscopy slides using an *in-house* developed film preparation setup, which allowed the control of the coating thickness. It has been demonstrated that the coating thickness influences the adhesion strength of fouling organisms [19, 20]. Therefore, the homogeneity and thickness of the PDMS coatings to be tested with organisms were evaluated by optical analysis using the MicroGlider®. The surface of the PDMS coating was very smooth and topographically homogeneous (Figure 3a). The thickness of the coating was determined to be ca. 150 µm (Figure 3b).

3.2. Chemical composition and stability

X-ray photoelectron spectroscopy (XPS) was used to investigate the surface chemistry upon plasma treatment. Table 1 summarizes the atomic composition of untreated and plasma-treated PDMS sur-
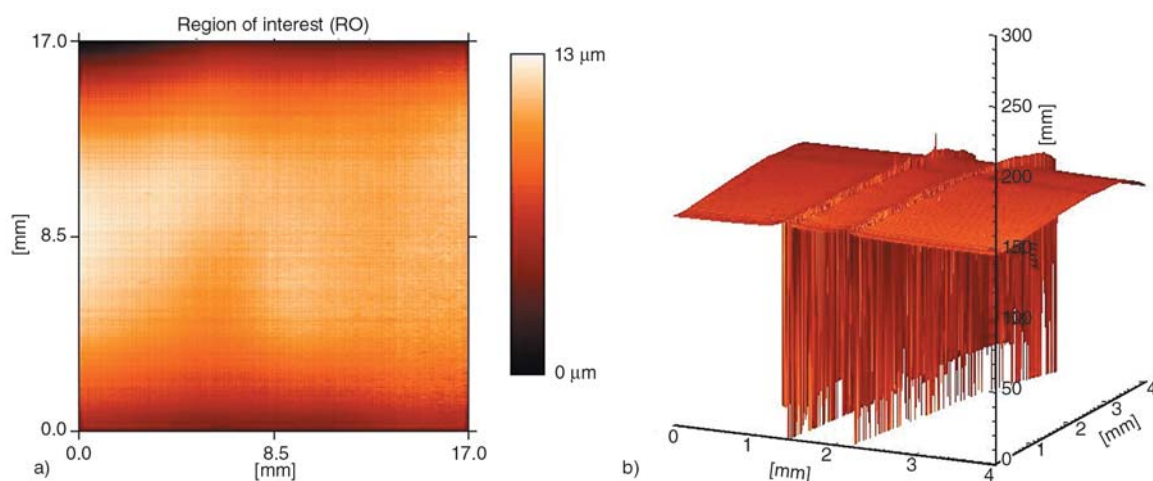

Figure 3. Representative MicroGlider® images of the PDMS coating. a – 2D image of a 17×17 mm² area and b – 3D image of a scratched coating at the edge of the slide (area scanned = 4×4 mm², estimated thickness = 150 µm)

Table 1. XPS data (composition in atomic %) of plasma fluorinated PDMS

Plasma treatment	Composition (atomic %)			
	C 1s	O 1s	Si 2p	F 1s
Untreated[a]	50.0	25.0	25.0	0.0
100 W; 300 s[b]	34.1	12.1	6.5	47.3
50 W; 200 s[b]	35.3	17.9	7.7	39.1
50 W; 100 s[b]	36.5	18.7	9.6	35.2

[a]Theoretical composition.

[b]Data correspond to average of 5-6 samples treated in 2 different batches.

faces for different treatment conditions. The fluorine content increased with power and treatment time up to 47%. For comparison, poly(tetrafluoroethylene) (PTFE), the most common fully fluorinated polymer, has a fluorine content of 66.6%.

To further characterize the chemical structure of the plasma treated PDMS surfaces, high resolution C1s spectra were recorded. It was assumed, that the spectra consist of five components corresponding to aliphatic carbon (285.0 eV), $-\underline{C}-CF-$ (287.6 eV), $-\underline{C}F-$ (290.4 eV), $-\underline{C}F_2-$ (292.0 eV) and $-\underline{C}F_3$ (294.0 eV) [21]. To evaluate the C1s spectra of the fluorinated PDMS surfaces obtained under different plasma treatment parameters, a peak deconvolution procedure was applied. Five component peaks with a given shape (Gaussian-Lorentzian ratio 50:50) were set to the energy values mentioned above. The fit procedure was allowed to vary the component energies except 285 eV within a range of ±0.5 eV, the component intensities and a common value for the full width at half maximum. Deconvoluted C1s spectra of fluorinated PDMS prepared using different plasma treatment conditions are presented in Figure 4. The assumptions of the peak deconvolution model were adequate to describe the shape of the C1s spectra, agreeing with

other studies where complex fluorinated polymer systems, as obtained by plasma-based techniques, were investigated [22–24]. All deconvoluted spectra show the full range of differently fluorinated carbon species suggesting a significantly branched and/or cross-linked structure. For the investigated parameter range the relative amount of highly fluorinated species increases continuously with increasing power and treatment time ($[\underline{C}F_3]$:$[C_xH_y]$ increased from 0.13 to 0.45, and $[\underline{C}F_2]$:$[C_xH_y]$ increased from 0.62 to 1.71 (Figure 4)).

Considering potential underwater applications, and the evidence of chemical re-structuring of silicones upon contacting water [25], we have evaluated the chemical stability of the plasma treated PDMS in aqueous media. Additionally, to assess the influence of ionic strength on the chemical stability of the plasma treated samples, and envisaging the possibility to use these surfaces in marine environment, the fluorine content was determined by XPS immediately after plasma treatment, after storage in ambient conditions, after incubation in recirculating deionized water (DIW), and in artificial sea water (ASW*) for up to one month (Figure 5).

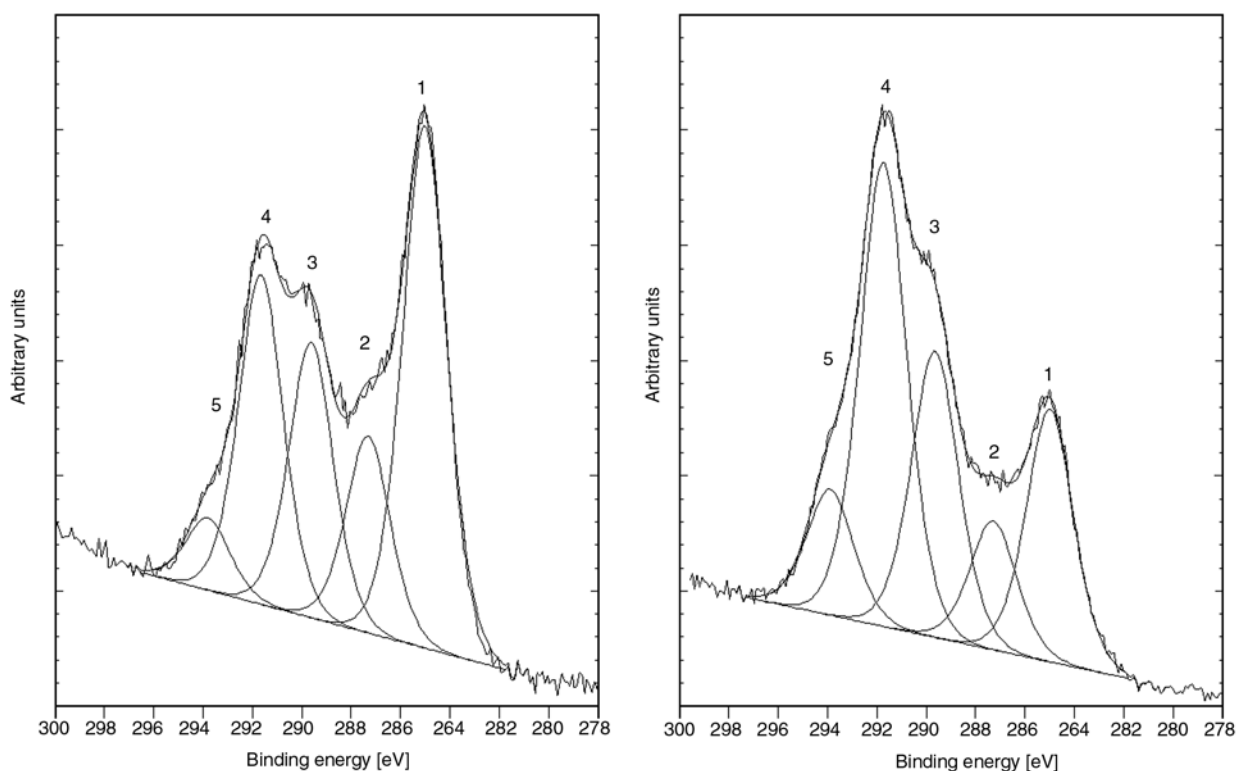The fluorine content decreased by 6% when samples were simply stored in ambient conditions for

Figure 4. Representative XPS C1s spectra of CF$_4$ plasma treated PDMS using the parameters: 50 W, 100 s (left), and 100 W, 300 s (right). Peak deconvolution (1) C$_x$H$_y$, (2) $-\underline{C}-CF-$, (3) $-\underline{C}F-$, (4) $-\underline{C}F_2-$, and (5) $-\underline{C}F_3$.
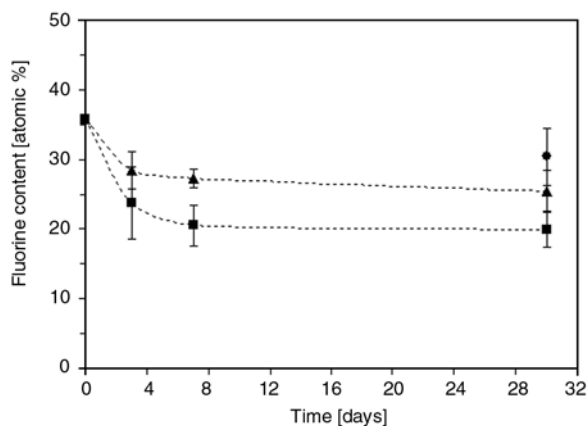
Figure 5. Fluorine content (atomic %) of CF_4 plasma treated PDMS. After plasma treatment (time = 0), after storage in ambient conditions (●), after incubation in recirculating DIW (▲), and after incubation in recirculating ASW* (■).

30 days pointing towards a re-orientation/migration of the fluorine groups away from the surface during aging. The introduction of functional groups onto the surface of silicone has been recognized to lack stability due to the reorganization of silicone elastomers over time [26, 27, 29, 31, 32]. The phenomena of hydrophobic recovery upon PDMS plasma oxidation has been extensively investigated, and explained namely by the reorientation of surface hydrophilic groups towards the bulk and/or reorientation of non-polar groups in the bulk towards the surface, by the diffusion of pre-existing low molecular weight (LMW) species through the bulk to the surface, or migration of created LMW species during treatment to the surface [26]. These same effects are believed to be responsible for the observed decrease of fluorine content on the surface plasma treated PDMS during aging.

When samples were incubated in aqueous media, the fluorine content suffered a steep initial decrease (Figure 5). The fluorine content further decreased after 1 week of incubation, but no additional significant differences could be observed after 4 weeks. This decrease can be explained by re-arrangements of fluorinated groups when the coatings are immersed in water, and by the removal of low molecular weight compounds generated by plasma treatment. The loss of fluorine was significantly higher when the surfaces were incubated in ASW* (loss of 45% of initial content) as compared with DIW (loss of 29% of initial content), revealing the

deleterious effect of the presence of salt on the stability of the plasma treated surfaces.

3.3. Morphology

The plasma treatment of polymer surfaces may greatly alter their morphology [28, 29]. For this reason, we have investigated the morphological features of the PDMS surface before and after plasma treatment by atomic force microscopy (AFM) in tapping mode. The surface of the plasma treated PDMS, even using the 'harshest' plasma treatment parameters tested (Figure 6b), was very smooth and comparable to the non-plasma treated surface (Figure 6a). Possible effects of plasma treatment time on surface morphology were investigated for different treatment times (100, 200, and 300 s). The surfaces were very smooth (RMS = 0.5–0.6 nm), no significant morphological differences between treatments could be detected (results not shown).

Additionally, as the exposure of silicones to aqueous media (sea water, phosphate buffered saline) can alter surface morphology [29, 30], the morphological features of the plasma treated PDMS when incubated in DIW and ASW* for 7 days were investigated. Typical height images of the PDMS exposed to the 'harshest' plasma conditions tested when incubated in aqueous media are presented in Figure 6c (DIW) and Figure 6d (ASW*). No morphological changes were observed upon incubation in either of the media tested.

3.4. Mechanical properties

It has been reported that the plasma treatment of PDMS, using a variety of different gases, generates a brittle silica-like layer at the PDMS surface [29, 31–35]. The formation of this hard layer can be explained by the surface oxidation and the etching effects associated with the plasma treatment, exposing some of the silica filler to the surface of the PDMS [29]. In order to investigate the extent of the impact of the CF_4 plasma treatment on the mechanical properties of the PDMS, AFM imaging was performed after indentation measurements and after surface scratching with the AFM tip under high load (Figure 7).

The results showed that the CF_4 plasma treatment resulted in the formation of a harder layer on the
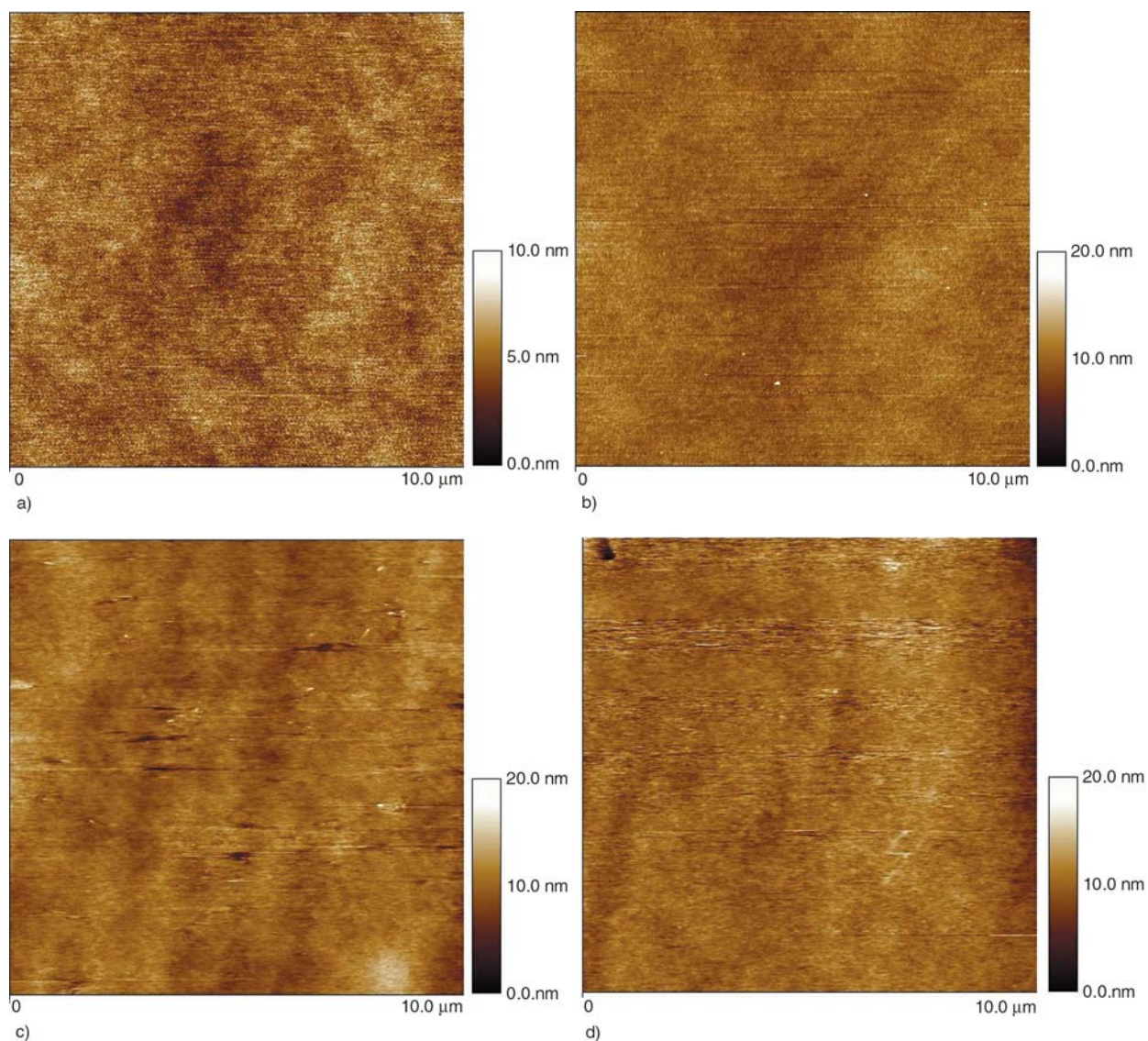
Figure 6. AFM height images of a – PDMS (RMS = 1.15 nm), and b – plasma fluorinated PDMS (plasma treatment conditions: 100 W; 300 s) after preparation (RMS = 1.34 nm); c – after 7 days incubation in recirculating DIW (RMS = 1.33 nm), and d – after 7 days incubation in recirculating ASW* (RMS = 1.58 nm). a) and b) imaging in air using tapping mode, c) imaging in DIW using contact mode, and d) imagining in ASW* using contact mode.

top-most surface of the PDMS, as higher force (>195 nN) was needed to cut through the surface, as compared with the untreated PDMS (data not shown). An apparent wrinkling of the surface was observed (Figure 7) as compared with the characteristic cracking of brittle surfaces [31–33, 35]. The top-most layer seems to elongate under stress, resulting in local thinning of the layer, being reflected on an apparent wrinkling.

The variety and extent of plasma-based surface modification effects, in particular the alteration of elastic properties of PDMS, depend on a multitude of interaction mechanisms, each of them acting on a characteristic depth scale. In low pressure plasma

reactors an effect on the scale of several tens of nanometers is most probably attributed to (vacuum) ultraviolet irradiation. As the ultraviolet irradiance of plasma sources with different process gases and different geometries can be different by orders of magnitude [36], the mechanical properties of the treated surface may vary over a certain extend. This possibly explains the difference between our experimental findings (non-brittle surface) and the observations reported in the literature (brittle surface) [31–33, 35].

The differences in mechanical properties of untreated and CF_4 plasma treated PDMS surfaces were further investigated by performing nanoin-
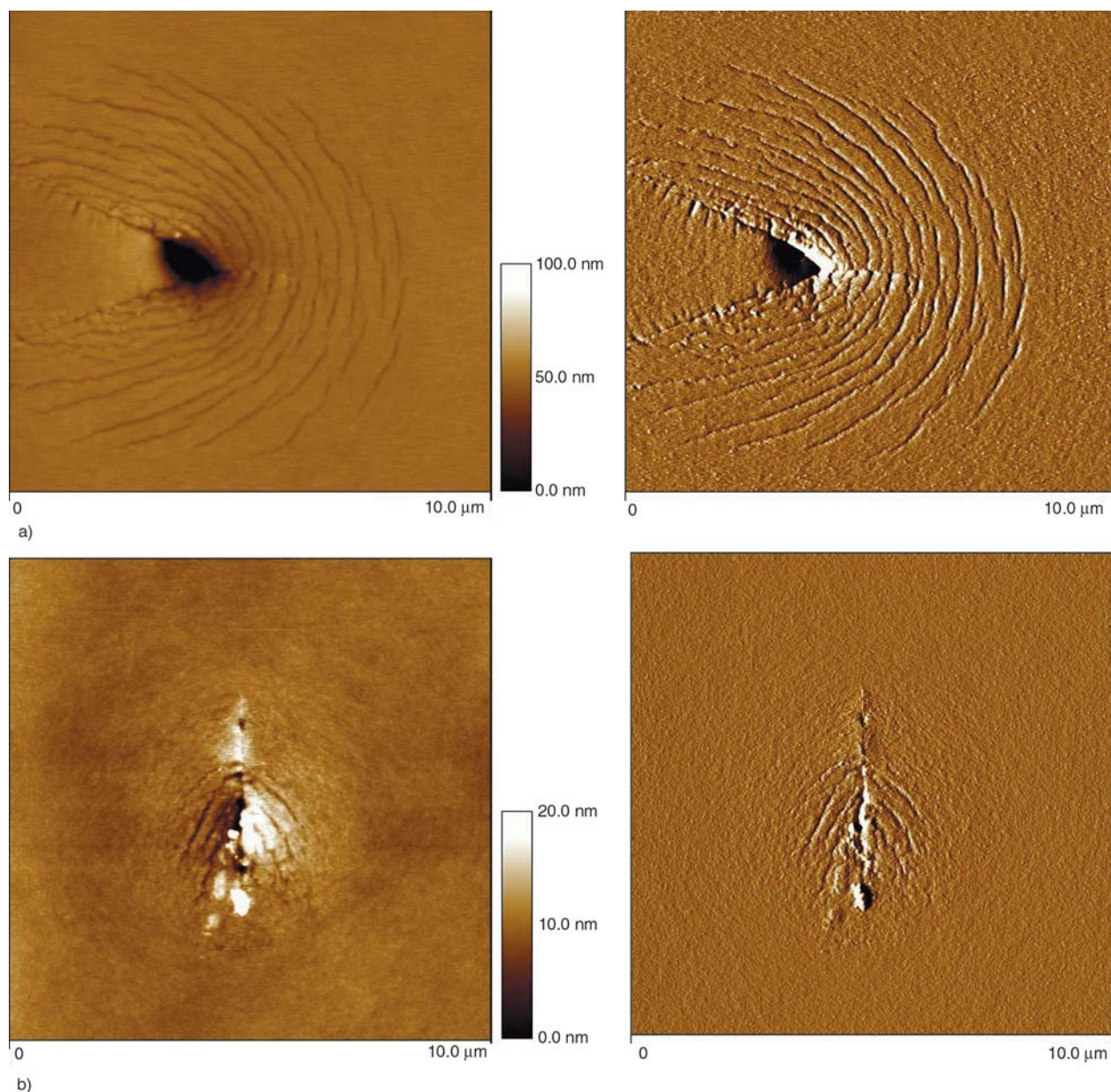
Figure 7. AFM height (left) and amplitude (right) images of plasma fluorinated PDMS (plasma conditions: 50 W; 200 s). Imaging after a – indentation measurement at high force (440 nN); and b – scratching the surface with the AFM tip using high force (440 nN). Imaging in air using tapping mode.

dentation measurements with five different loads. The analysis of the obtained curves allowed to conclude on the presence of a possible double-layer structure, estimate its thickness, and evaluate the hardness of the top-most surface of the PDMS. The force-separation curves of unmodified PDMS clearly differed from the curves obtained for plasma treated PDMS (results not shown). In the case of the plasma treated surfaces, a break in the force-separation curve was observed, indicating the presence of a double layer coating with the mechanical properties of the top-most layer differing from the underlying one. The measured thick-

ness of the top-most layer generated by the plasma treatment and selected indentation results for untreated and plasma treated samples (extracted from load-indentation curves) are presented in Table 2.

The results showed that the thickness of the top-most layer increased with increasing plasma treatment time. The mechanical properties of the top-most layer generated by plasma treatment can be compared for the different plasma conditions tested by comparing the indentation at constant low load. It was observed that when applying a load of 195 nN, the indentation of all plasma treated sam-

Table 2. Thickness of the top-most layer generated by plasma treatment and indentation at low load (195 nN), determined by analysis of AFM load-indentation curves

	Plasma treatment			
	Untreated	50 W; 100 s	50 W; 200 s	50 W; 300 s
Top-most layer thickness [nm][a]	n.a.	180–200	250–280	280–300
Indentation [nm] at load = 195 nN[b]	300 ± 11	112 ± 3	108 ± 3	111 ± 1

[a] data obtained for 2 independent samples
[b] data corresponds to the average of results extracted from 10 independent curves (± standard deviation)

ples was below 180 nm (i.e. within the thickness of the top-most layer) allowing the characterization of the top-most surface of the plasma treated PDMS. A significantly higher indentation was measured for the untreated PDMS as compared with the plasma treated PDMS, indicating that the top-most layer generated by the plasma treatment was characterized by a higher Young modulus. No significant differences could be detected between the different plasma conditions tested. This suggests that the plasma conditions tested only had a significant effect on the thickness of the generated top-most layer but not on its mechanical properties. When applying loads higher than 195 nN, the indentation was deeper than the thickness of the top-most layer, resulting in scattered indentation data due to the contribution of the bulk PDMS.

3.5. Wettability

The extent of changes in the wetting properties of the PDMS surface generated by CF_4 plasma treatment was evaluated by measuring advancing and receding water contact angles using the sessile drop technique (Table 3). Contrary to what would be expected, the CF_4 plasma treatment resulted in a more hydrophilic surface as compared with the untreated surface. This can be explained if we consider that the effect of introduction of fluorine is overcompensated by side effects associated with plasma treatment as surface oxidation. Furthermore, the fluorine groups originally at the surface will re-orient towards the bulk exposing moieties rich in oxygen to the surface, resulting in a decrease of the measured water contact angle. The contact

Table 3. Advancing and receding water contact angles measured by the sessile drop technique

Plasma treatment	Advancing water contact angle [°]	Receding water contact angle [°]
Untreated	118.7 ± 1.4	85.6 ± 2.8
100 W; 300 s	100.9 ± 1.1	43.9 ± 5.3

Table 4. Static water contact angle measured using the captive bubble technique

	Plasma treatment	
	Untreated	100 W; 300 s
Static water contact angle [°]	95.2 ± 0.9	124.7 ± 1.3

angle hysteresis increased after plasma treatment, possibly due to chemical heterogeneities [37] introduced by the plasma treatment and/or due to surface reorganization [38].

Considering the potential use of these surfaces in the marine environment, and the effect of sea water on the surface properties of silicones [39, 40], we have measured static water contact angles on untreated and plasma treated surfaces using captive air bubbles in ASW* (Table 4). The captive bubble results in ASW* were in good agreement with the data obtained using the sessile drop technique. The PDMS surface was found to be more hydrophilic after CF_4 plasma treatment.

3.6. Marine bacteria: attachment and adhesion strength

The effect of the introduction of fluorine into the PDMS surface on the inhibition of initial attachment and on the adhesion strength of the marine bacteria *Cobetia marina* and *Marinobacter hydrocarbonoclasticus* was investigated. These two species were selected as they are characterized by distinct surface energies: *Cobetia marina* is hydrophilic, and *Marinobacter hydrocarbonoclasticus* is hydrophobic [41]. The results of the assays on glass control slides, untreated PDMS coatings, and CF_4 plasma treated PDMS with a fluorine content of 47% (atomic %) are presented in Figure 8. The attachment of both *Marinobacter hydrocarbonoclasticus* and of *Cobetia marina* were dramati-
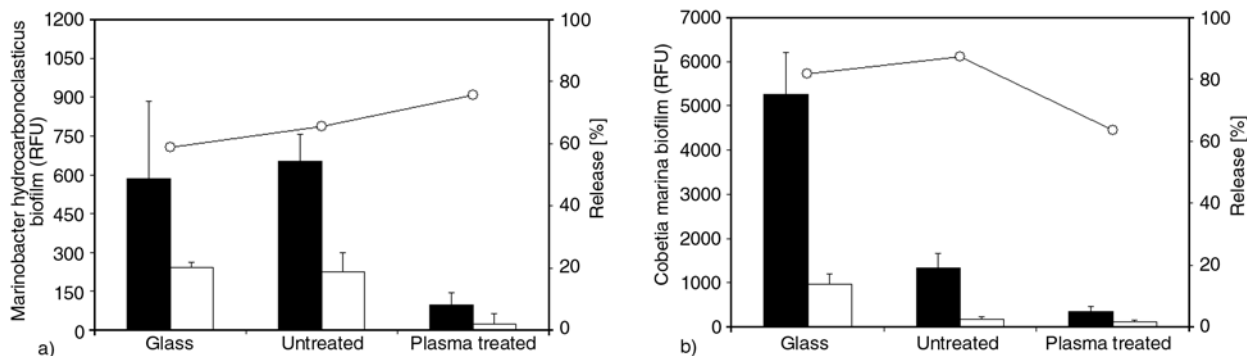
Figure 8. Marine bacterial biofilms of a – *Marinobacter hydrocarbonoclasticus* and b – *Cobetia marina* on glass, untreated PDMS, and CF_4 plasma treated PDMS. Bacterial biofilm formation (black bars) and remaining marine bacteria biofilm after rotation at 340 m/min for 10 min (white bars). The release percentages (O) represent the percentages of biofilm removal upon exposure to shear. N = 45; error bars = 2×standard error derived from arcsine-transformed data.

cally reduced when introducing fluorine into the PDMS coating. Bacterial adhesion to surfaces has been attributed to many factors, including surface chemical composition [42, 43], surface hydrophilicity [44], surface roughness [45], and surface mechanical properties [46]. As no significant differences in surface roughness were detected between untreated and plasma treated samples (Figure 6), the differences observed in bacteria attachment cannot be attributed to differences in surface morphology. The plasma treatment has altered the mechanical properties of the top-most surface of the PDMS (Table 2). A positive correlation between substrate stiffness and the initial attachment of the bacteria *Staphylococcus epidermis* has been reported [46]. However this correlation does not apply in the case of the present study as lower bacteria attachment was observed for the plasma treated (harder) surface. Recent bacteria studies using silicon oxide coatings deposited by plasma-assisted chemical vapour deposition (PACVD) methods showed that the attachment of *Pseudomonas fluorescens* decreased with increasing the surface water contact angle, the same trend being observed for *Cobetia marina* [41]. An opposite effect was observed in our experiments. Concerning the attachment of *Marinobacter hydrocarbonoclasticus*, it was observed to increase with increasing the water contact angle of the silicon oxide surfaces [41], being in good agreement with our observations. The mechanism of bacteria adhesion is very complex, depending not only on the surface physicochemical properties but also on the properties of the bacteria. Although hydrophobicity

has been generally considered to play a significant role in bacteria adhesion, our results indicate that the nature of the surface functional groups is critical in defining the interaction between substrate and bacteria. The mechanism of antimicrobial action provided by the presence of fluorinated species at the plasma treated PDMS surface is however unknown and deserves further investigations. The adhesion strength of *Marinobacter hydrocarbonoclasticus* decreased upon introduction of fluorine into the PDMS surface (% removal increases from 65 to 76%), while the adhesion strength of *Cobetia marina* increased after plasma treatment (% removal decrease from 87 to 64%). The easier detachment of hydrophobic bacteria (*Marinobacter*) from more hydrophilic surface (plasma treated) and of hydrophilic bacteria (*Cobetia*) from more hydrophobic surface (untreated) support that both the native properties of the individual strain of bacteria and the chemical composition of the surface determine bacteria adhesion strength [47].

4. Conclusions

Low pressure CF_4 plasma can be used to successfully introduce fluorinated groups into PDMS surfaces. The plasma treatment generated a smooth, non-brittle layer at the top-most surface of the PDMS, with very high fluorine content and possibly a significantly branched and/or cross-linked structure. Stability tests revealed a loss of fluorine in the plasma treated surface upon incubation in aqueous media, possibly due to the removal of low molecular weight (LMW) compounds generated by

plasma treatment, and/or to the re-orientation of the fluorine moieties away from the surface. As a consequence of oxidation effects associated with the plasma treatment, and the re-orientation of fluorinated groups, the PDMS surface was more hydrophilic after plasma treatment. The antifouling potentialities of PDMS towards two species of marine bacteria was improved after CF$_4$ plasma treatment suggesting that the approach described for the fluorination of PDMS surfaces may be applied to minimize microbial adhesion.

Acknowledgements

References

[1] Nitschke M.: Plasma modification of polymer surfaces and plasma polymerization. in 'Polymer surfaces and interfaces: Characterization, modification and applications' (ed.: Stamm M.) Springer, Berlin, 203–214 (2008).
DOI: 10.1007/978-3-540-73865-7

[2] Hollander A., Wilken R., Behnisch J.: Subsurface chemistry in the plasma treatment of polymers. Surface and Coatings Technology, **116–119**, 788–791 (1999).
DOI: 10.1016/S0257-8972(99)00297-2

[3] Meyer-Plath A. A., Schröder K., Finke B., Ohl A.: Current trends in biomaterial surface functionalization- nitrogen-containing plasma assisted processes with enhanced selectivity. Vacuum, **71**, 391–406 (2003).
DOI: 10.1016/S0042-207X(02)00766-2

[4] Rangel E. C., Gadioli G. Z., Cruz N. C.: Investigations on the stability of plasma modified silicone surfaces. Plasmas and Polymers, **9**, 35–48 (2004).
DOI: 10.1023/B:PAPO.0000039815.07810.bd

[5] Nitschke M., König U., Lappan U., Minko S., Simon F., Zschoche S., Werner C.: Low pressure plasma based approaches to fluorocarbon polymer surface modification. Journal of Applied Polymer Science, **103**, 100–109 (2007).
DOI: 10.1002/app.24717

[6] Vlachopolou M. E., Petrou P. S., Kakabakos S. E., Tserepi A., Gogolides E.: High-aspect-ratio plasma-induced nanotextured poly(dimethylsiloxane) surfaces with enhanced protein adsorption capacity. Journal of Vacuum Science and Technology B, **26**, 2543–2548 (2008).

[7] Tserepi A. D., Vlachopoulou M. E., Gogolides E.: Nanotexturing of poly(dimethylsiloxane) in plasmas for creating robust super-hydrophobic surfaces. Nanotechnology, **17**, 3977–3983 (2006).
DOI: 10.1088/0957-4484/17/15/062

[8] Minko S., Müller M., Motornov M., Nitschke M., Grundke K., Stamm M.: Two-level structured self-adaptive surfaces with reversibly tunable properties. Journal of American Chemical Society, **125**, 3896–3900 (2003).
DOI: 10.1021/ja0279693

[9] Abbasi F., Mirzadeh H., Katbab A-A.: Modification of polysiloxane polymers for biomedical applications: A review. Polymer International, **50**, 1279–1287 (2001).
DOI: 10.1002/pi.783

[10] McDonald J. C., Whitesides G. M.: Poly(dimethylsiloxane) as a material for fabricating microfluidic devices. Accounts of Chemical Research, **35**, 491–499 (2002).
DOI: 10.1021/ar010110q

[11] Anderson C., Atlar M., Callow M. E., Candries M., Milne A., Townsin R.: The development of foul-release coatings for seagoing vessels. Journal of Marine Design and Operations, **84**, 11–23 (2003).

[12] Yebra D. M., Kiil S., Dam-Johansen K.: Antifouling technology- Past, present and future steps towards efficient and environmentally friendly antifouling coatings. Progress in Organic Coatings, **50**, 75–104 (2004).
DOI: 10.1016/j.porgcoat.2003.06.001

[13] Brady Jr. R. F.: Properties which influence marine fouling resistance in polymers containing silicon and fluorine. Progress in Organic Coatings, **35**, 31–35 (1999).
DOI: 10.1016/S0300-9440(99)00005-3

[14] Cooksey K. E., Wigglesworth-Cooksey B.: Adhesion of bacteria and diatoms to surfaces in the sea: A review. Aquatic Microbial Ecology, **9**, 87–96 (1995).

[15] ASTM D 1141: Standard practice for the preparation of substitute ocean water 1998 (2003).

[16] Bers A. V., D'Souza F., Klijnstra J. W., Willemsen P. R., Wahl M.: Chemical defence in mussels: Antifouling effect of crude extracts of the periostracum of the blue mussel Mytilus edulis. Biofouling, **22**, 251–259 (2006).
DOI: 10.1080/08927010600901112

[17] ASTM D 4939: Standard test method for subjecting marine antifouling coating to biofouling and fluid shear forces in natural seawater 1989 (2003).

[18] D'Souza F., Bruin A., Biersteker R., Donnelly G. T., Klijnstra J. W., Rentrop C. H. A., Willemsen P. R.: Bacterial assay for rapid assessment of antifouling properties of coatings and materials. in preparation (2009).

[19] Kim J., Chisholm B. J., Bahr J.: Adhesion study of silicone coatings: The interaction of thickness, modulus and shear rate on adhesion force. Biofouling, **23**, 113–120 (2007).
DOI: 10.1080/08927010701189708

[20] Chaudhury M. K., Finlay J. A., Chung J. Y., Callow M. E., Callow J. A.: The inluence of elastic modulus and thickness on the release of the soft-fouling green alga *Ulva linza* (syn. *Enteromorpha linza*) from poly(dimethylsiloxane) (PDMS) model networks. Biofouling, **21**, 41–48 (2005).
DOI: 10.1080/08927010500044377

[21] Beamson G., Briggs D.: High resolution XPS of organic polymers, The Sienta ESCA 300 Database. Wiley and Sons, Chichester (1992).

[22] Béche B., Papet P., Debarnot D., Gaviot E., Zyss J., Poncin-Epaillard F.: Fluorine plasma treatment on SU-8 polymer for integrated optics. Optics Communications, **246**, 25–28 (2005).
DOI: 10.1016/j.optcom.2004.10.081

[23] Sawada Y., Kogoma M.: Plasma-polymerized tetrafluoroethylene coatings on silica particles by atmospheric-pressure glow discharge. Powder Technology, **90**, 245–250 (1997).
DOI: 10.1016/S0032-5910(96)03223-8

[24] Martin I. T., Dressen B., Boggs M., Liu Y., Henry C. S., Fisher E. R.: Plasma modification of PDMS microfluidic devices for control of electroosmotic flow. Plasma Processes and Polymers, **4**, 414–424 (2007).
DOI: 10.1002/ppap.200600197

[25] Chen C., Wang J., Chen Z.: Surface restructuring behaviour of various types of poly(dimethylsiloxane) in water detected by SFG. Langmuir, **20**, 10186–10193 (2004).
DOI: 10.1021/la049327u

[26] Kim J., Chaudhury M. K., Owen M. J., Orbeck T.: The mechanisms of hydrophobic recovery of polydimethylsiloxane elastomers exposed to partial electrical discharges. Journal of Colloid and Interface Science, **244**, 200–207 (2001).
DOI: 10.1006/jcis.2001.7909

[27] Murakami T., Kuroda S-I., Osawa Z.: Dynamics of polymeric solid surfaces treated with oxygen plasma: Effect of aging media after plasma treatment. Journal of Colloid and Interface Science, **202**, 37–44 (1998).
DOI: 10.1006/jcis.1997.5386

[28] Coen M. C., Dietler G., Groening P., Kasas S.: AFM measurements of the topography and the roughness of ECR plasma treated polypropylene. Applied Surface Science, **103**, 27–34 (1996).
DOI: 10.1016/0169-4332(96)00461-8

[29] Williams R. L., Wilson D. J., Rhodes N. P.: Stability of plasma-treated silicone rubber and its influence on the interfacial aspects of blood compatibility. Biomaterials, **25**, 4659–4673 (2004).
DOI: 10.1016/j.biomaterials.2003.12.010

[30] Arce F. T., Avci R., Beech I. B., Cooksey K. E., Wigglesworth-Cooksey B.: Modification of surface properties of a poly(dimethylsiloxane)-based elastomer, RTV11, upon exposure to seawater. Langmuir, **22**, 7217–7225 (2006).
DOI: 10.1021/la060809a

[31] Fritz J. L., Owen M. J.: Hydrophobic recovery of plasma-treated polydimethylsiloxane. Journal of Adhesion, **54**, 33–45 (1995).

[32] Everaert E. P., van der Mei H. V., de Vries J., Busscher H. J.: Hydrophobic recovery of repeatedly plasma-treated silicone rubber. Part 1. Storage in air. Journal Adhesion Science Technology, **9**, 1263–1278 (1995).
DOI: 10.1163/156856195X01030

[33] Owen M. J., Smith P. J.: Plasma treatment of polydimethylsiloxane. Journal of Adhesion Science and Technology, **8**, 1063–1075 (1994).
DOI: 10.1163/156856194X00942

[34] Hillborg H., Ankner J. F., Gedde U. W., Smith G. D., Yasuda H. K., Wikström K.: Crosslinked polydimethylsiloxane exposed to oxygen plasma studied by neutron reflectometry and other surface specific techniques. Polymer, **41**, 6851–6863 (2000).
DOI: 10.1016/S0032-3861(00)00039-2

[35] Cordeiro A. L., Zschoche S., Janke A., Nitschke M., Werner C.: Functionalization of poly(dimethysiloxane) surfaces with maleic anhydride copolymer films. Langmuir, in press (2009).
DOI: 10.1021/la803054s

[36] Holländer A., Klemberc-Sapieha J. E., Werthelmer M. R.: Vacuum-ultraviolet induced oxidation of the polymers polyethylene and polypropylene. Journal of Polymer Science Part A: Polymer Chemistry, **33**, 2013–2025 (1995).
DOI: 10.1002/pola.1995.080331208

[37] Li D., Neumann A. W.: Surface heterogeneity and contact angle hysteresis. Colloid and Polymer Science, **270**, 498–504 (1992).
DOI: 10.1007/BF00665995

[38] Yasuda H., Sharma A. K., Yasuda T.: Effect of orientation and mobility of polymer molecules at surfaces on contact angle and its hysteresis. Journal of Polymer Science: Polymer Physics Edition, **19**, 1285–1291 (1981).
DOI: 10.1002/pol.1981.180190901

[39] Estarlich F. F., Lewey S. A., Nevell T. G., Thorpe A. A., Tsibouklis J., Upton A. C.: The surface properties of some silicone and fluorosilicone coating materials immersed in sea water. Biofouling, **16**, 2–4 (2000).

[40] Nevell T. G., Edwards D. P., Davis A. J., Pullin R. A.: The surface properties of silicone elastomers exposed to seawater. Biofouling, **10**, 199–212 (1996).

[41] Akesso L., Pettitt M. E., Callow J. A., Callow M. E., Stallard J., Teer D., Liu C., Wang S., Zhao Q., D'Souza F., Willemsen P. R., Donnelly G. T., Donik C., Kocijan A., Jenko M., Jones L. A., Guinaldo P. C.: The potential of nanostructured silicon oxide type coatings deposited by PACVD for control of aquatic biofouling. Biofouling, **25**, 55–67 (2009).
DOI: 10.1080/08927010802444275

[42] Tang H., Cao T., Wang A., Liang X., Salley S. O., McAllister II J. P.: Effect of surface modification of siliconeon *Staphylococcus epidermis* adhesion and colonization. Journal Biomedical Materials Research Part A, **80**, 885–894 (2007).
DOI: 10.1002/jbm.a.30952

[43] Cao T., Tang H., Liang X., Wang A., Auner G. W., Salley S. O., Ng K. Y. S.: Nanoscale investigation on adhesion of *E. Coli* to surface modified silicone using atomic force microscopy. Biotechnology and Bioengineering, **94**, 167–176 (2006).
DOI: 10.1002/bit.20841

[44] Dexter S. C., Sullivan Jr. J. D., Williams III J., Watson S. W.: Influence of substrate wettability on the attachment of marine bacteria to various surfaces. Applied Microbiology, **30**, 298–308 (1975).

[45] Taylor R. L., Verran J., Less G. C., Ward A. J. P.: The influence of substratum topography on bacterial adhesion to polymethyl methacrylate. Journal of Materials Science: Materials in Medicine, **9**, 17–22 (1998).

[46] Lichter J. A., Thompson M. T., Delgadilho M., Nishikawa T., Rubner M. F., van Vliet K. J.: Substrata mechanical stiffness can regulate adhesion of viable bacteria. Biomacromolecules, **9**, 1571–1578 (2008).
DOI: 10.1021/bm701430y

[47] Liu Y., Zhao Q.: Influence of surface energy on modified surfaces on bacterial adhesion. Biophysical Chemistry, **117**, 39–45 (2005).
DOI: 10.1016/j.bpc.2005.04.015

Theoretical and experimental study of foaming process with chain extended recycled PET

I. Coccorullo, L. Di Maio, S. Montesano, L. Incarnato*

Department of Chemical and Food Engineering, University of Salerno, via Ponte don Melillo,
I-84084 Fisciano (Salerno), Italy

Abstract. The theoretical and experimental study of a thermoplastic polymer foaming process is presented. Industrial scraps of PET were used for the production of foamed sheets. The process was performed by making use of a chemical blowing agent (CBA) in the extrusion process. Due to the low intrinsic viscosity of the recycled PET, a chain extender was also used in order to increase the molecular weight of the polymer matrix. Pyromellitic dianhydride (PMDA) and Hydrocerol CT 534 were chosen as chain extender and CBA, respectively. The reactive extrusion and foaming were performed in a two step process.
Rheological characterization was carried out on PET samples previously treated with PMDA, as well as the morphological study was performed to define the cellular structure of the foams produced. Moreover, in order to predict the morphology of the foam, a non isothermal model was developed by taking into account both mass transfer phenomenon and viscous forces effect. Model results were compared with experimental data obtained analyzing the foamed samples. The model was validated in relation to working conditions, chemical blowing agent percentage and initial rheological properties of recycled polymer. A pretty good agreement between experimental and calculated data was achieved.

Keywords: *processing technologies, modeling and simulations, recycling, industrial applications*

1. Introduction

Since their origin in the 1930s, cellular plastics or polymeric foams have received wide success in industrial and consumer applications due to the low material costs, high strength-to-weight ratios, wide range of properties, and ease of processing. Moreover, these materials are particularly attractive since they can be produced with average cell sizes ranging from few microns to hundreds of microns. For any given polymer, the use of different blowing agents and process conditions can yield 'new materials' with different densities, structures, and properties.

Foaming consists of generating tiny gas bubbles in the polymer melt phase in order to produce lightweight materials without sacrificing mechanical and physical properties of the polymer. Gas bubbles can be generated by means of physical or chemical blowing agents. The final foam products usually possess better insulation properties, as well as higher degrees of impact resistance with respect to the starting material, thanks to the presence of the gas bubbles in the polymer melt [1].

There are many types of polymer foaming processes, such as foam extrusion, foam injection molding, compression molding, and micro-foaming [2, 3]. The final foam density depends on the original gas loading, the gas losses to the environment, and the foam expansion at quenching. The cell size and the cell size distribution depend on the intensity and kinetics of nucleation, on the characteristics of the bubble growth processes following

---

nucleation, and on the degree of cell wall collapsing, or cell coalescence, during expansion. Since the performance of foamed polymer is strongly related to many aspects of bubble growth, it is crucial to understand and control the bubble growth during the melt processing [1].

In the last few years the production of poly(ethylene terephthalate) (PET) foamed items, particularly sheets for insulating applications, is encountering a rising interest. Moreover, by the contrast to the commonly used thermoplastic resins, attention was paid to recycled materials [4, 5]. In order to increase the polymer viscosity and to enhance the foamability of recycled PET, various techniques have been investigated, including chain extension by reactive extrusion [4–10].

The results obtained with this technique are encouraging since it allows to perform in a single step the rheological upgrading of recycled polymer and foaming process.

However, in recent years the quality control requirements for plastic foamed products have become increasingly stringent. Therefore, researchers have attempted to optimize the foaming processes in order to produce high quality final products.

One of the most used methods for the optimization of the manufacturing process, as well as final product quality is numerical modeling: a large number of mathematical models for bubble growth were presented in the literature [11–21].

Some models have been written for bubble growth assumed to be governed by mass transfer alone, while others assumed momentum transfer alone. Using an integral method, the combination of these phenomena was presented by some authors. Extensive reviews and references can be found in a monograph edited by Lee and Ramesh [22].

The goal of this work is twofold:
– starting from preliminary results obtained in a previous work [7], the first goal of this work is to improve the process of extrusion foaming by chemical blowing agent (CBA) in order to produce high density foams from PET industrial scraps with a very low viscosity;
– the second goal of this work is to develop a simple and useful tool which can help the companies in choosing foaming conditions without performing complicated laboratory tests. With this aim, according to literature indications [11, 14, 16], the growth of a spherical bubble in a poly-

meric liquid has been theoretically studied by taking into account both mass transfer phenomenon and viscous forces effect. Moreover, with the aim of predicting the morphology of the final foam, a non isothermal model was developed. Model results were compared with experimental data obtained analyzing foamed sheets produced in laboratory starting from industrial scraps of PET and using a chemical blowing agent. The model was validated in relation to working conditions, chemical blowing agent percentage and initial rheological properties of recycled polymer.

2. Experimental

2.1. Materials

PET industrial scraps of low intrinsic viscosity, coming from the fibre production of a national company (Montefibre, Italy) were used. The chain extender used in this work is the Pyromellitic dianhydride (PMDA) purchased by Aldrich. The chemical modification, in the proportion required for the aim of extrusion foaming, is achieved with very low content of PMDA in PET; specifically three levels of PMDA contents were analyzed: 0.25, 0.50 and 0.75 weight% which proved to be the right compromise to tailor the required rheological modification and suitable foaming processability of PET. As far as the foam production is concerned, the choice was directed to a chemical foaming agent based process. In particular Hydrocerol CT 534, kindly supplied by Clariant, was used as a chemical foaming agent and specifically two levels of Hydrocerol contents were analyzed: 0.30 and 0.50 weight%. It was provided in powder form, and it is classified as an endothermic foaming agent, recommended for PET foaming, based on a mixture of both organic and inorganic foaming substances. The gas yielding during the process is reported as non toxic, presumably a blend of N_2, CO_2 and O_2 with a very low level of water.

2.2. Reactive and foaming processes

The reactive processing of PET with the PMDA and the foaming extrusion process were both performed with a Brabender single screw extruder ($D = 20$ mm, $L/D = 20$). The operation was accomplished in two steps.

Table 1. Operating conditions for chemical modification and foaming process

Reactive extrusion process	
Extruder temperature (hopper, barrel) [°C]	280, 280
Static mixer temperature [°C]	290
Die temperature [°C]	270
Screw speed [revolution per minute]	40
Foam extrusion process	
Extruder temperature (hopper, barrel) [°C]	270, 280
Die temperature [°C]	280
Extrusion die: slit die [mm²]	30×1
Screw speed [revolution per minute]	40

The main operative conditions for chemical modification and foaming process are reported in Table 1. The recycled PET was tailored by the chain extension reaction with the PMDA. The modified polymers were then used for the foam production.

2.2.1. Reactive processing

The reactive processing of PET with the PMDA was realized by making use of the mentioned extruder equipped with a static mixer to allow the required residence time for the reaction between PET and PMDA. The temperature profile used for the extrusion process was the following: extruder temperature (2 zones) 280°C; mixer temperature 290°C; die temperature 270°C. In Table 1, the working conditions for reactive process are reported.

Modified PET was characterized in terms of rheological properties (flow curves, melt strength and breaking stretching ratio (BSR)), mechanical properties (tensile and flexural properties) and densities.

Rheological properties

Rheological behavior of the modified PET was carefully analyzed in this work because this parameter strongly affects the foam morphology.

The dynamic flow properties of the polymer matrix produced by the chain extension process were measured with a Rheometrics Dynamic Spectrometer Mod. RDS-II (Rheometrics, Inc.) using a parallel plates geometry (plate radius = 25 mm; gap = 2 mm). Frequency sweep tests ($\omega = 0.1 \div 100$ rad/s were made at 280°C at a constant strain amplitude (10% strain) under a nitrogen gas purge in order to

minimize thermo-oxidative degradation phenomena.

Rheological measurement in shear flow were performed using a Capillary Extrusion Rheometer (Bohlin Instruments) with a die radius of 1 mm and a 16:1 length/diameter, equipped with a twin bore for the Bagley correction. Viscosity measurements were performed at 280°C within a shear rate range of $20 \div 10\,000$ s^{-1}. As the shear rate at the wall is greater for pseudoplastic than for Newtonian fluids at a given volumetric flow rate, the Rabinowitsch corrections were applied in all cases. The Capillary Extrusion Rheometer is equipped with a tensile module. The measurements were performed using a 1 mm diameter capillary die ($L/D = 20$) with the tensile module situated about 20 cm from the extrusion die. An extrusion temperature of 280°C and a wall shear rate of 125 s^{-1} were used. The tests allowed the determination of the melt strength and the breaking stretching ratio (BSR). The samples for testing were dried at 120°C in a vacuum oven for 12 h.

Mechanical properties and densities

The tensile properties were analyzed according to the standard ASTM D-638, the flexural ones were analyzed according to the standard ASTM D-790 and the densities were measured according to the standard ASTM D-1622.

2.2.2. Foaming process

The second step of processing consisted in the foam production by extruding the modified PET with the chemical blowing agent (CBA). Dry blends of treated PET and CBA powder were fed to the previously described extruder apparatus, which was operated without the static mixer. In Table 1 the working conditions for the processes of polymer foaming are reported. Further details on reactive process and foaming can be found elsewhere [7].

Foam produced was characterized in terms of rheological properties (flow curves, melt strength and BSR), mechanical properties (tensile and flexural properties), densities and finally in terms of cell size and cell size distribution by means of scanning electronic microscopy.

Cell size and cell distribution

Cell size and cell distribution was evaluated by means of electronic scanning microscopy (SEM).

In order to evaluate cell size and cell distribution from the SEM micrographs, a software for image analysis was developed and implemented in Labview (National Instruments). This software locates, counts, and measures objects in a rectangular search area. The software uses a threshold on the pixel intensities to segment the objects from their background. Optional filters give the capability to ignore the objects smaller or larger than given sizes. Other options allow rejecting the objects touching the borders of the search area and ignoring the holes that the segmentation process may create in the objects. The segmented objects are then located and measured. The software can also overlay on the image returned the position of the search area, the centers and bounding boxes of the objects detected.

3. Experimental results

3.1. Characterization of modified PET

Modified PET was characterized in terms of rheological properties (flow curves, melt strength and BSR), mechanical properties (tensile and flexural properties) and densities. In Table 2 main experimental results obtained analyzing modified PET samples were reported.

3.1.1. Rheological properties

Rheological behavior of the modified PET was carefully analyzed in this work because this parameter strongly affects the foam morphology.

A significant increase in viscosity due to the use of PMDA as chain extender in PET scraps (PET) is evident from the flow curves reported in Figure 1. These samples also exhibit a pronounced shear thinning behavior particularly the blend PET+ PMDA 0.75%.
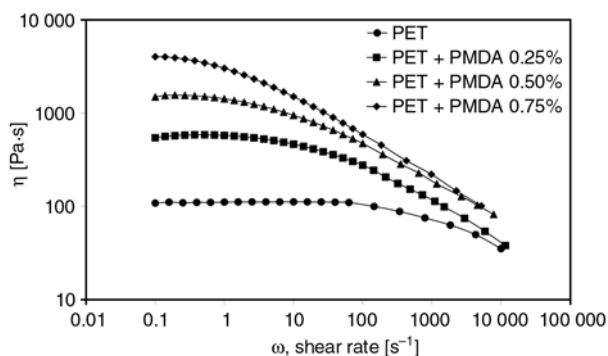

Figure 1. Flow curves for unmodified and modified PET samples (T=280°C)

Values of zero shear viscosity, obtained analyzing rheological data, are reported in Table 2 for unmodified and modified PET samples.

Moreover, in order to verify if the modified PET possesses melt properties suitable for foaming process, melt strength measurements were performed and the results being reported in Table 2. As it can be seen in Table 2, a sharp increase in melt strength is encountered with increasing PMDA content. Both the effects, the shear thinning behaviour and melt strength improvement, can be ascribed to the structural changes occurring during the chain extension process, i.e. the increase in M_w, the broadening of M_w/M_n and branching phenomena accomplished during the reactive extrusion. Actually, too large values of the MS tend to inhibit the bubble growth during the foaming process. As reported later, the parameters so obtained allow in all cases the production of foams, although with some differences. However, the sample treated with 0.50% of PMDA appears as the best accomplishment between the two parameters.

Since the polymer matrix was produced by a chain extension process, we considered the viscosity changing with the chain extender content using a polynomial fittings curve to interpolate the experimental data of η_0 vs. %PMDA [11] using Equation (1):

Table 2. Main properties of the modified PET samples

Code	%PMDA	η_0 [Pa·s] (T=280°C)	Melt strength [10^{-2} N]	BSR	Density [kg/m³]	η [dl/g]
PET	0	108	not meas.	not meas.	1410	0.49
PET_PMDA025	0.25	543	0.005	80	1414	0.59
PET_PMDA050	0.50	1275	0.012	120	1425	0.67
PET_PMDA075	0.75	3355	0.054	92	1435	0.77

$$\eta_0\,(\%PMDA) =$$

$$6577\,(\%PMDA)^2 - 742.64\,(\%PMDA) + 160 \quad (1)$$

Viscosity is related to temperature by an Arrhenius expression [23] and its variation with thermal profile is given by Equation (2):

$$\ln\frac{\eta_{0T}}{\eta_{0T_r}} = \frac{E_a}{R_g}\left(\frac{1}{T} - \frac{1}{T_r}\right) \quad (2)$$

where E_a is an activation energy for viscous flow (94 000 J/mol [23]), η_0 and η_{0T_r} are the zero shear viscosity corresponding to T and T_r, respectively. The effectiveness of the foaming process is strongly dependent on the viscosity of the polymer matrix and, consequently, on concentration of the chain extender. With an amount of PMDA lower than 0.5% no foam can be obtained.

3.2. Characterization of foam

Foam produced was characterized in terms of rheological properties (flow curves, melt strength and BSR), mechanical properties (tensile and flexural properties), densities and finally in terms of cell size and cell size distribution by means of scanning electronic microscopy. In Table 3 main experimental results obtained analyzing foamed samples were reported.

Data reported in Table 3 show that without significantly sacrifice the mechanical and physical properties (see results of tensile modulus and strength) it is possible to produce lightweight materials.

3.2.1. Cell size and cell distribution

The foamed strips obtained have a closed-cell structure (see SEM micrographs). Closed-cell foams are most suitable for thermal insulation and are produced when the cell membranes are sufficiently strong to withstand rupture at the maximum foam rise.
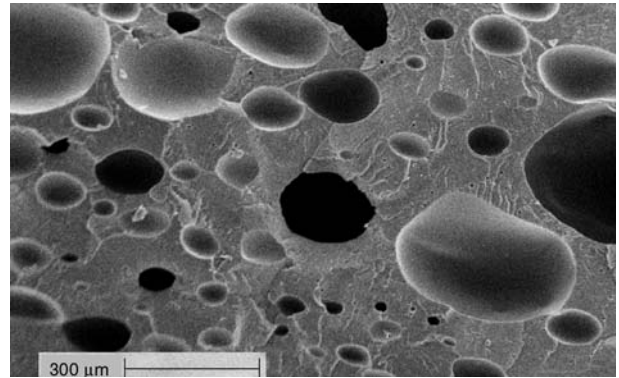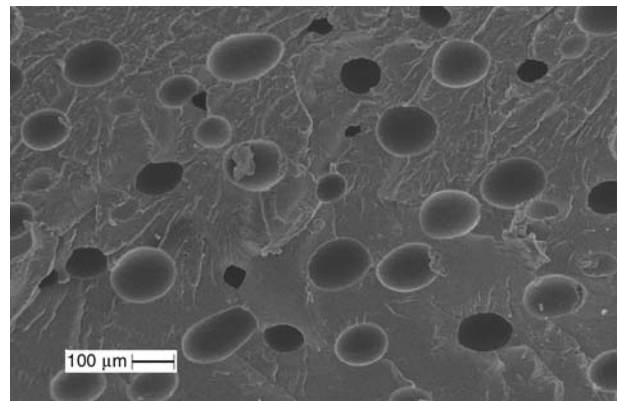

Figure 2. SEM micrograph PET_PMDA050_CBA05

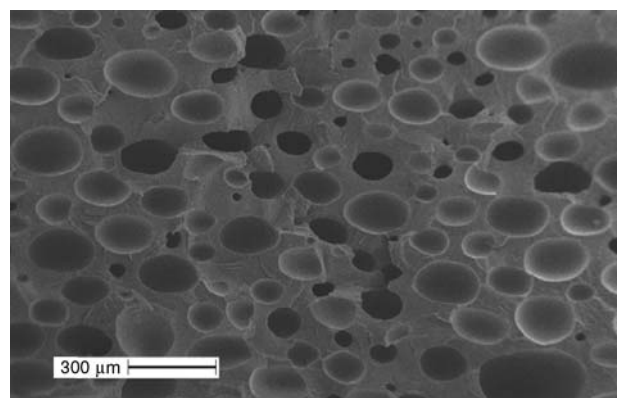**Figure 3.** SEM micrograph PET_PMDA075_CBA03

Figure 4. SEM micrograph PET_PMDA075_CBA05

Cell size and cell distribution was evaluated by means of electronic scanning microscopy (SEM). SEM micrographs of the cross section are reported in Figures 2–4 for the samples analyzed in this work.

Table 3. Main properties of the foamed samples

Code	%PMDA	%CBA	Density [kg/m³]	Tensile modulus [MPa]	Tensile strength [MPa]
PET	0	0	1410	1810	55.1
PET_PMDA050_CBA05	0.50	0.50	835	1240	23.4
PET_PMDA075_CBA03	0.75	0.30	1165	1365	29.5
PET_PMDA075_CBA05	0.75	0.50	900	1304	23.8

Table 4. The cell size and cell distribution for samples analyzed in this work

| Samples	N bubble [N/mm³]	Cell radius [μm]
PET_PMDA050_CBA05	~110	44 ± 15
PET_PMDA075_CBA03	~330	31 ± 10
PET_PMDA075_CBA05	~290	37 ± 15

Bubble dimensions, as evaluated by the image analysis software, are almost constant in the sample, confirming the assumption that temperature is constant along thickness direction.

The cell size and cell distribution, reported in Table 4, are strongly dependent, during the foaming process, on the concentration of the chain extender and, consequently, on the high viscosity of the polymer matrix.

4. Modeling

4.1. Bubble growth dynamics (Theoretical background)

Consider a polymer melt that has a dissolved gas concentration c_0 in equilibrium with the gas at some elevated pressure P_{B0}. With the release of pressure at $t = 0$, the solution becomes supersaturated, and nucleation and bubble growth begin. As the bubble growth proceeds, the pressure inside the bubble and the dissolved gas concentration at the bubble surface decrease. With time, gas diffuses into the bubble and a concentration gradient propagates radially in the polymer melt. A schematic of
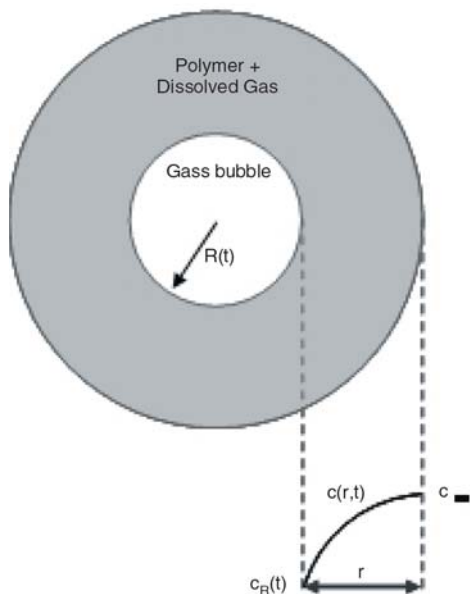
Figure 5. Schematic of single bubble growth

the bubble growth is shown in Figure 5. The radius and the dissolved gas concentration are denoted by $R(t)$ and $c(r,t)$.

In analyzing the bubbles growth process, the following assumptions can be made:

1. The bubble is spherically symmetric when it nucleates and remains so for the entire period of growth.
2. The gas pressure in the bubble $P_B(t)$ is related to the dissolved gas concentration at the bubble surface $c(R,t)$ by the Henry law: $c(R,t) = K_H P_B(t)$.
3. There are no chemical reactions during bubble growth.
4. Gravitational effects and latent heat of solution are neglected.
5. Inertial effects are neglected and the fluid is assumed to be incompressible and Newtonian.
6. The surface tension at the gas-liquid interface has a constant value σ.
7. The effect of foam densities on thermal conductivity of gas-filled polymeric bubble system is neglected.

The material properties such as polymer structure, molecular weight and its distribution, crystallinity and others are independent of the dissolved gas concentration and are ignored.

The neglect of inertia and the assumption of Newtonian behavior is imposed because the fluids are very viscous and the initial bubble growth rates are very small. Nevertheless, Amon and Denson [13] studied heat transfer analysis in polymer-gas systems in great detail. They found from reliable empirical correlations that the effective thermal conductivity of gas-filled polymeric bubble system changes by no more than a few percentage points over the whole range of foam densities. Moreover, as for thermoplastic foam extrusion, growth occurs in the molten-to-solid transition state. The polymer is cooled from 280°C (die temperature) to 25°C (ambient temperature) in a relatively short time: since in these circumstances all physical properties of the system undergo a rapid change, a transient heat transfer problem is considered here.

4.2. Governing equations for the bubble growth

In view of the above restrictions, the equation of motion, integral mass (gas) balance over the bubble and differential mass (dissolved gas) balance in the

surroundings mother phase take the following forms [14]. Equation of motion is given by Equation (3):

$$\frac{dR}{dt}=\frac{P_B-P_C}{4\eta}R-\frac{\sigma}{2\eta} \qquad (3)$$

The initial condition for the above equation is: $R(0) = R_i$. Here R_i is the initial radius of the bubble, P_C the pressure in the continuous phase, σ surface tension and η melt viscosity.

Integral mass (gas) balance over the bubble

A differential mass balance in a binary system assuming spherical symmetry, constant density and diffusion coefficient (D) is of the form of Equation (4):

$$\frac{\partial c}{\partial t}+v_r\frac{\partial c}{\partial r}=D\left[\frac{1}{r^2}\frac{\partial}{\partial r}\left(r^2\frac{\partial}{\partial r}\right)\right] \qquad (4)$$

where c is the dissolved gas concentration in the melt and D is the binary diffusion coefficient. The boundary and initial conditions for Equation (4) are given by Equation (5):

$$c(r,0)=c_i(r)$$
$$c(R,t)=c_R(t)=K_HP_B(t)$$
$$c(\infty,t)=c_\infty \qquad (5)$$

At a distance far from the bubble surface, the solution is not affected by the growing bubble and the dissolved gas concentration remains c_∞, the same as before the onset of nucleation. The quantity c_R is the dissolved gas concentration at the bubble surface. It is related to the gas pressure in the bubble through the solubility coefficient K_H. The quantity $c_i(r)$ is the initial concentration profile in the melt. The mass balance on the bubble requires that the rate of mass added to the bubble equals the rate that mass diffuses in through the bubble surface. Thus, a simple mass balance at the bubble surface relates the bubble pressure to the concentration gradient at the surface (see Equation (6)):

$$\frac{d}{dt}\left(\frac{4\pi}{3}\frac{P_BR^3}{Z_2R_gT}\right)=4\pi R^2D\frac{dc}{dr}\bigg|_{r=R} \qquad (6)$$

The initial condition for the above equation is $P_B(0)=P_{B0}$. Here P_{B0} is the initial bubble pressure,

Z_2 the compressibility factor of the gas inside the bubble, T temperature and R_g universal gas constant.

4.2.1. Dimensionless form of the governing equations

To facilitate the subsequent analysis, the following dimensionless variables and groups can be defined by Equations (7)–(15):

$$c_a=\frac{c-K_HP_C}{c_\infty-K_HP_C} \qquad (7)$$

$$P_{Ba}=\frac{P_B-P_c}{P_{B0}-P_c} \qquad (8)$$

$$r_a=\frac{r}{R_C} \qquad (9)$$

$$R_a=\frac{R}{R_C} \qquad (10)$$

$$t_a=\frac{t}{t_c} \qquad (11)$$

$$N_G=\frac{16\pi\sigma^3}{3k_BT(P_{B0}-P_c)^2} \qquad (12)$$

$$N_{Pe}=\frac{\sigma^2}{\eta D(P_{B0}-P_c)} \qquad (13)$$

$$N_{pi}=\frac{P_C}{P_{B0}-P_c} \qquad (14)$$

$$N_{si}=K_HRT \qquad (15)$$

In defining the above dimensionless quantities, we picked the critical bubble radius (Equation (16)):

$$R_C=\frac{2\sigma}{P_{B0}-P_C} \qquad (16)$$

and the critical momentum transfer time (Equation (17)):

$$t_C=\frac{4\eta}{P_{B0}-P_C}, \qquad (17)$$

as our characteristic bubble radius and bubble growth time, respectively.

In terms of the dimensionless variables, the equations governing the bubble growth dynamics takes the following forms (see Equations (18)–(20)):

$$\frac{dR_a}{dt_a} = P_{Ba} R_a - 1 \tag{18}$$

$$\frac{dP_{Ba}}{dt_a} =$$

$$\frac{3Z_2 N_{si}}{N_{Pe}} \frac{1}{R_a} \left. \frac{\partial c_a}{\partial r_a} \right|_{r_a = R_a} - \frac{3(P_{Ba} + N_{pi})}{R_a} \frac{dR_a}{dt_a} \tag{19}$$

$$\frac{\partial c_a}{\partial r_a} + \frac{R_a^2}{r_a^2} \frac{dR_a}{dt_a} \frac{\partial c_a}{\partial r_a} = \frac{1}{r_a^2 N_{Pe}} \frac{\partial}{\partial r_a} \left(r_a^2 \frac{\partial c_a}{\partial r_a} \right) \tag{20}$$

The corresponding initial and boundary conditions are given by Equations (21)–(25):

$$R_a(0) = R_{ai} \tag{21}$$

$$P_{Ba}(0) = PB_{ai} \tag{22}$$

$$c_a(r_a, 0) = c_{ai}(r_a) \tag{23}$$

$$c_a(R_a, t_a) = P_{Ba} \tag{24}$$

$$c_a(\infty, t_a) = 1 \tag{25}$$

Since the critical cluster represents an equilibrium state, this specification of the initial conditions will not produce bubble growth. To achieve the latter, we must perturb one or more of these variables from the equilibrium state. The bubble growth is a strong function of the value of the initial radius, arbitrary choice of it can lead to considerable error [11].

4.2.2. Initial conditions for bubble growth

In order to calculate the initial conditions for bubble growth, the approach used follows from Shafi *et al.* [11]. Following this procedure, we get the initial conditions for bubble growth (see Equations (26) and (27)):

$$R_a(0) = (1+A) + \frac{A(1+A)^2 N_{Pe}}{3N_{si}} \tag{26}$$

$$P_B(0) = 1 - \frac{A(1+A)(1+N_{pi}) N_{Pe}}{N_{si}} \tag{27}$$

where *A* is defined by Equation (28):

$$A = \left[1 + \left(\frac{3\pi}{4N_G} \right)^{\frac{1}{2}} \right]^{\frac{1}{3}} - 1 \tag{28}$$

The methodology for handling the transport processes around a single expanding bubble is valid for a bubble growing in an infinite expanse of liquid with no dissolved gas limitations. In actual foaming, there is a finite amount of dissolved gas that is continuously depleted by the simultaneous growth and nucleation of bubbles.

In order to extend the analysis in a finite amount of dissolved gas, in this work, the procedure presented by Shafi *et al.* [11] was adopted (see Figure 5). Shafi *et al.* applying the integral method to the present problem introduce an undetermined function of time, V_{cb}. Physically it represents the volume of the melt between the bubble surface and the radial position where the dissolved gas concentration approaches the initial dissolved gas concentration c_0. Moreover, they define two new variables: x, which represents the melt volume between the bubble surface and radial position r normalized to the volume of concentration boundary region V_{cb} and also a new concentration variable C as in Equations (29) and (30):

$$x = \frac{4\pi}{3} \frac{r^3 - R^3}{V_{cb}} \tag{29}$$

$$C = \frac{c - c_R}{c_0 - c_R} \tag{30}$$

Equations (29) and (30) transform a moving boundary problem with variable boundary conditions to a fixed boundary problem with constant boundary conditions. *C* is always 0 at the bubble surface ($x = 0$), and is 1 at the far end of the concentration boundary ($x = 1$) and it can be assumed as a function of x only. In view of Equations (29) and (30) and defining additional dimensionless variables and groups as shown in Equations (31) and (32):

$$c_{Ra} = \frac{c_R - K_H P_B}{c_0 - K_H P_B} \tag{31}$$

$$V_{cba} = \frac{3V_{cb}}{4\pi R_c^3} \qquad (32)$$

the equations governing the bubble growth dynamics in terms of dimensionless quantities can be rewritten by Equations (33)–(35):

$$\frac{dR_a}{dt_a} = c_{R_a} R_a - 1 \qquad (33)$$

$$\frac{dc_{Ra}}{dt_a} =$$

$$\frac{9N_{si}Z_2}{N_{Pe}} \frac{(1-c_{Ra})R_a}{V_{cba}} \left.\frac{dc}{dx}\right|_{x=0} - \frac{3(c_{Ra}+N_{pi})}{R_a} \frac{dR_a}{dt_a} \qquad (34)$$

$$V_{cba} = \frac{(c_{Ra}+N_{pi})R_a^3 - (1+N_{pi})}{N_{si}(1-c_{Ra})\int_0^1 (1-C)dx} \qquad (35)$$

With the initial conditions given by Equations (36) and (37):

$$R_a(0) = (1+A) + \frac{A(1+A)^2 N_{Pe}}{3N_{si}} \qquad (36)$$

$$c_R(0) = 1 - \frac{A(A+1)(1+N_{pi})N_{Pe}}{N_{si}} \qquad (37)$$

4.3. Model formulation

In order to calculate the evolution of the bubbles size in the foam sheet starting from material properties and working conditions, the model above described was implemented in a simulation code developed in Labview (National Instruments). With this aim Equations (33)–(35) must be solved with the initial conditions given by Equations (36) and (37). Moreover, as for thermoplastic foam extrusion, growth occurs in the molten-to-solid transition state. The polymer is cooled from 280°C (die temperature) to 25°C (ambient temperature). Rheological property variation certainly changes the isothermal growth scenario and hence, a transient heat transfer problem is considered here. The polymer is cooled by means of two cooling fans, in

this case, the energy equation combined with Fourier's law of heat conduction, is given by Equation (38):

$$\frac{\partial T}{\partial t} = \frac{k_P}{\rho_P C_{p,P}} \frac{\partial^2 T}{\partial x^2} \qquad (38)$$

where ρ_P, $C_{p,P}$ and k_p are density, specific heat and thermal conductivity, respectively.

The initial and boundary conditions are then given by Equation (39):

$$T = T_0, \ t = t_0$$
$$\frac{\partial T}{\partial x} = 0, \ x = 0$$
$$\frac{\partial T}{\partial x} = h(T - T_{AIR}), \ x = \delta \qquad (39)$$

where δ is the half-thickness of the foam sheet, T_0 is the initial temperature of the polymer (die temperature), T_{AIR} is the ambient temperature and h is the heat transfer coefficient.
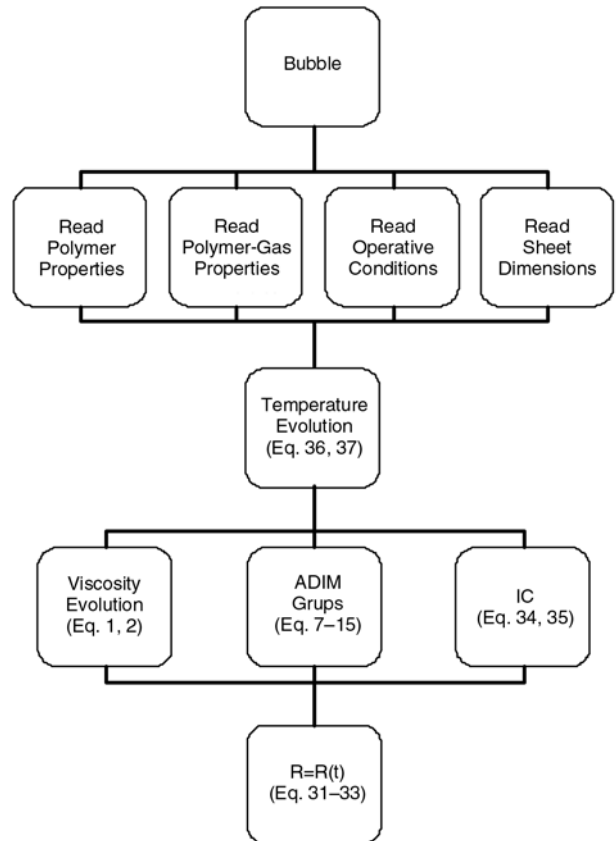

Figure 6. Flow chart describing the sequence of the calculations in the model

A flow chart describing the sequence of the calculations is reported in Figure 6. In Table 5, the main variables involved in the model are reported.

4.3.1. Solution methodology

The equations governing the bubble growth dynamics are highly nonlinear and stiff. These equations were solved using the Gear's method. The nonlinear equations are solved by Brown's method. The equations were solved using a finite difference scheme.

It is worth mentioning that in the model adopted in this work there are no involved adjustable parameters so that the model starting from data of materials properties and the operative conditions is able to predict bubble dimensions.

5. Model results

Model developed in this work following the literature indications allows to calculate the evolution of the temperature, of the bubble pressure and radius starting from the operative conditions and material properties (Tables 1 and 6). Consistently with experimental data, with an amount of chain extender lower that 0.5% according to the model the clusters are not sufficiently large compared to the critical cluster in order to grow spontaneously to a macroscopic bubble and no foam can be obtained. In Figure 7, the calculated evolution of temperature and bubble radius during the foaming process are reported for PET_PMDA050_CBA05 and PET_PMDA075_CBA05. Figures show that bubbles growth takes about one second, after this time temperature become too low and viscosity too high.

Table 5. Main variables involved in the model adopted in this work

σ	surface tension	D	binary diffusion coefficient
η	melt viscosity	Z_2	compressibility factor of the gas
K_H	solubility coefficient	R_g	Universal gas constant
P_{B0}	initial bubble pressure	c_∞	initial gas concentration
R_i	initial radius of the bubble	$c_i(r)$	initial gas concentration profile
$R(t)$	bubble radius	$c(r,t)$	dissolved gas concentration
$P_B(t)$	gas pressure in the bubble	$c(R,t)=c_R$	dissolved gas concentration at the bubble surface
P_C	Pressure in the continuous phase		
V_{cb}	volume of the melt between the bubble surface and the radial position where the dissolved gas concentration approaches the initial dissolved gas concentration c_0		

Table 6. Physical properties [23] and operative conditions used in the model

Physical properties	Operative conditions
PET specific heat C_p	1130 J/(kg·K)
Thermal conductivity K	0.218 W/(m·K)
Activation energy for viscous flow E_a	94 000 J/mol
Rheological reference temperature	553 K
Surface tension σ	0.0446 N/m
Diffusivity	$3 \cdot 10^{-12}$ m^2/s
Die pressure	$1.5 \cdot 10^6$ Pa
Ambient pressure	$1.01 \cdot 10^5$ Pa
Die temperature T_0	543 K

In Figure 8, the calculated evolution of bubble pressure and radius during the foaming process are reported for PET_PMDA050_CBA05 and PET_PMDA075_CBA05.
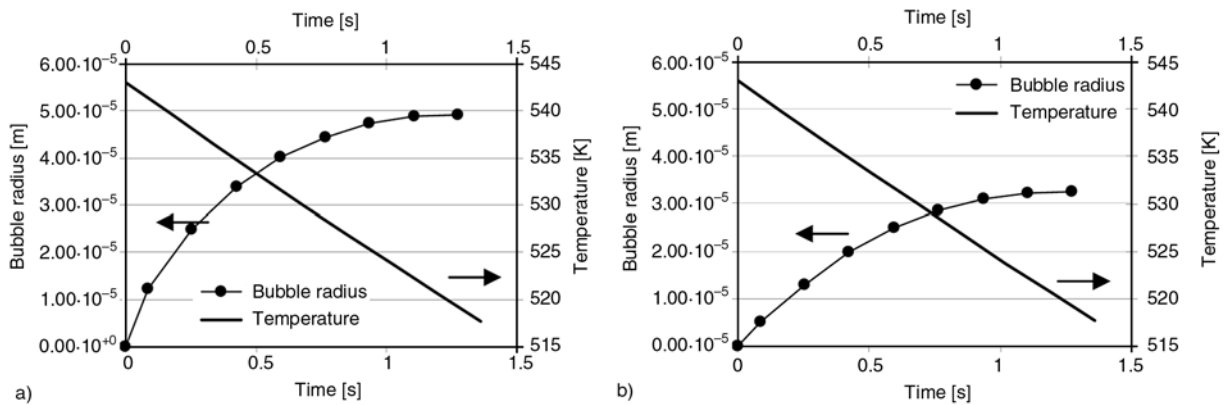

Figure 7. Temperature profile for the bubble growth simulation of extrusion. a – PET_PMDA050_CBA05; b – PET_PMDA075_CBA05
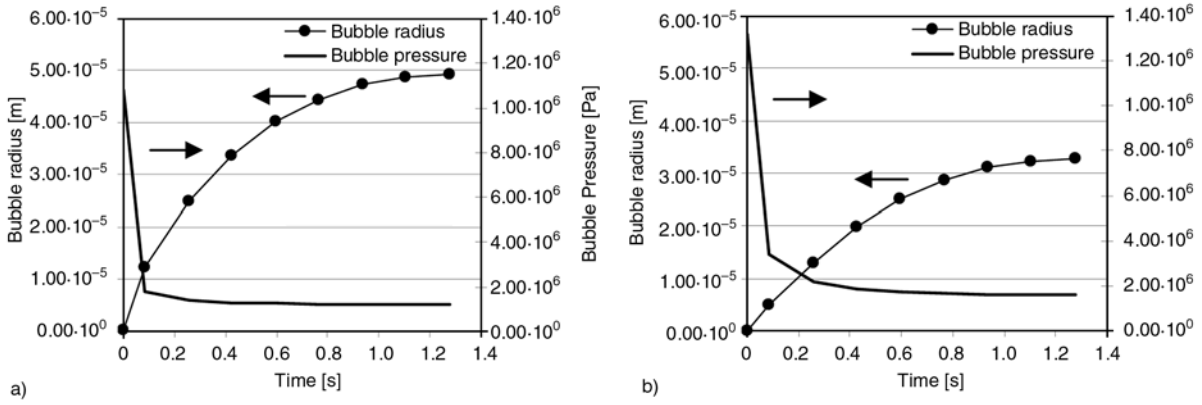
Figure 8. Pressure profile for the bubble growth simulation of extrusion foaming, a – PET_PMDA050_CBA05; b – PET_PMDA075_CBA05
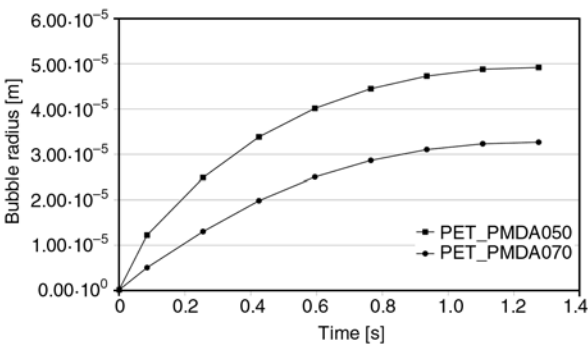

Figure 9. Evolution of the bubble radius for PET_PMDA050_CBA05 and PET_PMDA075_CBA05
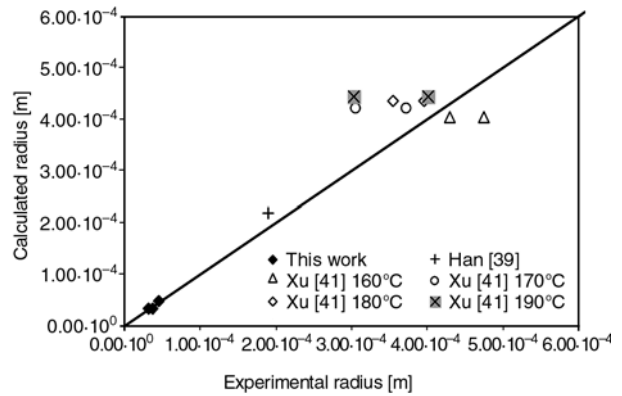

Figure 10. Comparison between experimental results and model prediction for the bubble radius (literature data are also reported in figure)

Table 7. Comparison between experimental results and model prediction for the bubble radius

Samples	Experimental cell radius [μm]	Calculated cell radius [μm]
PET_PMDA050_CBA05	44 ± 15	49
PET_PMDA075_CBA03	31 ± 10	33
PET_PMDA075_CBA05	37 ± 15	33

The bubble pressure start from a maximum and decreases to a value close to the ambient pressure. The evolution of the bubble radius for the samples analyzed in this work was compared in Figure 9. As it can be seen from the figure, the radius of the bubbles in the sample coded as PET_PMDA050_CBA05 is bigger than the one of the bubbles in PET_PMDA075_CBA05. From figure the effect of the PMDA content is evident, in fact, the bubble radius increases on decreasing of the PMDA content: this is mainly due to the higher melt strength (shown by the PET_PMDA075_CBA05) which limits the growth of the bubbles.

The comparison between experimental results and model prediction for the bubble radius is reported in Figure 10. Because at the moment only few experimental data are available, literature data [25, 26] are also reported in figure. Moreover, the model described in this work was adopted in order to calculate the evolution of the bubble radius in literature experimental conditions and results were also reported in figure. The satisfactorily agreement

between literature experimental data and model predictions is a further validation of the model adopted in this work.

In order to underline results achieved in this work, the comparison between experimental results and model prediction for the bubble radius for PET_PMDA050_CBA05, PET_PMDA075_CBA03, PET_PMDA075_CBA05 is reported in Table 7. Comparison shows that model seems to be able to predict experimental data of bubble radius, even if, at the moment only few experimental data are available.

The comparison between experimental data and model prediction shown in Figure 10 is satisfactorily, however, better results of prediction of the evolution of the bubble radius during foaming process could be achieved by means of a better rheological description, that is adopting more complex models which better describe viscoelastic properties of the material.

5. Conclusions

In this work, the process of extrusion foaming by chemical blowing agent (CBA) was improved in order to produce high density foams from PET industrial scraps with a very low viscosity. Due to the low intrinsic viscosity of the recycled PET (IV = 0.48 dl/g), a chain extender was also used in order to increase the molecular weight of the polymer matrix. The reactive processing of PET and the foaming extrusion process were both performed with a Brabender single screw extruder. The operation was accomplished in two steps. The chemical modification, in the proportion required for the aim of extrusion foaming, is achieved with very low content of PMDA in PET; specifically three levels of PMDA contents were analyzed: 0.25, 0.50 and 0.75 weight% which resulted to be the right compromise to tailor the required rheological modification and suitable foaming processability of PET. As far as the foam production is concerned, the choice was directed to a chemical foaming agent based process. In particular Hydrocerol CT 534 was used as a chemical foaming agent and specifically two levels of Hydrocerol contents were analyzed: 0.30 and 0.50 weight%.

Modified PET was characterized in terms of rheological properties (flow curves, melt strength and BSR), mechanical properties (tensile and flexural properties) and densities. Foam produced was characterized in terms of rheological properties (flow curves, melt strength and BSR), mechanical properties (tensile and flexural properties), densities and finally in terms of cell size and cell size distribution by means of scanning electronic microscopy.

Finally, the growth of a spherical bubble in a polymeric liquid has been theoretically studied by taking into account both mass transfer phenomenon and viscous forces effect.

Model results were compared with experimental data obtained analyzing foamed sheets produced in laboratory starting from industrial scraps of PET. As for thermoplastic foam extrusion, growth occurs in the molten-to-solid transition state. Rheological property variation certainly changes the isothermal growth scenario and hence, a transient heat transfer problem is considered and a non isothermal model for bubble growth was developed.

The model was validated in relation to working conditions, chemical blowing agent percentage and initial rheological properties of recycled polymer. A good agreement between experimental and calculated data was achieved, even if, at the moment only preliminary experimental data are available.

In order to achieve a better understanding of the foaming process, future work will consider an additional validation by comparing model results with a wider set of experimental data and the analysis of the bubble nucleation.

References

[1] Lee C. H., Lee K-J., Jeong H. G., Kim S. W.: Growth of gas bubbles in the foam extrusion process. Advances in Polymer Technology, **19**, 97–112 (2000). DOI: 10.1002/(SICI)1098-2329(200022)19:2<97::AID-ADV3>3.0.CO;2-B

[2] Kumar V., Suh N. P.: Process for making microcellular thermoplastic parts. Polymer Engineering and Science, **30**, 1323–1329 (1990). DOI: 10.1002/pen.760302010

[3] Baldwin D. F., Suh N. P., Park C. B., Cha S. W.: Supermicrocellular foamed materials, U.S. Patent 5334356, USA (1994).

[4] Xanthos M., Dey S.: Foam extrusion of polyethylene terephthalate (PET). in 'Foam extrusion: Principles and practice' (ed.: Lee S. T.) Technomic, Lancaster, 307–336 (2000).

[5] Branch G. L., Wardle T.: Manufacture of fully recyclable foamed polymer from recycled material. International Patent PCT/US2004/015245 (2004).

[6] Incarnato L., Scarfato P., Di Maio L., Acierno D.: Structure and rheology of recycled PET modified by reactive extrusion. Polymer, **41**, 6825–6831 (2000). DOI: 10.1016/S0032-3861(00)00032-X

[7] Di Maio L., Coccorullo I., Montesano S., Incarnato L.: Chain extension and foaming of recycled PET in extrusion equipment. Macromolecular Symposia, **228**, 185–200 (2005). DOI: 10.1002/masy.200551017

[8] Awaja F., Dumitru P.: Statistical models for optimisation of properties of bottles produced using blends of reactive extruded recycled PET and virgin PET. European Polymer Journal, **41**, 2097–2106 (2005). DOI: 10.1016/j.eurpolymj.2005.04.010

[9] Japon S., Boogh L., Leterrier Y., Manson J. A. E.: Reactive processing of poly(ethylene terephthalate) modified with multifunctional epoxy-based additives. Polymer, **41**, 5809–5818 (2000). DOI: 10.1016/S0032-3861(99)00768-5

[10] Awaja F., Pavel D.: Injection stretch blow moulding process of reactive extruded recycled PET and virgin PET blends. European Polymer Journal, **41**, 2614–2634 (2005). DOI: 10.1016/j.eurpolymj.2005.05.036

[11] Shafi M. A., Lee J. G., Flumerfelt R. W.: Prediction of cellular structure in free expansion polymer foam processing. Polymer Engineering and Science, **36**, 1950–1959 (1996). DOI: 10.1002/pen.10591

[12] Venerus D. C.: Diffusion-induced bubble growth in viscous liquids of finite and infinite extent. Polymer Engineering and Science, **41**, 1390–1398 (2001). DOI: 10.1002/pen.10839

[13] Amon M., Denson C. D.: A study of the dynamics of foam growth: Analysis of the growth of closely spaced spherical bubbles. Polymer Engineering and Science, **24**, 1026–1034 (1984). DOI: 10.1002/pen.760241306

[14] Favelukis M., Zhang Z., Pai V.: On the growth of a non-ideal gas bubble in a solvent-polymer solution. Polymer Engineering and Science, **40**, 1350–1359 (2000). DOI: 10.1002/pen.11264

[15] Ramesh N. S., Rasmussen D. H., Campbell G. A.: The heterogeneous nucleation of microcellular foams assisted by the survival of microvoids in polymers containing low glass transition particles. Part I: Mathematical modeling and numerical simulation. Polymer Engineering and Science, **34**, 1685–1697 (1994). DOI: 10.1002/pen.760342206

[16] Patel R. D.: Bubble growth in a viscous Newtonian liquid. Chemical Engineering Science, **35**, 2352–2356 (1980).

[17] Joshi K., Lee J. G., Shafi M. A., Flumerfelt R. W.: Prediction of cellular structure in free expansion of viscoelastic media. Journal of Applied Polymer Science, **67**, 1353–1368 (1998). DOI: 10.1002/(SICI)1097-4628(19980222)67: 8<1353::AID-APP2>3.0.CO;2-D

[18] Yue P., Feng J. J., Bertelo C. A., Hu H. H.: An arbitrary Lagrangian-Eulerian method for simulating bubble growth in polymer foaming. Journal of Computational Physics, **226**, 2229–2249 (2007). DOI: 10.1016/j.jcp.2007.07.007

[19] Otsuki Y., Kanai T.: Numerical simulation of bubble growth in viscoelastic fluid with diffusion of dissolved foaming agent. Polymer Engineering and Science, **45**, 1277–1287, (2005). DOI: 10.1002/pen.20395

[20] Everitt S. L., Harlen O. G., Wilson H. J.: Competition and interaction of polydisperse bubbles in polymer foams. Journal of Non-Newtonian Fluid Mechanics, **137**, 60–71 (2006). DOI: 10.1016/j.jnnfm.2006.03.005

[21] Favelukis M.: Dynamics of foam growth: Bubble growth in a limited amount of liquid. Polymer Engineering and Science, **44**, 1900–1906 (2004). DOI: 10.1002/pen.20192

[22] Lee J. G., Ramesh N. S.: Polymeric foams: Mechanisms and materials. CRC Press, New York (2004).

[23] Van Krevelen D. W.: Properties of polymers. Elsevier, New York (1990).

[24] Amon M., Denson C. D.: A study of the dynamics of foam growth: Simplified analysis and experimental results for bulk density in structural foam molding. Polymer Engineering and Science, **26**, 255–267 (1986). DOI: 10.1002/pen.760260311

[25] Han C. D., Yoo H. J.: Studies on structural foam processing. 4. Bubble growth during mold filling. Polymer Engineering and Science, **21**, 518–533 (1981).

[26] Xu D., Pop-Iliev R., Park C. B., Fenton R. G., Jiang H.: Fundamental study of CBA-blown bubble growth and collapse under atmospheric pressure. Journal of Cellular Plastics, **41**, 519–538 (2005). DOI: 10.1177/0021955X05059031

Synthesis and characterization of a novel temperature-pH responsive copolymer of *2*-hydroxypropyl acrylate and aminoethyl methacrylate hydrochloric salt

K. L. Deng, H. Tian, P. F. Zhang, X. B. Ren, H. B. Zhong*

College of Chemistry & Environmental Science, Hebei University, Baoding 071002, China

Abstract. In this investigation, a novel temperature-pH responsive copolymer was prepared by the radical copolymerization between *2*-hydroxypropyl acrylate (HPA) and aminoethyl methacrylate hydrochloric salt (AMHS). The molecular structure of the corresponding copolymer has been confirmed by ^{1}H NMR and FTIR measurements. The results indicated that the lower critical solution temperature (LCST) of the resulting copolymer has shown a considerable dependence on the monomer ratio and pH value in the medium. When the molar ratio of HPA to AMHS unit on polymer chain was fixed at 1.56, 2.25, and 3.01, the LCSTs of copolymers were observed at 36.5, 28.2 and 17.8°C, respectively. For the effect of additive salts, the LCST change of the copolymer was affected by both cations and anions in the following order of $Al(NO_3)_3$ > KNO_3 > $Mg(NO_3)_2$ > $NaNO_3$ and $KCl \approx KSCN$ > KBr > KNO_3 > KI. The copolymer seems to be useful as a candidate for the controlled-drug release carrier by pH and temperature external stimuli.

Keywords: smart polymers, temperature-pH responsive polymer, lower critical solution temperature

1. Introduction

In recent years, the responsive polymers have attracted considerable interest for their chemical or physical property changes in response to the external stimuli such as temperature, pH, specific ions, and electric field [1]. As the important responsive polymers, the temperature or pH-responsive polymers are widely applied in many fields including drug-delivery system [2], chemical separation [3], and gene carriers [4].

The thermo-sensitive polymers reversibly become a uniform sphere from a random coil chain in the solution at a certain temperature, namely, the lower critical solution temperature (LCST) [5]. These phenomena can also be observed when other external parameters are changed such as pH value [6], electric field [7], and ionic strength [8]. Normally,

the LCST value of polymer is greatly affected by the balance of the hydrophilic and hydrophobic groups in the polymer. In other words, the hydrophilic and hydrophobic interactions between the polymer chains play a significant role in determining their LCST value. The two interactions in nature are related to the hydrophobic interaction among polymers and to hydrophilic interaction (hydrogen bonding) between hydrophilic groups of polymer and water molecules. If the excessively hydrophilic or hydrophobic groups are attached to the polymer backbone, no thermo-sensitivities of the polymers are observed under common conditions. It has been reported that the change of hydrophilic/hydrophobic groups on the macromolecular chains leads to several thermo-sensitive polymers with different LCST values. Such poly-

---

mers include poly(*N,N'*-diethyl acrylamide) [1], poly(*N*-isopropylacrylamide) [9], poly(*2*-isopropyl-*2*-oxazoline) [10] , and poly(vinyl methyl ether) [11] and so on. For example, Schild [12] reported that the LCST of a thermo-responsive polymer containing *N*-isopropylacrylamide was controlled by the content of hydrophilic amide groups and hydrophobic groups. In addition, in order to get polymers with much better controlled temperature-responsive properties, some copolymers were synthesized by the introduction of other monomers or natural polymers. The various copolymers were prepared to meet the demands in many fields, such as poly(*N*-isopropylacrylamide-*co*-acrylamide-*co*-hydroxyethylmethacrylate) [13], poly(*N,N*-dimethyl-acrylamide-*b*-*N*-isopropylacrylamide-*b*-*N*-acryloyl-valine) [14], poly(*N*-isopropylacrylamide/carboxy-methyl chitosan) [15], and poly(*N*-isopropylacry-lamide-*co*-diethyleneglycol methacrylate) [16].

2-Hydroxypropyl acrylate (HPA) is extensively applied in fibre, adhesives, rubber industry, paints and coatings industry [17]. To the best of our knowledge, the preparation of the copolymer between HPA and AMHS as a temperature-responsive material has not been reported in the literature. By varying the monomer ratio in the copolymerization of HPA and AMHS, the balance between hydrophobicity and hydrophilicity on the copolymer chain can be effectively controlled to some extent. Accordingly, HPA/AMHS copolymer may theoretically exhibit a reversible temperature-responsive property. The incorporation of AMHS into the macromolecular chain may produce a pH-responsive copolymer, because AMHS is a kind of weak-base/strong-acid salt. The copolymer also responds to inorganic ion stimuli and shows a phase transition.

The aim of this study was to prepare a novel copolymer of HPA and AMHS and evaluate the dual responsiveness (temperature and pH) in its aqueous solution. The molecular structure of the resulting copolymer and the monomer was characterized by ^{1}H NMR and FTIR measurements. By varying the ratio of HPA to AMHS, the hydrophilic and hydrophobic balance of the resulting copolymer was adjusted effectively. When the molar ratio of HPA to AMHS unit on polymer chain was fixed at 1.56, 2.25, and 3.01, the LCSTs of copolymers in the aqueous solution were found to be 36.5, 28.2 and 17.8°C, respectively. Furthermore, a series of

inorganic salts were selected to evaluate the salt effect on LCST of the resulting copolymer.

2. Experimental section

2.1. Materials

2-aminoethanol, propylene oxide and benzoyl chloride were purchased from Dongfang health materials factory (Tianjin, China) and Huadong Chemical Factory (Tianjin, China), respectively. Acrylic acid and methacrylic acid were purified by vacuum distillation. Potassium persulfate (KPS) was recrystallized from deionized water before used. The other solvents were analytical grade and used without any further purification.

2.2. Measurements

Fourier-transform infrared spectra (FTIR) of the monomer and the corresponding copolymers were recorded on a Vector22 FT-IR spectrophotometer with KBr pellet in the range of 400–4000 cm^{-1}. ^{1}H NMR spectra were measured with a Bruker Avance-400 (400 MHz) using D_2O as solvent and TMS as internal standard. The thermo-sensitivities of the copolymer in the solution were detected by monitoring the optical transmittance at 500 nm on a Shimadzu UV-120-02 spectrophotometer with a thermally-controlled cuvette holder. The heating rate was controlled at 0.5°C/min in our experiment. The temperature at which the transmittance of the copolymer solution decreased to half of the initial value during heating was defined as LCST for the copolymers in our study.

2.3. Synthesis of HPA and AMHS

2-aminoethanol hydrochloride was prepared via the neutralization of *2*-aminoethanol with the calculated amount of hydrochloride solution and complete drying under vacuum at 70°C. Methacryloyl chloride was synthesized by reacting methacrylic acid with benzoyl chloride according to the literature [18]. The mixture of *2*-aminoethanol hydrochloride and methacryloyl chloride with an excess of 10% was heated up to 75°C and the temperature was maintained for 2 h. Then, it was cooled and dissolved in tetrahydrofuran. The solution of the crude AMHS was poured into ethyl ether to remove the un-reacted methacryloyl chloride. The pure

AMHS, a white powder, was obtained after filtration with a yield of 81%.

FTIR [cm^{-1}] for AMHS: 3381, 3044 (broad v_{N-H}), 2974–2887 (strong v_{C-H}), 1720 (strong $v_{C=O}$), 1622 (weak $v_{-C=C-}$), 1494 (median δ_{N-H}), 1064 (strong v_{C-O-C}).

0.28 mol propylene oxide, 0.2 mol acrylic acid, a trace amount of CuCl as inhibitor and pyridine as catalyst were added into the round flask with a condenser. The mixture was heated to 90°C and kept for 4 h. Finally, the isomers (HPA) containing *2-hydroxypropyl acrylate* and *2-hydroxyisopropyl acrylate* were obtained after vacuum distillation with a yield of 63%. From ^{1}H NMR measurement, HPA was composed of pure *2-hydroxypropyl acrylate* and *2-hydroxyisopropyl acrylate*, and the molar ratio of two isomers was about 1.7:1.

FTIR [cm^{-1}] for HPA: 3420 (broad v_{O-H}), 2977–2885 (strong v_{C-H}), 1720 (strong $v_{C=O}$), 1617 (weak $v_{-C=C-}$), 1194 (strong $v_{O-C=O}$), 1080 (strong v_{C-O-C}).

2.4. Synthesis of the copolymers from HPA and AMHS

A series of the copolymers with various feed ratios of HPA to AMHS were synthesized by the conventional radical copolymerization using $K_2S_2O_8$-NaHSO$_3$ as the redox initiator. In the polymerization, the molar ratio of monomers to initiator was fixed at 100:1 and the total monomer concentration was 0.3 mol/l in the deionized water. The Schlenk tube was added with the required amount of $K_2S_2O_8$-NaHSO$_3$ initiator, HPA, AMHS and deionized water. After degassing with dry nitrogen, the reaction mixture was magnetically stirred for 10 h at room temperature. Finally, the resulting mixture was precipitated into cold sodium chloride solution to remove the residual HPA, AMHS and un-reacted initiator. After several washing with hot water, the title copolymer was obtained via filtration and dried under vacuum at 60°C for 48 h. When the ratio of HPA to AMHS was fixed at 1, 2, 3 and 4 in the copolymerization, the corresponding copolymers were designated as PHA1, PHA2, PHA3, and PHA4. From ^{1}H NMR measurements, The molar ratio of HPA to AMHS on polymer chain for PHA1, PHA2, PHA3, and PHA4 were 0.75:1, 1.56:1, 2.25:1 and 3.01:1, respectively.

3. Results and discussion

3.1. Molecular design for the temperature-pH sensitive polymers

The synthetic route for the copolymer studied in this paper is shown in Figure 1. We firstly prepared nonionic HPA and ionic AMHS monomer. The temperature-pH responsive copolymer of two monomers was obtained by solution polymerization initiated with $K_2S_2O_8$-NaHSO$_3$. Herein, the HPA monomer units on the copolymer chains serve as the hydrophobic moieties and AMHS units function as the hydrophilic groups. The modulation of hydrophobicity and hydrophilicity on the polymer
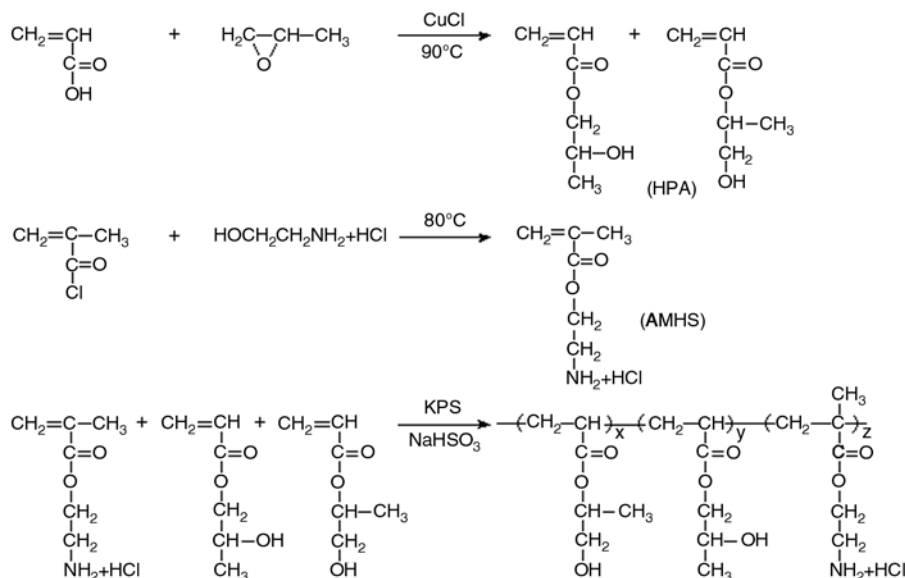

Figure 1. Synthetic route for the temperature-pH sensitive polymer

chains was achieved via changing the ratio of HPA to AMHS in the polymerization. It was found that only the corresponding copolymers with given monomer ratio did show a reversible thermo-sensitiveness. In contrast with this result, no LCST was observed in the aqueous solutions of poly(AMHS). The reason is attributed to the following fact that too high hydrophilic interactions allow the homopolymer of AMHS to completely dissolve in water. Accordingly, the appropriate balance between hydrophobicity and hydrophilicity on the polymer chains plays a crucial role in preparation of thermo-responsive polymer.

3.2. Structural confirmation of the copolymer from HPA and AMHS

The FTIR spectrum and the ^{1}H NMR spectrum of PHA4 were recorded in order to confirm the structure of the copolymer. As shown in Figure 2 of PHA4 FTIR spectrum, the broad peaks from about 3600 to 3250 cm^{-1} suggested the presence of the –OH and –NH$_2$·HCl groups. The strong characteristic absorption at 1735.8 cm^{-1} was observed, which was ascribed to the characteristics stretching vibration of C=O group from HPA and AMHS repeating units. Also, the absorption bands at 1176.2 cm^{-1} could be attributed to the C–O–C stretching vibration. In the ^{1}H NMR spectrum of PHA4 shown in Figure 3, the main peaks of the

copolymer PHA4 were found. For example, the peaks at 4.06 and 3.61 ppm were ascribed to methylene and methine groups in [–OC$\underline{H}_2$C$\underline{H}$(OH)CH$_3$] repeating unit. The chemical shift of methylene and methine groups in [–OC$\underline{H}_2$C$\underline{H}$(OH)CH$_3$] repeating unit was also observed at 3.61 and 4.06 ppm. The peaks for the two methylene groups [–OC$\underline{H}_2$C$\underline{H}_2$NH$_2$·HCl] in AMHS unit were recorded at 4.21 and 3.32 ppm respectively. Here, the peak at 4.9 ppm possibly indicated the existence of –NH$_2$ groups in the AMHS repeating unit. It is necessary to state that no peaks for –OH group were found in the measurement using D$_2$O as solvent. The above-mentioned spectral data confirmed the structure of the target copolymer. In addition, the molar ratio of HPA to AMHS on polymer chain for PHA1, PHA2, PHA3, and PHA4 were found to be 0.75:1, 1.56:1, 2.25:1 and 3.01:1, respectively, from ^{1}H NMR results.
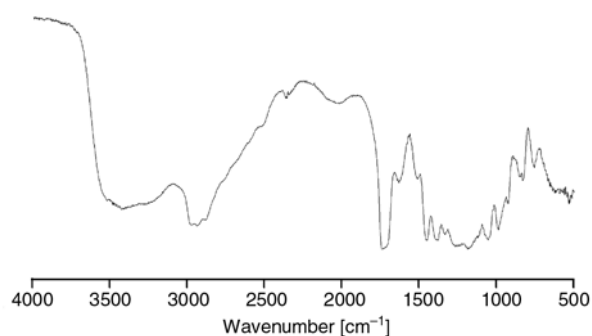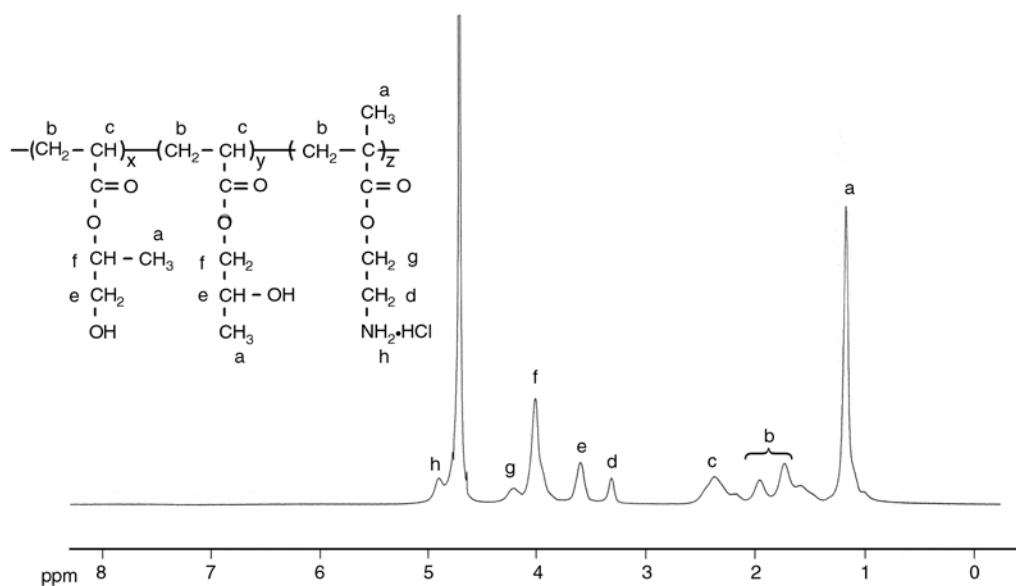

Figure 2. FTIR spectrum of the PHA4

Figure 3. ^{1}H NMR spectrum of the PHA4

3.3. Effect of the different factors on LCST

3.3.1. Effect of copolymer concentration in aqueous solution on LCST

In this study, the temperature at which the transmittance decreased to half of the initial value was defined as the LCST. For the thermo-sensitive polymer, a clear aqueous copolymer solution below LCST became cloudy upon heating. A typical optical transmittance of the solution of PHA3 as a function of temperature is shown in Figure 4. Clearly, the PHA3 precipitated out from the aqueous solution at temperature around 25–45°C range, depending on its concentration. The LCST value decreased as the polymer concentration increased. When PHA3 concentration was 1 wt%, its LCST was about 40°C. As PHA3 concentration was increased to 2 and 3 wt%, the LCSTs of PHA3 reached about 28.2 and 30.1°C, respectively. This result shows no remarkable dependence of LCST upon the concentration values at higher copolymer concentration. Additionally, the phase transition interval is more than 10°C for PHA3 copolymers. The reason for this observation can be probably ascribed to the wider molecular weight distribution of copolymer or the different sequence of the monomer unit on copolymer chain. The wider phase transition temperature was also reported in another copolymer system from *2*-hydroxylpropyl acrylate [19].
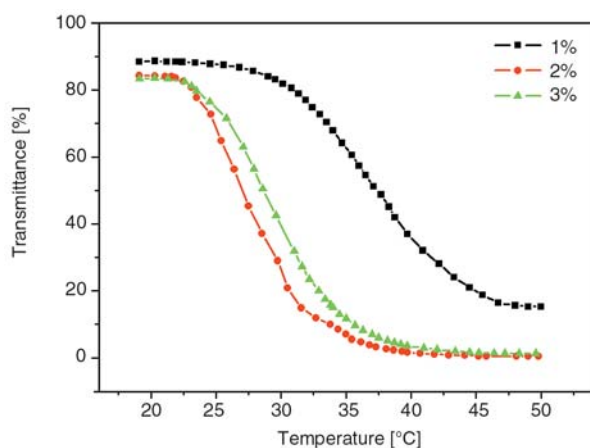

Figure 4. Effect of the copolymer concentration in aqueous solution on LCST Solvent: deionized water; pH = 6.5; wavelength = 500 nm

3.3.2. Effect of the ratio of HPA to AMHS on LCST

The temperature-responsiveness of the title copolymers was confirmed by monitoring transmittance in
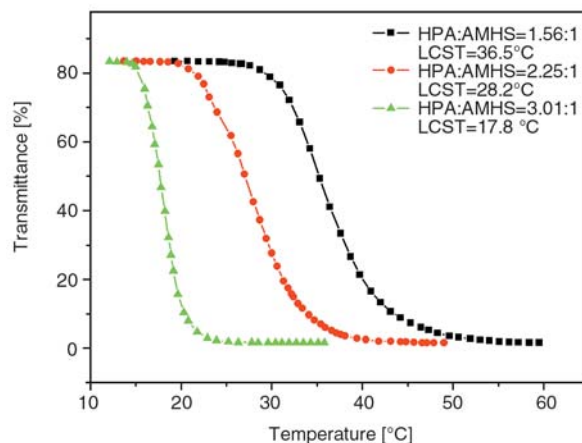

Figure 5. Transmittance as a function of temperature for copolymer in aqueous solution Solvent: deionized water; pH = 6.5; wavelength = 500 nm

3% (wt) solution as a function of temperature. As shown in Figure 5, the LCST of copolymer were 36.5, 28.2 and 17.8°C, respectively, when the molar ratios of HPA to AMHS on polymer chain were fixed at 1.56, 2.25 and 3.01. This result suggested that LCST of copolymer was decreased with increasing content of hydrophoblic HPA units. Compared to AMHS, HPA factually exhibits a slight hydrophobicity to some extent. The similar tendency has been reported that the LCST of *N*-isopropylacrylamides-based copolymer was decreased by the incorporation of more hydrophobic monomer [20]. Additionally, no obvious LCSTs were observed in the copolymer aqueous solution when the ratio of HPA to AMHS was under 1 or above 5 in the copolymerization. The reasons for this may be explained as the excessive hydrophilicity or hydrophobicity in the copolymeric chains. LCST values of the copolymers prepared in this study, especially for PHA2, are very close to the physiological temperature. As a result, these copolymers are suitable to the application in the biomedical fields. In addition, the more sensitive responsiveness was found with increasing the hydrophobic HPA unit content in copolymer chains. The temperature span in the phase transition for PHA2 was about 28°C (from 27 to 55°C), whereas the range during the phase transition for PHA4 reached about 12°C (from 13 to 25°C).

3.3.3. Effect of pH value on LCST

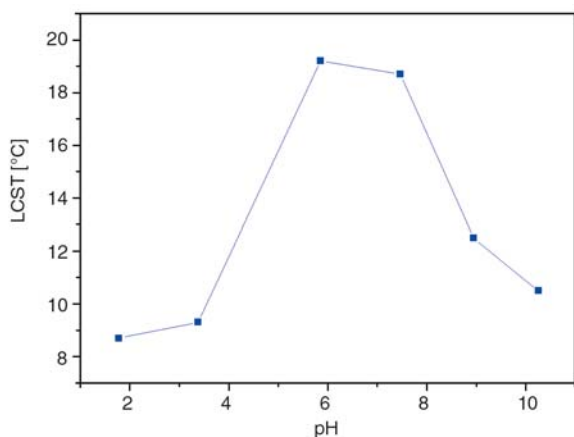Figure 6 demonstrates the effect of pH on LCST of PHA3 copolymer. Herein, the phosphate buffered

Figure 6. Effect of pH in copolymers aqueous solution on LCST Solvent: phosphate buffered saline (PBS); wavelength = 500 nm

saline (PBS) with the same ion strength (I = 0.6) was used as the medium for the different pH. From the figure it is seen that the phase transition behavior is considerably dependent on the pH value in the solution; increasing pH leads to higher LCST value in the range of pH 1.78–5.85. This effect is related to the dissociative behaviors of the aminoethyl hydrochloric salt moiety on AMHS units. The ionization degree of aminoethyl hydrochloric salt was increased with increasing pH value due to its weak-base/strong-acid salt nature. So, the hydrophilicity of copolymer increases with pH value, resulting in a higher LCST value. This result is consistent with the reported phase transition behaviors of poly(N,N-diethylacrylamide-*co*-methacrylic acid) in different pH solution [21]. At too higher pH, however, the LCST sharply decreased with increasing pH value. For instance, when pH values were adjusted to 7.46, 8.94 and 10.25, the LCSTs were 18.7, 12.5 and 10.5°C, respectively.

3.3.4. Effect of the additive salt on LCST of the copolymer

The thermo-sensitiveness of the copolymers is derived from the hydrophilic/hydrophobic interactions related to the copolymer chains and water molecules [22]. The existence of some amino salt groups on the copolymers prepared from HPA and AMHS may likely alter the aforementioned interaction, further inducing a change of LCST value. Some salts increase the LCST of polymers, which is called the 'salting-in' effect; while other salts can decrease the LCST value, which is called 'salting-

out' effect [23]. In order to investigate the effect of some inorganic salts on LCST of the copolymer, two series of potassium salt and metallic nitrate (0.02–0.20 mol/l) were added into the copolymer aqueous solution (3 wt%), and their LCSTs were measured.

Figure 7 has shown the LCST-shifting effect with respect to the concentration of potassium salts. Clearly, the LCST value of copolymer PHA4 changed drastically when potassium salts was charged to copolymer solution. The changing LCST increased with increasing its concentration. For example, when the concentration of KBr was 0.02, 0.05, 0.10, 0.15, and 0.20 mol/l, the LCST of PHA4 changed to 16.4, 15.8, 15.2, 14.9 and 14.4°C from 17.8°C (in deionized water). The result was in a good agreement with the studies on aqueous hydroxypropyl cellulose solution by Oshima and co-workers [24]. In addition, different from the effect of KBr and KCl, LCST of the copolymer PHA4 exhibited an increasing tendency with increasing the concentration of KI. The LCSTs of PHA4 increased to 18.1, 18.0, 18.5, 19.5 and 20.6°C, respectively, as KI concentrations were fixed at 0.02, 0.05, 0.10, 0.15, 0.20 mol/l. It has generally been accepted that the larger anion such as I⁻ served as 'salting-in' effect, while the smaller anion including F⁻, Br⁻ and Cl⁻ functioned as 'salting-out' effect [23]. From the comparative data of three anions, the effectiveness order from 'salting-out' to 'salting-in' in this system is summarized as follows: KCl ≈ KSCN > KBr > KNO$_3$ > KI. The experiment result is consistent with the investigation on the other polymer system [25]. In overall,
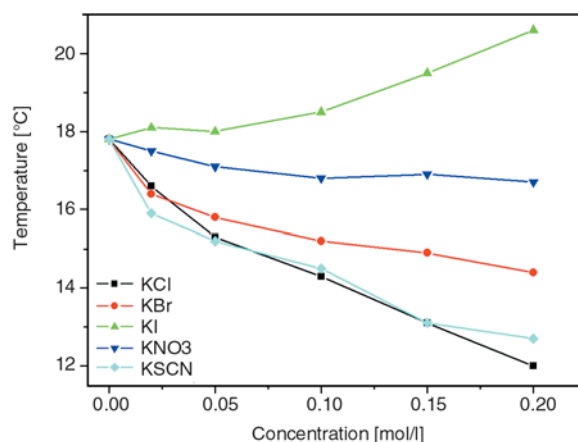

Figure 7. Effect of a series of potassium salts in PHA4 aqueous solution on LCST Solvent: deionized water; wavelength = 500 nm

KI seems to increase H-bonding (hydrophilic inter-action) between water molecules and copolymer chains, leading to an increase in LCST value. On the contrary, KBr and KCl seem to decrease the interaction among water and polymer, resulting in decrease of the LCST.

Figure 8 illustrated the effect of several metallic nitrates on the LCST of copolymers as function of its concentration. The addition of metallic nitrate into the aqueous copolymer solution also induced the alteration of LCST, especially for $NaNO_3$, $Mg(NO_3)_2$ and KNO_3. For instance, when the concentrations of $NaNO_3$ and $Mg(NO_3)_2$ were controlled at 0.20 mol/l, the change of LCST was found to be 4.9°C (12.9–17.8°C) and 2.0°C (15.8–17.8°C), respectively. $Al(NO_3)_3$, however, appears to be a weak LCST-shifter in our system, which is not in accordance with the study on hydroxypropyl cellulose system by Oshima [24]. The reason may likely be ascribed to the fact that the copolymer with amino salts investigated in this paper is different from the nonionic hydroxypropyl cellulose studied by Oshima. Additionally, NO_3^- ions act as LCST-elevating driver. The LCST-elevating potential from NO_3^- ions in $Al(NO_3)_3$, solution overtakes that in $NaNO_3$, $Mg(NO_3)_2$ and KNO_3 solution with the same molar concentration. Concerning the overall effect of nitrates selected, it could be concluded that the order in effectiveness from 'salting-in' to 'salting-out' was $Al(NO_3)_3 > KNO_3 > Mg(NO_3)_2 > NaNO_3$. Therefore, $NaNO_3$ could be used as the efficient LCST-shifter for this copolymer from HPA and AMHS.
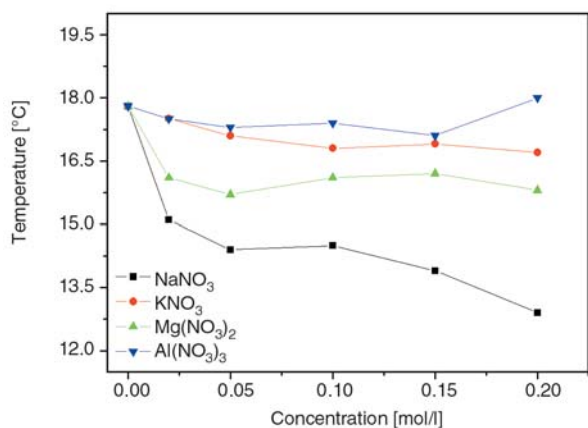

Figure 8. Effect of a series of metallic nitrates in PHA4 aqueous solution on LCST Solvent: deionized water; wavelength = 500 nm

4. Conclusions

In this study, a novel pH-temperature responsive copolymers were prepared by modulating the ratio of HPA to AMHS monomers. The LCSTs of the resulting copolymers rapidly increased as the content of hydrophilic monomer AMHS was increased. Also, the copolymer exhibited a complicated phase transition behavior in the different pH medium, i.e., its LCST first increased and thereafter decreased with an increase in pH value. The investigation on the effect of additive salts suggested that LCST of copolymer shifted either down or up, depending on the different cations and anions, as well as on their concentration. These copolymers seem to be good candidates for being used as controlled-drug release carriers by pH and temperature stimuli.

References

[1] Gil E. S., Hudson M. S.: Stimuli-reponsive polymers and their bioconjugates. Progress in Polymer Science, **29**, 1173–1222 (2004).
DOI: 10.1016/j.progpolymsci.2004.08.003

[2] Zhang J-T., Xue Y-N., Gao F-Z., Huang S-W., Zhou R-X.: Preparation of temperature-sensitive poly(*N*-isopropylacrylamide)/β-cyclodextrin-grafted poly-ethylenimine hydrogels for drug delivery. Journal of Applied Polymer Science, **108**, 3031–3037 (2008).
DOI: 10.1002/app.27931

[3] Kanazawa H., Sunamoto T., Matsushima Y., Kikuchi A., Okano T.: Temperature-responsive chromatographic separation of amino acid phenylthiohydantoins using aqueous media as the mobile phase. Analytical Chemistry, **72**, 5961–5966 (2008).
DOI: 10.1021/ac0004658

[4] Kurisawa M., Yokoyama M., Okano T.: Gene expression control by temperature with thermo-responsive polymeric gene carriers. Journal of Controlled Release, **69**, 127–137 (2000).
DOI: 10.1016/S0168-3659(00)00297-2

[5] Washington R. P., Steinbock O.: Frontal polymerization synthesis of temperature-sensitive hydrogels. Journal of the American Chemical Society, **123**, 7933–7934 (2001).
DOI: 10.1021/ja0161103

[6] Zhang J., Peppas N. A.: Synthesis and characterization of pH- and temperature-sensitive poly(methacrylic acid)/poly(*N*-isopropylacrylamide) interpenetrating polymeric networks. Macromolecules, **33**, 102–107 (2000).
DOI: 10.1021/ma991398q

[7] Li H., Chen J., Lam K. Y.: Multiphysical modeling and meshless simulation of electric- sensitive hydrogels. Journal of Polymer Science Part B: Polymer Physics, **42**, 1514–1531 (2004).
DOI: 10.1002/polb.20025

[8] Chiu H-C., Lin Y-F., Hung S-H.: Equilibrium swelling of copolymerized acrylic acid-methacrylated dextran networks: Effects of pH and neutral salt. Macromolecules, **35**, 5235–5242 (2002).
DOI: 10.1021/ma0122021

[9] Xiao X. C.: Effect of the initiator on thermosensitive rate of poly(*N*-isopropylacrylamide) hydrogels. Express Polymer Letters, **1**, 232–235 (2007).
DOI: 10.3144/expresspolymlett.2007.35

[10] Park J. S., Kataoka K.: Precise control of lower critical solution temperature of thermosensitive poly(2-isopropyl-2-oxazoline) via gradient copolymerization with 2-ethyl-2-oxazoline as a hydrophilic comonomer. Macromolecules, **39**, 6622–6630 (2006).
DOI: 10.1021/ma0605548

[11] Maeda Y.: IR spectroscopic study on the hydration and the phase transition of poly(vinyl methyl ether) in water. Langmuir, **17**, 1737–1742 (2001).
DOI: 10.1021/la001346q

[12] Schild H. G.: Poly(*N*-isopropylacrylamide): Experiment, theory and application. Progress in Polymer Science, **17**, 163–249 (1992).
DOI: 10.1016/0079-6700(92)90023-R

[13] Fundueanu G., Constantin M., Bortolotti F., Cortesi R., Ascenzi P., Menegatti E.: Poly[[(*N*-isopropylacrylamide-*co*-acrylamide-*co*-(hydroxyethylmethacrylate))] thermoresponsive microspheres: An accurate method based on solute exclusion technique to determine the volume phase transition temperature. European Polymer Journal, **43**, 3500–3509 (2007).
DOI: 10.1016/j.eurpolymj.2007.05.026

[14] Lokitz B. S., York A. W., Stempka J. E., Treat N. D., Li Y. T , Jarrett W. L., McCormick C. L.: Aqueous RAFT Synthesis of micelle-forming amphiphilic block copolymers containing *N*-acryloylvaline. Dual mode, temperature/pH responsiveness, and 'locking' of micelle structure through interpolyelectrolyte complexation. Macromolecules, **40**, 6473–6480 (2007).
DOI: 10.1021/ma070921v

[15] Chen J., Sun J., Yang L. M., Zhang Q. F., Zhu H. N., Wu H. F., Hoffman A. S., Kaetsu I.: Preparation and characterization of a novel IPN hydrogel memberane of poly(*N*-isopropylacrylamide)/carboxymethyl chitosan (PNIPAAM/CMCS). Radiation Physics and Chemistry, **76**, 1425–1429 (2007).
DOI: 10.1016/j.radphyschem.2007.02.045

[16] Nitschke M., Götze T., Gramm S., Werner C.: Detachment of human endothelial cell sheets from thermo-responsive poly(NiPAAm-co-DEGMA) carriers. Express Polymer Letters, **1**, 660–666 (2007).
DOI: 10.3144/expresspolymlett.2007.90

[17] Ivanova P., Eliyas A.: Kinetics of the esterification of methacrylic acid with ethylene oxide in the presence of ferric chloride immobilized on polymer support. Applied Catalysis, **53**, 41–52 (1989).
DOI: 10.1016/S0166-9834(00)80008-1

[18] Stempel G. H., Cross R. P., Mariella R. P.: The preparation of acrylyl chloride. Journal of the American Chemical Society, **72**, 2299–2300 (1950).
DOI: 10.1021/ja01161a527

[19] Eggenhuisen T. M., Becer C. R., Fijten M. W. M., Eckardt R., Hoogenboom R., Schubert U. S.: Libraries of statistical hydroxypropyl acrylate containing copolymers with LCST properties prepared by NMP. Macromolecules, **41**, 5132–5140 (2008).
DOI: 10.1021/ma800469p

[20] Feil H., Bae Y. H., Feijen J., Kim S. W.: Effect of comonomer hydrophilicity and ionization on the lower critical solution temperature of *N*-isopropylacrylamide copolymers. Macromolecules, **26**, 2496–2500 (1993).
DOI: 10.1021/ma00062a016

[21] Liu S. X., Liu M. Z.: Synthesis and characterization of temperature- and pH-sensitive poly(*N*, *N*-diethylacrylamide-*co*-methacrylic acid). Journal of Applied Polymer Science, **90**, 3563–3568 (2003).
DOI: 10.1002/app.13034

[22] Schmitz S., Ritter H.: Unusual solubility properties of polymethacrylamides as a result of supramolecular interactions with cyclodextrin. Angewandte Chemie, International Edition, **44**, 5658–5661 (2005).
DOI: 10.1002/anie.200501374

[23] Von Hippel P. H., Schleich T.: Ion effects on the solution structure of biological macromolecules. Accounts of Chemical Research, **2**, 257–265 (1969).
DOI: 10.1021/ar50021a001

[24] Nishio Y., Chiba R., Miyashita Y., Oshima K., Miyajama T., Kimura N., Suzuki H.: Salt addition effects on mesophase structure and optical properties of aqueous hydroxypropyl cellulose solutions. Polymer Journal, **34**, 149–157 (2002).
DOI: 10.1295/polymj.34.149

[25] Lee S. B., Song S-C., Jin J-I., Sohn Y. S.: A new class of biodegradable thermosensitive polymers. 2. Hydrolytic properties and salt effect on the lower critical solution temperature of poly(organophosphazenes) with methoxypoly(ethylene glycol) and amino acid esters as side groups. Macromolecules, **32**, 7820–7827 (1999).
DOI: 10.1021/ma990645n

Effect of polymer structure and additives on silane grafting of polyethylene

J. Morshedian[1], P. Mohammad Hoseinpour[1], H. Azizi[1], R. Parvizzad[2]*

[1]Iran Polymer and Petrochemical Institute (IPPI), P.O. Box: 14965/115, Tehran, Iran
[2]Research and Development Department, Tabriz Petrochemical Company, Tabriz, Iran

Abstract. Silane method is a preferred method in crosslinking polyethylene to modify its properties. Here, the silane grafting reactions of low density (LDPE), linear low density (LLDPE) and high density polyethylene (HDPE) were compared, all with a fixed amount of silane (vinyltrimethoxysilane) and peroxide (dicumylperoxide). Processing for silane grafting was carried out in an internal mixer, and FTIR spectra were used for comparing the silane grafting efficiencies. The effect of polymer physical form and pre-mixing the components was also determined. Molecular structure parameters were analyzed to investigate their effect on silane grafting efficiency. In case of LDPE and LLDPE, the probable interfering effect of two types of antioxidants on silane grafting reactions was studied. Ethylene propylene diene monomer (EPDM) was added to LDPE to evaluate its effect on silane grafting efficiency. Amongst different grades of polyethylene, LLDPE had a better efficiency in silane grafting. Branchings, PDI, M_w, and MFI are all determining factors and should be considered in comparing the silane grafting efficiency between different grades of polyethylene. In case of incorporating antioxidant, different results were observed when the polymer under study was different. EPDM as an additive would enhance silane grafting efficiency.

Keywords: material testing, branching number, polydispersity index, polyethylene, silane grafting

1. Introduction

Un-crosslinked polyethylene has the melting point of 100–130°C, however, after crosslinking no flow would be noticed even at 150°C [1, 2], where elastic behaviour prevails. In addition to the advantages associated with crosslinked polyethylene, it is also capable of absorbing high loadings of fillers compared to un-crosslinked polyethylene which becomes brittle on incorporating fillers. By crosslinking polyethylene, some of its important properties (e.g. creep and wear resistance, long term service temperature, impact strength) would also be drastically improved [3–5]; this makes polyethylene a good choice for applications such as hot water pipe, heat shrinkable products, steam resistant food packaging, and foams for thermal insulation.

There are some methods to crosslink polyethylene, among which silane method is a common and beneficial approach to crosslink polyethylene which per se has no functional group or cure site to be crosslinked in a way similar to some other thermoset resins. This method can be done in two ways, either by grafting unsaturated hydrolysable alkoxysilanes onto or copolymerizing them into polyethylene chains [6, 7], followed by processing and shaping the polymer into final product and then moisture curing it in the presence of catalyst. In silane crosslinking, siloxane bridges link polyethylene chains together. Recently, it is also possible to

crosslink the silane-polyethylene copolymer at ambient temperature in the absence of high moisture content, taking the advantage of some special catalysts [8–10]. Easy processing, low cost and capital investments, and favourable properties of processed materials are the advantages of silane method [11]. Further studies on this subject would be found in literature for interested reader [12–16]. Considering the role of antioxidants in preventing or retarding oxidation degradation, it is important to study the proper type of antioxidant in crosslinked polyethylene which has no or the least interference with silane grafting reactions [17–20]. Frequently applied antioxidants for crosslinked polyethylene are mentioned in plastics additives handbook [21], among which the influence of two common types of antioxidants are studied here.

EPDM (ethylene propylene diene monomer) as additive in polyethylene would contribute flexibility to polyethylene, besides improving some properties such as elongation at break and impact resistance [22]. In silane method of crosslinking, due to the reduction of crystallinity in polymer matrix as a result of incorporating EPDM, water diffusion (in moisture curing step) would be enhanced and so does the crosslinking rate. For these reasons, the effect of adding EPDM on grafting efficiency of polyethylene is studied. The result of this study could be generalized to material parameters affecting extent of functionalization or grafting of low molecular weight species to polyethylene by radical reaction in melt mixing.

2. Experimental

2.1. Materials

2.1.1. Polymers

The information of low density polyethylene (LDPE), linear low density polyethylene (LLDPE) and high density polyethylene (HDPE) used in this study can be found in Tables 1 and 2. Ethylene propylene diene monomer (EPDM) with the trade name Vistalon 7500 (supplied by ExxonMobil Chemical Company (USA)), was a terpolymer containing ethylene (55.5 wt%), propylene and ethylidene norbornene (5.7 wt%). All the polymers were received as granules except the EPDM which was in chips form.

Table 1. Suppliers' information for polyethylenes used in this study

Polyethylene	Trade name	Manufacture
LDPE	LH0075	Bandar Imam Petrochemicals Co. (Iran)
LLDPE	BPD3052	INEOS Group Limited (United Kingdom)
HDPE	Ex3	Arak Petrochemicals Co. (Iran)

Table 2. Properties of polyethylenes used in this study

	LDPE	LLDPE	HDPE
MFI (190°C, 2.16 kg) [g/10 min]	0.70	3.50	0.40
$M_n \cdot 10^{-3}$	17.6	17.1	13.9
$M_w \cdot 10^{-4}$	12.7	6.402	13.6
Polydispersity Index (PDI)	7.234	3.736	9.770

2.1.2. Silane

As the most common silane used in the manufacture of silane crosslinkable polyethylene is vinyltrimethoxysilane [23], here vinyltrimethoxysilane was used as the silane, which was in liquid form and with boiling temperature of 123°C, and supplied by Evonik Industries, Germany, under the trade name of Dynasilan VTMO.

2.1.3. Peroxide

Free radicals are needed to initiate silane grafting by abstracting hydrogen atoms from the macromolecules (said alkylradicals); these free radicals are generated from thermally degradable organic peroxides [24], with the most preferred one being dicumylperoxide. It is also possible for unsaturation on silane to be attacked by peroxide followed by reaction with the polyethylene chain [25]. For the current study, the peroxide was dicumylperoxide with 98% purity and melting point of 49°C, supplied by Ashland Inc. (USA), under the trade name of Di-cup 40C.

2.1.4. Antioxidant

The antioxidants used in this study are listed in Table 3, all provided by Ciba Specialty Chemicals, Switzerland.

Table 3. Information of antioxidants used in this study

Trade name	Chemical name	Designation in this study
Irganox® 1010	pentaerythritol tetrakis(3-(3,5-di-tert-butyl-4-hydroxyphenyl)propionate)	AO-1
Irgastab® Cable KV10	4,6-bis (octylthiomethyl)-o-cresol	AO-2

2.1.5. Other material(s)

Acetone (99.5% purity) was supplied by Merck Ltd, Germany, and used as received.

2.2. Equipments

The Melt Flow Index (MFI) of pure polyethylenes was determined through a model 5MPCA MFI equipment (Ray-Ran Co. England) according to ASTM D1238, under 2.16 kg load, at 190°C.

In case of using polyethylenes in powder form the granules were powdered by Pulman Powder Mill, Germany. Pre-mixing was done using a turbo-mixer (TM-2002 Model) manufactured by Borhan Pooya Chemi Trading Ltd., Iran.

The grafting process was carried out in an internal mixer (Rheomix Haake, SYS 90, NJ, USA) with a Banbury-type rotor. Fourier transform infrared (FTIR) spectroscopy was carried out by FTIR, Bruker IFS 48 on thin films for evaluating the extent of grafting.

Oxidative induction time (OIT) tests were fulfilled for 3.50 milligram of polymer at 200°C in Differential Scanning Calorimeter, Stanton Redcraft STA-780, according to ASTM D3895.

The molecular weight, polydispersity indices and branchings were determined using Size Exclusion Chromatography (SEC) equipped with a refractive index (RI) detector, an on-line viscometer and a Multi Angle Light Scattering (MALLS) detector. The solvent was 1,2,4-trichlorobenzene (TCB) and the samples were dissolved at 123°C.

2.3. Procedure

2.3.1. Processing

All the experiments were carried out using 0.04 weight part peroxide per hundred weight part of polyethylene [phr] and 4 phr silane. A solution of silane and peroxide in predetermined amounts was prepared for each batch, and polyethylene (in granular or powder form) mixed with this solution using turbo-mixer at 1500 rpm for one hour. In case

of incorporating antioxidant, an amount of 0.1 phr antioxidant was added to aforementioned solution prior to mixing with polymer in turbo-mixer. Silane grafting of polyethylene was carried out in the melt in a batch operation using internal mixer. The rotor speed, processing time, and the temperature were fixed at 60 rpm, 15 minutes, and 190°C, respectively. For assessing neat polymers (no other reactant) they were processed directly in internal mixer. In incorporating EPDM, it was used as received (in form of chips), and hand-mixed with polyethylene prior to pre-mixing.

2.3.2. Fourier Transform Infrared (FTIR) sample preparation

Thin films for spectroscopy analysis were prepared by a hot press at 170°C, under 30 MPa for 20 seconds; samples (or granules) to be pressed were equal weighted and thus the obtained film thicknesses were similar (200 micrometer). After preparation of thin films, each film was immersed in acetone for 3 hours, followed by washing with pure acetone and drying for 1 minute under hot air flow, to get sure about leaching all the remnant (un-reacted) silane out. It should be noted that by hot pressing the films, the un-reacted silane would already evaporated as its boiling point is 123°C [26].

3. Results and discussion

3.1. Silane grafting determination

3.1.1. Torque monitoring

Here, the aim is to characterize the influence of molecular structure and additives (EPDM and antioxidants), on the extent of silane grafting in polyethylene. Determination of silane grafting efficiency is important due to its inevitable effect on crosslinking which follows after. The later is not the concern of current study.

During the processing in internal mixer, the first increase in torque observed in Figure 1 is due to
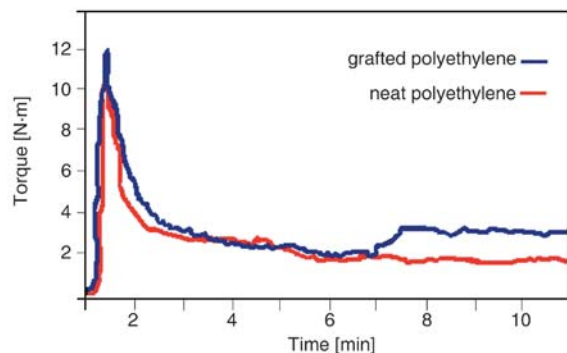
Figure 1. Typical plots of torque vs. time, observed for silane grafted LDPE and the neat one (LDPE without any silane or peroxide)

adding material(s). The torque decreases as the polymer starts plasticating and melting. The following increase in case of silane-containing polyethylene is an indication of starting grafting reactions and is occurred because of the increase in melt viscosity and continues to a plateau. The final torque of silane-grafted polyethylene is higher than that of the neat one (as shown in Figure 1). If the mixing goes further in time, the torque would further increase in result of degradation crosslinking or silane crosslinking in presence of ambient water vapour.

3.1.2. FTIR characterization

In studying the FTIR spectra, the transmittance peaks of interest are listed in Table 4. Obviously, the neat polymer has no peak at 1092 cm^{-1}. The 1092 cm^{-1} is used as an indication of silane grafting extension in samples of this study which typically has the strongest absorbance [17, 27] compared to 799 and 1192 cm^{-1}. The peak at 1080 cm^{-1} is the result of crosslinking, which could occur to some extent even during grafting process. In such cases,

the Si–OCH$_3$ is apt to be masked by strong Si–O–Si absorption [27]. Vinyl and vinylidene groups are considered as the unsaturations in polyethylene and used as one of their microstructure parameters when studying the silane grafting efficiency.

As the film thicknesses (prepared for FTIR study) were almost the same (and if not, hot pressing was repeated to reach the film with desired thickness) and polyethylene shows no transmittance peak at wavenumber of 1092 cm^{-1}, it is possible to consider the height of transmittance peak in this wavenumber as the grafting efficiency and use the corresponding value to compare the silane grafting efficiency in different polyethylenes, although this would be only a realtive comparison and not a quantitative one [26].

3.2. Effect of pre-mixing and polymer physical form

Prior to processing in internal mixer, pre-mixing of the silane compound and peroxide with polymers plays an important role in final results, since silane is hardly adsorbed by polyethylene if pre-mixing is not carried out. To demonstrate this dependency, first the LDPE was added to internal mixer (in form of granules) and at the pre-fixed temperature of 115°C. After melting (observed through the first torque reduction), silane (4 phr) was added to it by using a glass syringe. As the boiling temperature of silane is 123°C, it is to be added at such a temperature (115°C). Then, the temperature of internal mixer was set to 190°C. By reaching this temperature, peroxide (0.04 phr) was added to internal mixer (approximately 18 minutes from the first adding polyethylene to mixer) and the processing was continued till a rise in torque observed (nearly

Table 4. Transmittance FTIR peaks for specified groups

Group	Structure	Wavenumber [cm^{-1}]	Reference
Trimethoxysilane	Si—OCH$_3$	799, 1092, 1192	[7, 18]
Siloxane	Si—O—Si	1080	[18, 19]
Carbonyl	C═O	1720	[29]
Vinyl	⎯CH$_2$ · H · C═C · H · H	909, 990	[28, 30, 31]
Vinylidene	⎯CH$_2$ · H · C═C · ⎯CH$_2$ · H	888	[28, 30]

20 minutes after addition of peroxide). It is noteworthy to say that since peroxide would initiate polyethylene crosslinking reactions even at such a low temperature of 120°C, where silane has still no noticeable activity in such a temperature, in case of adding peroxide together with silane at 115°C, there would be a strong probability to have undesired crosslinking reactions by consuming peroxide (through formation of C–C crosslinks) and hence no further silane grafting at higher temperatures. Thus, by designing the procedures in such a way that the silane was added first (at 115°C), followed by the addition of peroxide at 190°C, we avoided the undesired possible peroxide initiated crosslinking reactions (C–C crosslinks). Besides, by choosing such a low amount of peroxide (0.04 phr) and thus making the ratio of silane to peroxide to be almost 100, and considering that in the silane : peroxide ratios of more than 50 the risk of crosslinking reactions initiated by peroxide reaches almost zero, we avoided the undesired reactions. For confirming this hypothesis, we further performed the gel content tests on some of the final resultant specimens, right after the processing. By immersion of the specimens in boiling xylene, we noticed almost no left polyethylene (as the gel content) after 24 hours. That proved us the reliability of our processing method and reactants ratios.

Once again, the LDPE granules with specified amounts of silane and peroxide was poured in turbo-mixer and mixed for about one hour at 1500 rpm without any heating. As presented in Table 5, in case of the non-premixed sample there is no observed peak at 1092 cm^{-1} and instead, there is a peak at 1080 cm^{-1}. This peak is a result of forming Si–O–Si bands, i.e. occurrence of silane crosslinking. As it consumes more time to perform the whole process with incorporating silane and peroxide separately into internal mixer (when no pre-mixing was done before), the mixture passed a longer time under processing before reaching the increase in torque. At such a high temperature (190°C) and with presence of ambient water vapour, crosslinking reactions would commonly

occur, and this is not desired. Based upon this observation and since the normalized peak at 1080 cm^{-1} is still short, indicating the low efficiency in silane grafting prior to crosslinking reactions, all other samples in following experiments went under an hour pre-mixing (in turbo-mixer at 1500 rpm) prior to their processing.

Now this should be noted that although the procedures were designed to include the pre-mixing step (and not adding silane and peroxide in two steps, as previously mentioned), still both the pre-mixing effect and the silane : peroxide ratio helps avoiding the formation of C–C crosslinks, as proved by gel content tests.

To study the importance of polymer physical form (i.e. granular or powder form), LDPE was premixed with specified amount of silane-peroxide solution in powder form. After this pre-mixing and processing, the resultant FTIR spectra have been shown in Figure 2, and the corresponding peak height at 1092 cm^{-1} are 47 and 63 millimetre for granular LDPE and the powder one, respectively. Thus, it can be inferred that physical form of polymer is of a great importance in increasing the silane grafting extent; in powder form there would be more surface area of polymer to adsorb silane-peroxide solution. To reach this better efficiency, all the polymers were processed at powder form rather
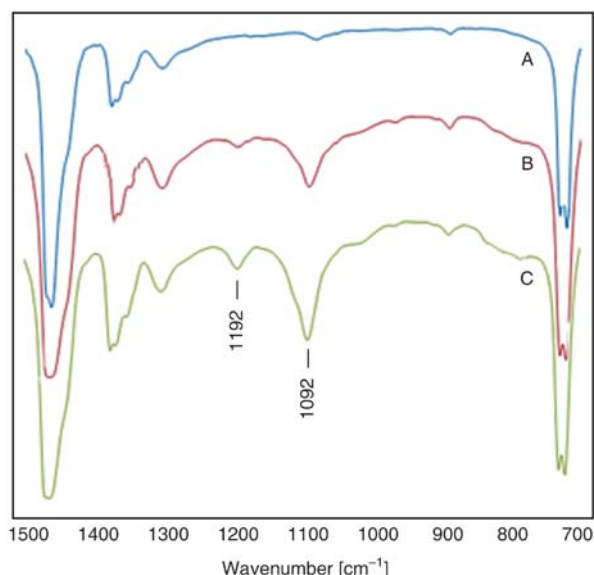

Figure 2. FTIR spectra for LDPE A) neat polymer, B) granular silane grafted, C) powder grafted. Both A) and B) are grafted with 4 and 0.04 phr silane and peroxide, respectively, and the reaction mixture was pre-mixed in turbo-mixer for an hour prior to processing.

Table 5. Comparison of silane grafting in premixed and non-premixed granular LDPE

		Non-premixed granular LDPE	Pre-mixed granular LDPE
Peak height [mm] at	1092 cm^{-1}	0	47
	1080 cm^{-1}	21	0

than granular form in all other experiments of the current study.

3.3. Effect of polymer type

The extent of silane grafting for similarly grafted LDPE, LLDPE, and HDPE have been determined via their corresponding FTIR spectra and the measured values are presented in Table 6.

Referring to Table 6, the higher peak height at 1092 cm^{-1} for LLDPE with respect to that of LDPE and HDPE indicates that LLDPE is more apt to silane grafting reactions compared to LDPE. This is also true for LDPE compared to HDPE. In initiating the silane grafting reaction, peroxide decomposition species would participate in different reactions [2]; they would combine with each other to form unsaturated species; inducing to β-scissioning in polymer chain and thus leading to chain extension; and finally they would react with the vinyl unsaturation of silane for grafting the molecule onto the polyethylene. Among all the aforementioned reactions, only the last one is desired and the other two would result in molecular structure changes and consequently lead to differences in crosslinking performance [26]. Different types of polyethylene have different tendency and probability for these side reactions and thus different extent of silane grafting would be obtained in fixed amounts of reactants for each type of polyethylene. However, the more efficient grafting in LLDPE rather than LDPE and HDPE, would be also due to existence of tertiary carbons in LLDPE which are

Table 6. Comparison of silane grafting efficiency in LDPE, LLDPE and HDPE

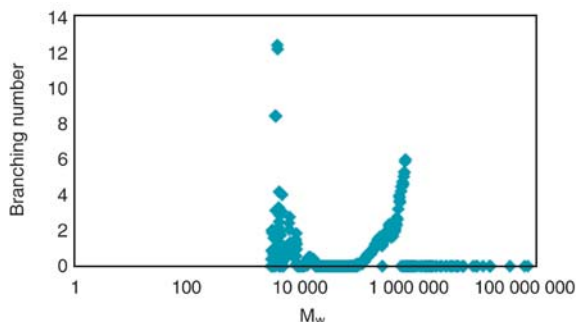| Polymer	LDPE	LLDPE	HDPE
Peak height [mm] at 1092 cm^{-1}	63	70	25

Figure 3. Branching number of LLDPE versus its molecular weight, determined by SEC
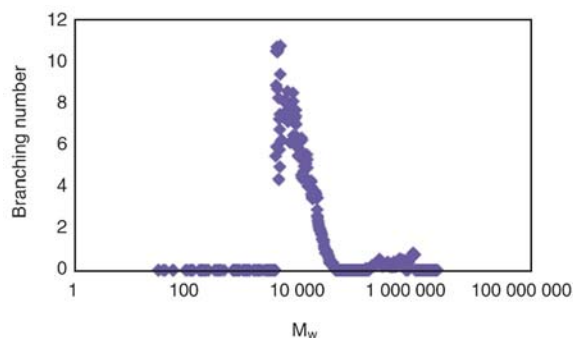

Figure 4. Branching number of LDPE versus its molecular weight, determined by SEC

more apt to react with free radicals initiating grafting reactions [26], since the associated hydrogens are relatively easy to be abstracted during silane grafting reactions. The less tendency to silane grafting in HDPE can be related to the shortage of tertiary carbons: HDPE has ignorable branches. Branching status of LLDPE and LDPE are shown in Figures 3 and 4. As it can be observed, branchings have been spread within all ranges of molecular weight in LLDPE, but in case of LDPE it is only in low molecular weight range, although both have nearly same branching numbers. Thus, the branching distribution (with respect to molecular weight) affect the silane grafting in such a way that wider distribution (bi-modal) (as in case of LLDPE) results in higher grafting, and narrower one contributes to less tendency for silane grafting.

However, there are other factors that would possibly take part in determination of ultimate silane grafting efficiency; it is obvious that the vinyl group in silane is the active site for initiation of grafting on polyethylene in presence of peroxide. Thus, presence of unsaturation in polyethylene itself would positively affect silane grafting initiation. According to Table 4, the corresponding peaks for unsaturation can be detected via FTIR spectra. Only vinyl bonds were investigated here, as they are more active to take part in silane grafting. The vinyl group absorbs at both 909 and 990 cm^{-1}, but only the peak at 909 cm^{-1} is used here, due to its reported stronger absorption. Considering the magnified FTIR spectra for neat polymers (see Figure 5), LLDPE and HDPE has a peak height 0.055 and 0.052 millimetre, respectively, and the corresponding peak height for LDPE is negligible. Thus, higher relative content of vinyl unsaturation in LLDPE would positively affect its
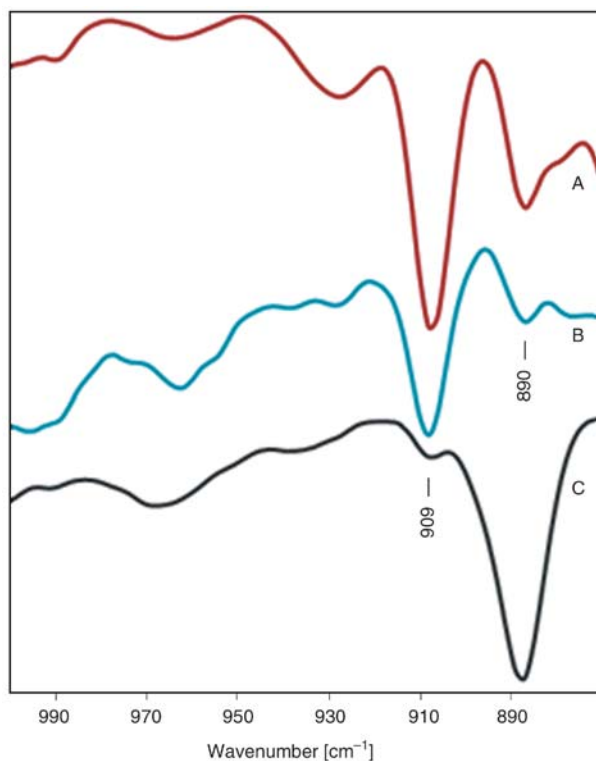
Figure 5. Magnified FTIR spectra for neat polymers, A) LLDPE, B) HDPE, C) LDPE. The transmition range is magnified to show the range of 0.945 to 0.97, in order to highlight the vinyl unsaturation peaks on polyethylenes.

more efficient performance in silane grafting, while due to the negative cumulative effects of other parameters (discussed above or in the following lines) in HDPE, its vinyl unsaturation would contribute no significant positive effect on its silane grafting.

It should be noted that although a peak at 888 cm⁻¹ can be observed (for LDPE) in Figure 5, it can not be referred to vinylidene unsaturation, as it is always overlapped by absorption at 889 to 903 cm⁻¹ from vibrations of terminal methyl groups on alkyl groups longer than ethyl [32].

Furthermore, as it can be seen from Table 2, these polymers have different polydispersity index values and molecular weights. LLDPE has the lowest PDI, followed by LDPE and HDPE, which means that lower PDI provides more tendency for occurrence of silane grafting. Meanwhile, the higher weight average molecular weight for HDPE and the lower weight average molecular weight for LLDPE would contribute to their level of tendency for grafting reaction; i.e., for LLDPE with low weight average molecular weight, there is more accessibility of polymer backbone for silane and the peroxide

decomposition species to start the grafting reactions, while HDPE with higher molecular weight provides less accessibility and LDPE lies between these two. No direct relation can be deduced between number average molecular weights (M_n) and silane grafting efficiency of these polyethylenes.

Moreover, different MFI values should be also taken into account when comparing these types of polyethylene. LLDPE has the highest MFI followed by LDPE and HDPE. This shows that higher MFI would result in more tendency for silane grafting, considering the higher grafting efficiency in LLDPE.

3.4. Effect of additives

3.4.1. Antioxidants

Antioxidants are normally used to achieve thermo-oxidative stabilization. During the processing in presence of antioxidants, some part of peroxide could be consumed in a 'non-useful' reaction, which means that this portion has to be compensated for with additional peroxide and if not, there would be lesser silane grafting efficiency. The grafting process limits the choice of antioxidants since many of them are effective radical scavengers and can inhibit the grafting reaction [12]. Here the effect of two types of antioxidants on silane grafting reactions of LDPE is studied. In each case, the antioxidant was added to the silane-peroxide solution and premixed with polyethylene in turbo-mixer prior to mixing in internal mixer. Table 7 presents the corresponding peak heights. The thermo-oxidative products has the characteristic peaks between 1650 and 1800 cm⁻¹; here the transmittance peak at 1720 cm⁻¹ is considered as the indication of thermo-degradation (designation of

Table.7. Comparison between the silane grafting efficiency and thermal degradation in LDPE for different incorporated antioxidants. All the samples contained 4 phr silane, 0.04 phr peroxide, 0.1 phr antioxidant and premixed in turbo-mixer for one hour, followed by processing in internal mixer for 15 min at 190°C.

		Peak height [mm] at	
		1720 cm⁻¹	1092 cm⁻¹
Grafted LDPE with	AO-1	8	15
	AO-2	4	11
	no antioxidant	14	63

C=O groups), in which, the neat (un-processed) sample shows no peak while the processed neat one shows a strong peak. Thus the height of this peak is a designation of the extent of degradation (although only comparatively).

Here, it should be noted that except LLDPE (as indicated by its supplier), the other two polyethylenes have some amount of antioxidant but determination and evaluation of this amount and/or type is not of this article's concern, as we aimed to study the effect of antioxidants on silane grafting of as received polyethylenes, that is, the form they are already available in market.

Referring to Table 7, it would be possible to assess the effectiveness of antioxidants: shorter the peak height at 1720 cm^{-1} and higher the peak height at 1092 cm^{-1} declares the more effectiveness of antioxidant. In both cases, besides reacting with existing peroxide decomposed species, the antioxidant would also react with the polyethylene alkyl radical which is formed during processing. This may inhibit the grafting reactions. Comparing the peak heights for samples containing antioxidant with the one contains no kind of antioxidant declares this phenomenon.

Incorporation of AO-2 resulted in the least thermal degradation, with respect to AO-1. However, regarding the non-considerable extent of silane grafting, this would be of no advantage to incorporate AO-2 in LDPE in grafting process in aforementioned amounts of silane and peroxide.

The previous experiment was carried out for LLDPE in the same amounts of reactants and conditions. The results obtained from the corresponding FTIR spectra are presented in Table 8.

In case of LLDPE the best antioxidant regarding the least thermal degradation, is AO-2 (as in the case of LDPE), however, in contrary to LDPE, the silane grafting efficiency is considerably higher; it should be noted that although the polyethylenes that contain no antioxidant show less difference in grafting efficiency (peak height of 63 mm in case of LDPE and peak height of 70 mm in case of LLDPE), the grafting efficiency when adding AO-2, is considerably different for the two polyethylenes (peak height of 11 mm in case of LDPE and peak height of 32 mm in case of LLDPE). This shows that while exhibiting frustrating effects, even a same antioxidant would differently affect the silane grafting efficiency, when used in different polymers. Thus, selecting the proper antioxidant for silane grafting of a polyethylene, would not dictate its properness for silane grafting of another polymer.

In a later study it was observed that with employing much higher amounts of silane and peroxide (e.g. up to 6 phr silane and 0.4 phr peroxide) silane grafting would occur in presence of this antioxidant. Based upon OIT tests, maximum 0.1 phr antioxidant would be necessary for preventing the product from degradation (see Figure 6), which imparts 32.92 minute before degradation occurs at 200°C (when the amount of antioxidant chosed 0.05 and 0.75 phr, the induction time became 19.83 and 23.75 minutes, respectively). Thus, a possible practical method to have a desirable grafting extent besides the least thermal degradation would be to incorporate a part of this predetermined amount within the process and let the left amount incorporated in the catalyst masterbatch (to be used during crosslinking process). This has been done before in case of other additives (such as carbon black) which would interfere with the silane grafting reactions [6]. An alternative choice is making use of higher amounts of peroxide which has disadvan-
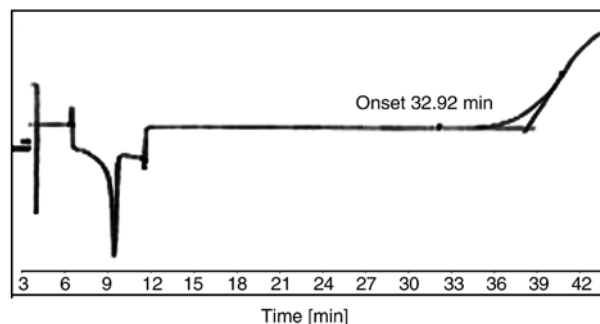
Table 8. Comparison between the silane grafting efficiency and thermal degradation in LLDPE for different incorporated antioxidants. All the samples contained 4 phr silane, 0.04 phr peroxide, 0.1 phr antioxidant and premixed in turbo-mixer for one hour, followed by processing in internal mixer for 15 min at 190°C.

		Peak height [mm] at	
		1720 cm^{-1}	1092 cm^{-1}
Grafted LLDPE with	AO-1	14	31
	AO-2	5	32
	no antioxidant	18	70

Figure 6. OIT for neat LLDPE containing 0.1 phr of AO-1 (3.5 milligram of sample in aluminium pan under 200°C)

tage of some scorch occurring during the grafting stage resulting in formation of gelled spots and a rough surface on the product.

3.4.2. Polymeric additive

The influence of EPDM as polymeric additive was investigated on silane grafting efficiency of LDPE. The experiment was carried out with a fixed amount of EPDM (2 phr); both polymers were hand mixed in powder form and after pre-mixing with reactants, processed similarly as in aforementioned experiments. According to FTIR analysis, the resultant grafting efficiency (peak height at 1092 cm⁻¹) is 78 mm in case of adding EPDM, which is higher compared to the grafting efficiency of the sample containing no EPDM (in that case the grafting efficiency was 63). This could be due to the unsaturation in diene monomer exists in EPDM, which creates some additional reactive sites for silane grafting to occur (grafting may also occur by the abstraction of secondary hydrogen from a polyethylene sequence of EPDM [33, 34]). A schematic of probable silane grafting on unsaturated bond in EPDM is demonstrated in Figure 7.
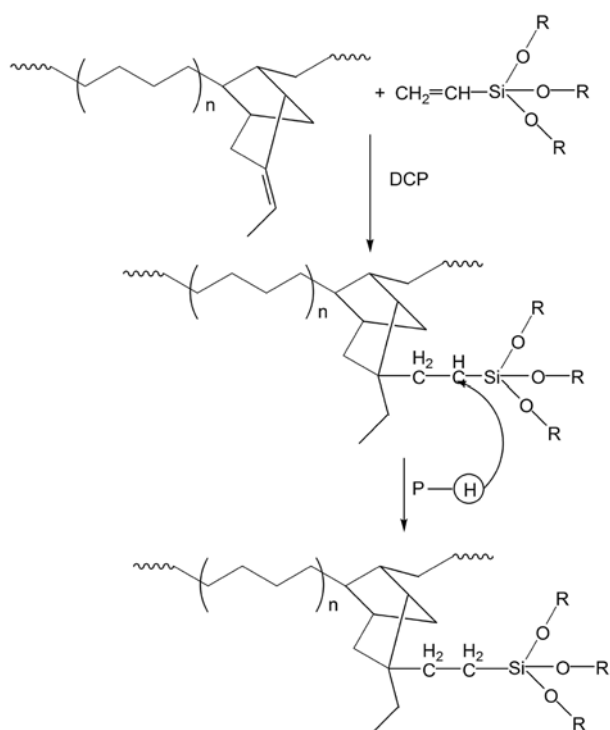
Figure 7. Schematic of silane grafting on EPDM [34]

4. Conclusions

In this study it was aimed to characterize the influence of molecular structure, antioxidants type, and EPDM (as additive), on the extent of silane grafting in polyethylene (LDPE, LLDPE and HDPE), in an internal mixer. Grafting reactions can be well monitored through increase in torque and relatively compared by height of FTIR absorption peaks at 1092 cm⁻¹.

It is concluded that, pre-mixing the mixture prior to processing in a turbo-mixer would result in a better efficiency in grafting, and reducing the probability of premature silane crosslinking (as more time would be required in case of not pre-mixing the reactants, which in turn provides the possibility of parallel crosslinking reactions in presence of ambient moisture) during silane grafting reactions. Furthermore, the physical form of polyethylene plays a critical role in this efficiency, as the powder form results in better efficiency with regard to granules.

Amongst LDPE, LLDPE and HDPE, LLDPE has the highest grafting efficiency followed by LDPE and finally, HDPE. Higher content of tertiary carbon would be the main reason for higher grafting efficiency in LLDPE, however, other factors such as higher branching number and its broader distribution mode (versus molecular weight), higher unsaturation content in polymer backbone, lower PDI, lower weight average molecular weight, and higher MFI, all positively affect silane grafting efficiency in polyethylene. No direct relation can be deduced between number average molecular weights (M_n) and silane grafting efficiency of the polyethylenes under study.

In case of adding antioxidant in LDPE or LLDPE, each of them frustrates the grafting reactions on polyethylene; however, their relative effect on silane grafting was different. That is, although antioxidants reduce the occurrence of the silane grafting reactions, an antioxidant would have less or more effect on the silane grafting efficiency or thermo-degradation of different types of polyethylene.

Considering that the 0.1 phr antioxidant (used in this study) would be necessary for preventing the product from degradation, a possible practical method to have a desirable grafting extent (in both

LDPE and LLDPE) besides the least thermal degradation would be the incorporation of a part of this predetermined amount within the process and have the left amount to be mixed in the catalyst masterbatch (to be used during crosslinking process). Another method is increasing the amounts of peroxide, which makes the possibility of some scorch occurring during the grafting stage which in turn results in the formation of gelled spots and a rough surface on the product.

In case of adding EPDM to LDPE, the resultant silane grafting efficiency is higher compared to the grafting efficiency of the sample which contains no EPDM.

References

[1] Peacock A. J.: Handbook of polyethylene, structures, properties, and applications. Marcel Dekker, New York (2000).

[2] Narkis M., Tzur A., Vaxman A., Fritz H. G.: Some properties of silane-grafted moisture-crosslinked polyethylene. Polymer Engineering and Science, **25**, 857–862 (1985).
DOI: 10.1002/pen.760251311

[3] Zhu Y., Yoon H. G., Suh K. S.: Electrical properties of silane crosslinked polyethylene in comparison with DCP crosslinked polyethylene. IEEE Transactions on Dielectrics and Electrical Insulation, **6**, 164–168 (1999).
DOI: 10.1109/94.765906

[4] Shieh Y-T., Liu C-M.: Silane grafting reactions of LDPE, HDPE and LLDPE. Journal of Applied Polymer Science, **74**, 3404–3411 (1999).
DOI: 10.1002/(SICI)1097-4628(19991227)74:14<3404:: AID-APP14>3.0.CO;2-S

[5] Gale G. M.: Silane compounds in hot-water pipe and cable technology. Applied Organometallic Chemistry, **2**, 17–31 (1988).
DOI: 10.1002/aoc.590020104

[6] Mehrabzade M., Morshedian J., Barzin J.: Preparation of silane grafting and crosslinking of polyethylene: Studies of the factors affecting the grafting and crosslinking. Iranian Journal of Polymer Science and Technology, **1**, 3–10 (1998).

[7] Hjertberg T., Palmlof M., Sultan B. A.: Chemical reactions in crosslinking of copolymers of ethylene and vinyltrimethoxy silane. Journal of Applied Polymer Science, **42**, 1185–1192 (1991).
DOI: 10.1002/app.1991.070420503

[8] Dammert R., Gustafsson B., Sultan B-Å. K.: Polyethylene compatible sulphonic acids as silane crosslinking catalysts. U.S. Patent 6005055, USA (1999).

[9] Blank W. J., Hessel E. T., Abramshe R. A.: Alkylaryl and arylalkyl monosulfonic acid catalysts for crosslinking polyethylene. U.S. Patent 6441097, USA (2002).

[10] Irestahl E., Lindahl S.: Cross-linking studies of PE-VTMS/Visico, effects of TiO₂ addition on catalyst performance, kinetics of the cross-linking reaction. Linköping University, Department of Physics, Chemistry and Biology (2008).

[11] Barzin J., Azizi H., Morshedian J.: Preparation of silane-grafted and moisture cross-linked low density polyethylene: Part I: Factors affecting performance of grafting and cross-linking. Polymer- Plastics Technology and Engineering, **45**, 979–983 (2006).
DOI: 10.1080/03602550600718209

[12] Sultan B. A., Palmlof M.: Advances in crosslinking technology. Plastics, Rubber and Composites, Processing and Applications, **21**, 65–73 (1994).

[13] Kuan H-C., Kuan J-F., Ma C-C., Huang J-M.: Thermal and mechanical properties of silane-grafted water crosslinked polyethylene. Journal of Applied Polymer Science, **96**, 2383–2391 (2005).
DOI: 10.1002/app.21694

[14] Azizi H., Barzin J., Morshedian J.: Silane crosslinking of polyethylene: The effects of EVA, ATH and Sb₂O₃ on properties of the production in continuous grafting of LDPE. Express Polymer Letters, **1**, 378–384 (2007).
DOI: 10.3144/expresspolymlett.2007.53

[15] Venkatraman S., Kleiner L.: Properties of three types of crosslinked polyethylene. Advances in Polymer Technology, **9**, 265–270 (1989).
DOI: 10.1002/adv.1989.060090308

[16] Shieh Y-T., Hsiao K-I.: Thermal properties of silane-grafted water-crosslinked polyethylene. Journal of Applied Polymer Science, **70**, 1075–1082 (1998).
DOI: 10.1002/(SICI)1097-4628(19981107)70:6<1075:: AID-APP4>3.0.CO;2-L

[17] Aizan W., Abdul Rahman W.: Design of silane crosslinkable HDPE compounds for automotive fuel tank application. Project no. 03-02-06-0089, Faculty of Chemical and Natural Resource Engineering, Universiti Teknologi Malaysia (2006).
http://eprints.utm.my/2782/1/74125.pdf

[18] Mallegol J., Carlsson D. J., Deschenes L.: A comparison of phenolic antioxidant performance in HDPE at 32–80°C. Polymer Degradation and Stability, **73**, 259–267 (2001).
DOI: 10.1016/S0141-3910(01)00086-6

[19] Yamazaki T., Seguchi T.: ESR study on chemical crosslinking reaction mechanisms of polyethylene using a chemical agent- II. The effect of phenolic antioxidants. Journal of Polymer Science Part A: Polymer Chemistry, **35**, 2431–2439 (1997).
DOI: 10.1002/(SICI)1099-0518(19970915)35:12<2431:: AID-POLA13>3.0.CO;2-8

[20] Catalina F., Pienado C., Allen N. S., Corrales T.: Chemiluminescence of polyethylene: The comparative antioxidant effectiveness of phenolic stabilizers in low-density polyethylene. Journal of Polymer Science Part A: Polymer Chemistry, **40**, 3312–3326 (2002). DOI: 10.1002/pola.10419

[21] Gachter R., Müller H.: Plastics additives handbook. Hanser Publishers, Munich (1993).

[22] Kumar M. S. C., Alagar M., Prabu A. A.: Studies on dynamic mechanical and mechanical properties of vinyloxyaminosilane grafted ethylene propylene diene terpolymer/linear low density polyethylene (EPDM-g-VOS/LLDPE) blends. European Polymer Journal, **39**, 805–816 (2003). DOI: 10.1016/S0014-3057(02)00285-9

[23] Shieh Y-T., Tsai T-H.: Silane grafting reactions of low-density polyethylene. Journal of Applied Polymer Science, **69**, 255–261 (1998). DOI: 10.1002/(SICI)1097-4628(19980711)69:2<255::AID-APP6>3.0.CO;2-M

[24] Ultsch S., Fritz H. G.: Crosslinking of LLDPE and VLDPE via graft-polymerized vinylteimethoxysilane. Plastics and Rubber Processing and Applications, **13**, 81–91 (1990).

[25] Shah G. B., Fuzail M., Anwar J.: Aspects of the crosslinking of polyethylene with vinyl silane. Journal of Applied Polymer Science, **92**, 3796–3803 (2004). DOI: 10.1002/app.20381

[26] Wong W. K., Varrall D. C.: Role of molecular structure on the silane crosslinking of polyethylene: The importance of resin molecular structure change during silane grafting. Polymer, **35**, 5447–5452 (1994). DOI: 10.1016/S0032-3861(05)80008-4

[27] Launer P. J.: Infrared analysis of organosilicon compounds: Spectra-structure correlations. in 'Silicone compounds register and review' (eds.: Anderson R., Arkles B. C., Larson G. L.) Petrarch Systems, Bristrol, 47–53 (1987).

[28] Smedberg A., Hjertberg T., Gustafsson B.: Crosslinking reactions in an unsaturated low density polyethylene. Polymer, **38**, 4127–4138 (1997). DOI: 10.1016/S0032-3861(96)00994-9

[29] Mizutani T., Tsukahara T., Ieda M.: The effects of oxidation on the electrical conduction of polyethylene. Journal of Physics D: Applied Physics, **13**, 1673–1679 (1980). DOI: 10.1088/0022-3727/13/9/015

[30] Haslam J., Willis H. A., Squirrel D. C. M.: Identification and analysis of plastics. Butterworth, London (1972).

[31] Andersson L. H. U., Hjertberg T.: The effect of different structure parameters on the crosslinking behavior and network performance of LDPE. Polymer, **47**, 200–210 (2006). DOI: 10.1016/j.polymer.2005.11.023

[32] ASTM D3124: Standard test method for vinylidene unsaturation in polyethylene by infrared spectrophotometry (1998).

[33] Alagar M., Abdul Majeed S. M., Selvaganapathi A., Gnanasundaram P.: Studies on thermal ageing and morphological characteristics of EPDM-g-VTES/LLDPE. European Polymer Journal, **42**, 336–347 (2006). DOI: 10.1016/j.eurpolymj.2005.07.013

[34] Alagar M., Abdul Majeed S. M., Nagendiran S.: Preparation and characterization of vinyltriethoxysilane grafted ethylene propylene diene terpolymer/linear low density polyethylene (EPDM-g-VTES/LLDPE) blends. Polymers for Advanced Technologies, **16**, 582–591 (2005). DOI: 10.1002/pat.626

Effects of antistatic agent on the mechanical, morphological and antistatic properties of polypropylene/organo-montmorillonite nanocomposites

W. S. Chow, W. L. Tham*

School of Materials and Mineral Resources Engineering, Engineering Campus, Universiti Sains Malaysia, 14300 Penang, Malaysia

Abstract. Polypropylene (PP) and PP/organo-montmorillonite (OMMT) compounds containing antistatic agent (3, 6 and 9 wt%) were prepared using co-rotating twin screw extruder followed by injection molding. PP/OMMT composites were prepared by mixing of PP, OMMT and maleated PP (PPgMAH). The mechanical properties of PP blends and PP/OMMT nanocomposites were studied by tensile and impact tests. The effect of antistatic agent (AA) on the surface resistivity of PP and PP/OMMT nanocomposites were studied. The morphological properties of PP blends and PP/OMMT nanocomposites were characterized by using field emission scanning electron microscopy (FESEM). The intercalation of OMMT silicates layer in PP nanocomposites was characterized using X-ray diffraction (XRD). The impact strength of PP blends and PP/OMMT nanocomposites did not vary significantly by the addition of antistatic agent. The tensile modulus and tensile strength of PP/OMMT nanocomposites were slightly decreased with the increasing loading of antistatic agents. From FESEM analysis, the dispersion of antistatic agent in the PP matrix can be revealed. In addition, the surface resistivity of PP/OMMT compound was affected by the loading of antistatic agent. XRD results indicated the formation of intercalated nanocomposites for PP/OMMT/AA.

Keywords: nanocomposites, polypropylene, organo-montmorillonite, antistatic agent, material testing

1. Introduction

Nowadays, plastics have replaced metals and become the material of choice in electronic components because they have higher flexibility, lighter weight, better colorability and higher cost effectiveness [1, 2]. The function of antistatic agent is to prevent the build-up of static electrical charge due to the transfer of electrons to the material surface. Electrostatic charging of composites can lead dust deposition, electric shocks and damages in electronic equipment [3]. Antistatic agent is able to dissipate or promote the decay of static electricity. In addition, an antistatic agent could improve processability, mold release, and give better internal and external lubrication. The antistatic agents are general 'soap like' molecules with a hydrophobic and a hydrophilic part. The hydrophilic part may consist of fatty acid esters, ethoxylated amine and phosphate esters which can migrate to the surface and attract a layer of water. This could lead to the enhancement of surface conductivity of a polymeric material [3]. The main function of the antistatic agent is to promote a conductive channel. A continuous water layer will be formed due to the attachment of vapor to the surface of the antistatic agent. The conductivity of the water layer increased when the number of ions increases, resulting in better antistatic properties of the polymeric materials [4–5].

Polypropylene (PP) is one of the most widely used polyolefin polymers because of its low cost, low density and high specific properties. The PP blends and composites find wide application in automotive parts, extruded profiles, cable insulation, footwear, and packaging industry. Clay minerals are composed of silicate layers with the fundamental unit in 1 nm thickness planar structure [6]. Montmorillonite (MMT) is a valuable mineral and is widely used in many industrial applications because of its high aspect ratio, plate morphology, natural abundance and cost effectiveness. The expandable layered silicates of MMT can be intercalated and/or exfoliated by polymer chain to form nanocomposites [7]. The dispersion of organically modified layered silicates (organoclay) in PP induces enhancement in mechanical properties, flame resistance, heat distortion temperature and barrier properties. Furthermore, these improvements are achieved at clay loadings as low as 5 wt% [8, 9]. For non-polar polymers such as polyethylene (PE) and PP, the interaction between polymer chains and MMT surface is relatively weak and the polymer chains are difficult to intercalate into MMT. Therefore, compatibilizers were often added to increase the degree of interaction between polymer chains and MMT [10, 11]. The properties improvement of nanocomposites is correlated with the intercalation/exfoliation and dispersion of clay layer silicate in polymer matrix. Exfoliation of polymer in layered silicate depends on several factors such as types of clay, organic modifier, and polymer matrix [12, 13]. In general, for PP/clay nanocomposites, a functionalized polymer such as PP grafted with maleic anhydride (PPgMAH) is added to improve the interfacial interaction and compatibility between PP and clays. It is believed that the enhancement of the PP properties depends on the molecular weight and grafting degree of PPgMAH and the relative ratio of PPgMAH/clay. Low grafting percentage of PPgMAH (typically 0.5–2%) hardly enhances the compatibility significantly. While, too much of PPgMAH may lead to the deterioration of nanocomposites properties [14].

In this work, the PP/OMMT compounds were first prepared by melt blending of PP, OMMT and PPgMAH. The aim of this study is to evaluate the effect of antistatic agent on the mechanical properties, morphology and surface resistivity of PP/OMMT nanocomposites. It is believed that the antistatic agent can be intercalated into the interlayer spacing of OMMT silicate layers, and thus reduce the migration of antistatic agent from the PP nanocomposites. As a result, the antistatic effects can be maintained for a longer time.

2. Experimental

2.1. Materials

PP copolymer (SM240) was supplied by Titan (M) Sdn Bhd. The MFI and density of PP is 25 g/10 min and 0.9 g/cm³, respectively. The OMMT (1.30P) was supplied by Nanocor, USA. PPgMAH with a percentage of MAH 1.47% was supplied by Eastman Chemical, USA. The antistatic agent (Irgastat P 18) based on polyamide/polyether block amide was supplied by Ciba Specialty Chemical (M) Sdn Bhd. PP containing 3, 6, and 9 wt% of antistatic agent (AA) is designated as PP/AA3, PP/AA6 and PP/AA9, respectively. PP/OMMT compounds [denoted as (PP/OMMT)MB] were first prepared by mixing PP, OMMT and PPgMAH at a ratio of 87:3:10. The PP/OMMT nanocomposites containing 3, 6, and 9 wt% of AA is labeled as PP/OMMT/AA3, PP/OMMT/AA6 and PP/OMMT/AA9, respectively.

2.2. Preparation of PP nanocomposites

2.2.1. Co-rotating twin-screw extrusion

Prior to extrusion, OMMT, PPgMAH and antistatic agent were dried in an oven for 3 hours at 80°C. The extrusion processes of PP/AA blends and PP/OMMT/AA composites were carried out using a co-rotating twin screw extruder (model PSM 30, Sino Alloy, Taiwan) with a *L/D* 40 and intermeshing screw configuration. The screw speed was set at 150 rpm. The processing temperature was set in the range of 155–175°C. Further, the PP/OMMT/AA composites were prepared by mixing (PP/OMMT) MB with the antistatic agent at three different loadings, i.e. 3, 6 and 9 wt%.

2.2.2. Mini vertical injection molding

The PP samples were prepared by using a mini vertical injection molding (model RR/TSMP, Ray-Ran Test Equipment LTD, United Kingdom). The barrel temperature was set in the range of 180–185°C. The mold temperature was set at 80°C.

2.3. Materials characterization

2.3.1. Tensile tests

The samples were prepared by compression molding method. Dumbbell specimens were cut from 1 mm thickness compression-molded sheet. Tensile test was carried out with an Instron tensile machine (model 3366, USA) at 27°C (50% relative humidity), according to ASTM D638, at a crosshead speed of 50 mm/min. Tensile modulus, tensile strength and elongation at break of the PP samples were evaluated from the stress-strain data.

2.3.2. Impact tests

The Charpy impact strength of PP samples was determined according to ASTM D5942 by using a pendulum impact machine (Zwick, USA). The Charpy impact tests were done for both un-notched and single-notched specimens at room temperature. A pendulum with 7.5 J was selected for the impact tests. For unnotched specimen, the Charpy impact strength (a_{cU}), was calculated using Equation (1). For single-notched specimens, the Charpy impact strength (a_{cN}) was calculated using Equation (2):

$$a_{cU} = \frac{W}{h \cdot b} \cdot 10^{-3} \tag{1}$$

$$a_{cN} = \frac{W}{h \cdot b_N} \cdot 10^{-3} \tag{2}$$

where W – corrected energy absorbed by breaking the test specimen [J], h – thickness of the test specimen [mm], b – width of the test specimen [mm], b_N – remaining width at the notch base of the test specimen [mm].

2.3.3. Field emission scanning electron microscopy (FESEM)

The fracture surface of PP/OMMT composites was investigated using a field emission scanning electron microscopy (FESEM, Zeiss Supra 35VP) at an accelerator voltage of 15 kV. The fracture surface of the PP specimens was sputter-coated with a thin gold-palladium layer in vacuum chamber for conductivity before examination.

2.3.4. X-ray diffraction (XRD)

X-ray diffraction (XRD) analyses of OMMT, (PP/OMMT)MB and PP/OMMT/AA composites were performed on a Siemens Diffractometer D5000 machine (Germany) using CuK$_\alpha$ radiation. The samples were scanned in a fixed step size, 0.040° with a step time of 10 s in the range of 2–10°. The d-spacing (d) of the interlayer gallery of OMMT and the PP/OMMT nanocomposites was calculated by using Bragg's Law (c.f. Equation (3)):

$$n\lambda = 2d\sin\theta \tag{3}$$

2.3.5. Surface resistivity tests

Surface resistivity tests of the PP samples were carried out according to ASTM D-257-99 using Advantest R8340 Ultra High Resistance Meter. The surface resistivity of PP composites (before and after exposure to room temperature for 3–6 months) was determined by using Equation (4). The thickness of specimen, test voltage and test time is 1mm, 500 V and 1 min, respectively (Equation (4)):

$$\rho_s = \frac{\pi(D+d)}{D-d} \cdot R_s \tag{4}$$

where, ρ_s – surface resistivity [ohm/sq], R_s – surface resistance [ohm], π – ratio of the circumference of a circle to its diameter equal with 3.14, D – inside diameter of guard electrode [cm], d – diameter of main electrode [cm].

3. Results and discussion

3.1. Tensile properties

Figure 1 shows the effect of antistatic agents (AA) on the tensile modulus of PP and (PP/OMMT)MB. The tensile modulus of PP was increased by the addition of OMMT. This is due to the reinforcing effects of OMMT layered silicates. According to Ding *et al.* [15], the uniformly dispersed MMT tactoid with intercalated structures could significantly increase the mechanical properties of a polymer composite even at a low content of OMMT fillers. The OMMT filler could influence the orientation of
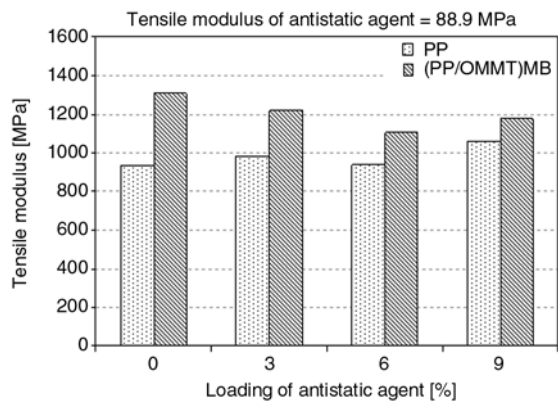
Figure 1. Effect of antistatic agents (AA) on the tensile
modulus of PP and (PP/OMMT)MB composites

the lamella in the polymer crystalline [16]. The
increment of degree of crystallinity could lead to
the enhancement of stiffness and modulus of the
PP. Similar observation also reported for various
different types of polymer/clay nanocomposites.
The tensile modulus of polyamide 6/polypropylene
(PA6/PP) blend was increased by the addition of
organoclay. This is due to high stiffness of silicate
layers, the large aspect ratio and surface area of sil-
icate layers and constraining effect of these layers
on molecular motion of polymer chains [17, 18]. In
Figure 1, it can be also observed that the tensile
modulus of PP was slightly increased by the addi-
tion of antistatic agent compare to pure PP. How-
ever, the increments of tensile modulus are not
significant between PP and PP/AA. The tensile
modulus of (PP/OMMT)MB was decreased by the
addition of antistatic agents. Note that the tensile
modulus of antistatic agent is 88.9 MPa. The anti-
static agent is more flexible than (PP/OMMT)MB.
Thus, the addition of antistatic agents could lead to
the reduction of tensile modulus of PP/OMMT
composites. According to Kusmono *et al.* [17], the
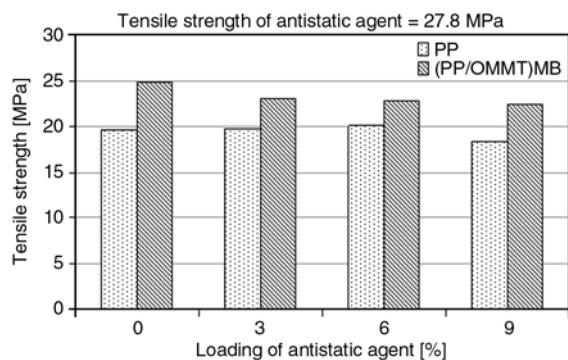
tensile modulus of PA6/PP nanocomposites was
reduced by the addition of SEBS-g-MA due to the
elastomeric nature of the SEBS-g-MA. Figure 2
shows the effect of antistatic agents (AA) on the
tensile strength of PP and (PP/OMMT)MB. The
tensile strength of (PP/OMMT)MB is relatively
higher than that of PP. This is attributed to the
improved interfacial interaction between PP and
OMMT in the presence of PPgMAH. According to
Mishra *et al*. [19], the intercalation of polymer
chain inside silicate layers leads to an increase in
the surface area of interaction between clay and
polymer matrix. Hence, the tensile strength of the
nanocomposite increases slightly as compared to
the pristine equivalent. The tensile strength of
PP/AA blends (3–9% of AA) is comparable to neat
PP. It can be observed that the antistatic agents did
not influence much the mechanical properties of
PP. The tensile strength of (PP/OMMT)MB was
slightly decreased by the addition of antistatic
agents. This is attributed to the high flexibility and
plasticization effects of antistatic agent. Figure 3
shows the effect of antistatic agents (AA) loading
on the elongation at break of PP and (PP/OMMT)
MB. The elongation at break for (PP/OMMT)MB
composite is lower than that of pure PP. The load-
ing of filler may increase the stress concentration
and causes the composite to fail in a brittle manner
as compared to PP [20, 21]. The elongation at break
of (PP/OMMT)MB was not influenced by the addi-
tion of antistatic agent. Thus, it is believed that the
antistatic agents' main function is to dissipate static
electric charge accumulated on the surface of plas-
tic, rather than to alter the mechanical properties of
a plastic. However, the elongation at break of PP
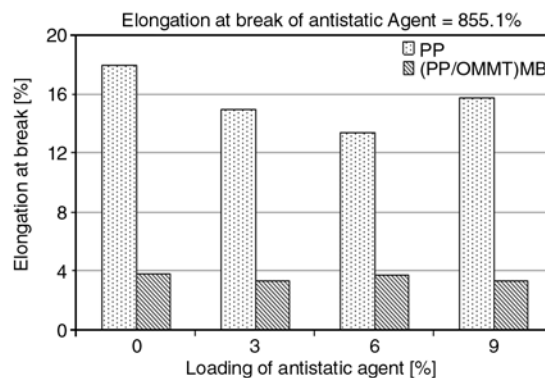was slightly decreased by the addition of antistatic

Figure 3. Effect of antistatic agents (AA) on the elonga-
tion at break of PP and (PP/OMMT)MB com-
posites

Figure 2. Effect of antistatic agents (AA) on the tensile
strength of PP and (PP/OMMT)MB composites

agent. According to Li *et al.* [3], phase separation occurred between the AA and PP matrix during co-spinning process. The AA forms the antistatic mechanism with polymer, the polar radical groups (e.g. C–O–C, –OH and SO_3Na) attract atmospheric moisture and transfer moisture from the polymer surface to inner AA phases. The charge transmission path of AA in polymer matrix is formed by the network of AA phases, and result in dissipation of static charges. When the content of antistatic agent is increased, more transmission paths are formed. The build of transmission paths of AA in PP may restrict the movement of polymer chains and consequently reduce the elongation at break of PP.

3.2. Impact properties

The effect of antistatic agents (AA) on the un-notched Charpy impact strength of PP and (PP/OMMT)MB composite is shown in Figure 4. It can be seen that the loading of antistatic agents (e.g. 3, 6 and 9%) do not affect the impact strength of PP. The impact strength of PP/AA is comparable with neat PP. The impact strength of PP was slightly reduced by the addition of OMMT. According to Ding *et al.*, [15], the OMMT was dispersed in the PP matrix on the nanometer scale and part of the OMMT was intercalated by PP chains. Thus, the OMMT layered silicates may confine the segmental movement of PP macromolecules. However, the impact strength of (PP/OMMT)MB is comparable to the neat PP. This is attributed to the PPgMAH component that can improve the interfacial interaction between PP and OMMT. A better interfacial interaction could lead to improvement of impact strength with high absorption energy during
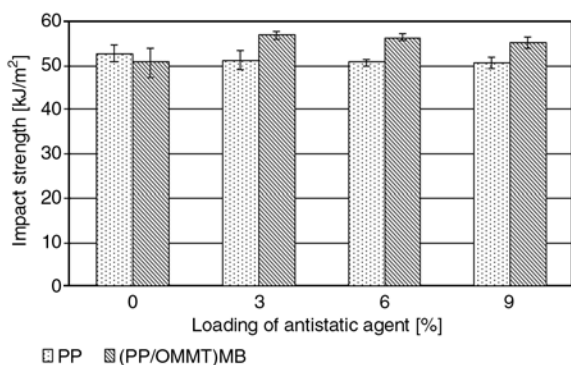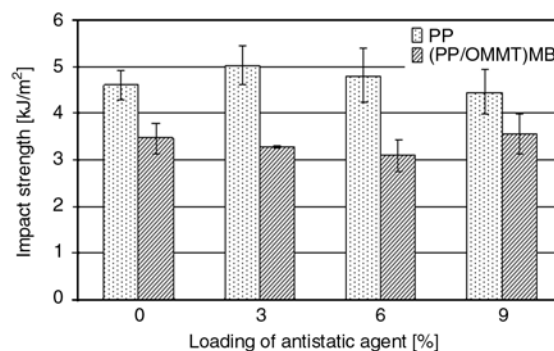
Figure 5. Effect of antistatic agents (AA) on the notched Charpy impact strength of PP and (PP/OMMT)MB composites

impact deformation. According to Kusmono *et al.* [17], the high impact strength of PA6/PP/OMMT could be attributed to the improved interfacial interaction resulting from the formation of maleic anhydride grafted styrene-ethylene-butylenes-styrene (SEBS-g-MA) in the composites. It is interesting to note that the impact strength of (PP/OMMT)MB was slightly increased by the addition of antistatic agent. This is due to the flexibility and ductility characteristics of the antistatic agent. Accordingly, the PP/OMMT/AA samples will absorb more energy during impact deformation. According to Cai *et al.* [20], the grafted polymer might play the role of a bumper interlayer around the filler, while absorbing impact energy and preventing initiation of cracks. A further improvement of nanocomposites' ductility is exhibited as an increase in flexibility of the grafted polymer chains. Figure 5 shows the effect of antistatic agents on notched Charpy impact strength of PP and (PP/OMMT)MB composite. The different loading of antistatic agents in PP and (PP/OMMT) MB do not show any alteration on impact strength obviously. However, the PP/AA blends exhibited higher impact strength compared to PP/OMMT/AA composites. The notched samples were fractured easily compared to the un-notched ones. The value of impact strength for notched samples decrease rapidly compared to un-notched samples, especially for (PP/OMMT)MB nanocomposite. This may be due to the dispersed and intercalated OMMT layer silicates in the PP matrix which could restrict the segmental movement of PP macromolecules and further decrease its impact strength [19].

Figure 4. Effect of antistatic agents (AA) on the un-notched Charpy impact strength of PP and (PP/OMMT)MB composites

Table 1. Interlayer spacing and surface resistivity of PP and (PP/OMMT)MB

Materials designation	2θ	d_{001} [nm]	Surface resistivity [ohm/sq]			Category
			control	3 months	6 months	
AA	–	–	10^8	10^8	10^8	antistatic
PP	–	–	$>10^{12}$	$>10^{12}$	$>10^{12}$	insulator
PP/AA3	–	–	$>10^{12}$	$>10^{12}$	$>10^{12}$	insulator
PP/AA6	–	–	10^{11}	10^{11}	10^{11}	antistatic
PP/AA9	–	–	10^{11}	10^{11}	10^{11}	antistatic
OMMT	3.32	2.66	10^8	10^8	10^8	–
PP/OMMT	3.24	2.72	$>10^{12}$	$>10^{12}$	$>10^{12}$	insulator
PP/OMMT/AA3	3.22	2.74	$>10^{12}$	$>10^{12}$	$>10^{12}$	insulator
PP/OMMT/AA6	3.20	2.76	$>10^{12}$	$>10^{12}$	$>10^{12}$	insulator
PP/OMMT/AA9	3.18	2.77	10^{11}	10^{11}	10^{11}	antistatic

3.3. Surface resistivity

Table 1 shows the effect of antistatic agent (AA) on the surface resistivity of PP before and after exposure to room temperature for 3–6 months. It can be seen that the surface resistivity of all the samples remained unchanged for the duration of 6 months. The surface resistivity of antistatic agent is about 10^8 ohm/sq. Neat PP and PP/AA3 with 10^{12} ohm/sq surface resistivity was in the category of insulator materials. However, the surface resistivity of PP/AA6 and PP/AA9 blends was recorded at 10^{11} ohm/sq. This indicates that both of the PP/AA6 and PP/AA9 could be categorized as antistatic materials. The surface resistivity of PP/AA6 and PP/AA9 were decreased by the incorporation of antistatic agent. However, PP/AA3 did not show significant changing of surface resistivity because the content of antistatic agent unable imparts antistatic properties on PP. Accordingly the probability of migration for the hydrophilic groups to the material surface to attract water is low. Table 1 also shows the effect of antistatic agent (AA) on the surface resistivity of (PP/OMMT)MB composites. Surface resistivity of PP/OMMT, (PP/OMMT)/AA3 and (PP/OMMT)/AA6 are more than 10^{12} ohm/sq, while (PP/OMMT)/AA9 showed the surface resistivity of 10^{11} ohm/sq. It is worth noting that the surface resistivity of PP/OMMT/AA9 remained 10^{11} ohm/sq for 6 months. This indicates that (PP/OMMT)/AA9 nanocomposites could exhibits antistatic behaviors. However, PP/OMMT, (PP/OMMT)/AA3 and (PP/OMMT)/AA6 nanocomposites were classified in the insulator category where the surface resistivity recorded at 10^{12}–10^{16} ohm/sq. (PP/OMMT)/AA3 and (PP/OMMT)/AA6 nanocomposites could not achieve the antistatic behavior; this may be due to the insufficient and

lower content of antistatic agent. In addition, it is believed that the antistatic agent could intercalate into the OMMT silicate layers. This will reduce the possibility of antistatic agent migrate to the PP sample surface. One may believe that an optimum migration rate has to be achieved in order to facilitate the migration of neighbor's antistatic agent to the surface from the bulk, but it should not lose the whole amount of antistatic agent too fast. On the other hand, when 9% antistatic agent added in PP/OMMT, it is able to give the antistatic ability due to the migration of antistatic agent to the PP composites surface. According to Ratnayake and Haworth [22], the water contact angles were increased dramatically by adding clay into PP/antistatic agent blends. This is because most of functional group of antistatic agent interacts with clay particles, rather than migrating onto the surface, especially at low concentration of antistatic agent.

3.4. X-ray diffraction (XRD)

The 2θ and d-spacing of OMMT and (PP/OMMT) MB with and without AA was shown in Table 1. The (PP/OMMT)MB nanocomposite shows a small shoulder which appeared at 2θ = 3.24°. The corresponding d-spacing of (PP/OMMT)MB is d_{001} = 2.72 nm. This is due to the intercalation of clay layers by the addition of PPgMAH. According to Bertini *et al.* [23], the patterns of the PP/OMMT composite provides direct evidence of the intercalation. A shoulder shifted to lower diffraction angles of 2θ with the presence of montmorillonite. A higher content of PPgMAH improves the intercalation and clay dispersability in the PP matrix [22]. Interesting to note that, the d_{001} peak of PP/OMMT has been broadened by the addition of antistatic
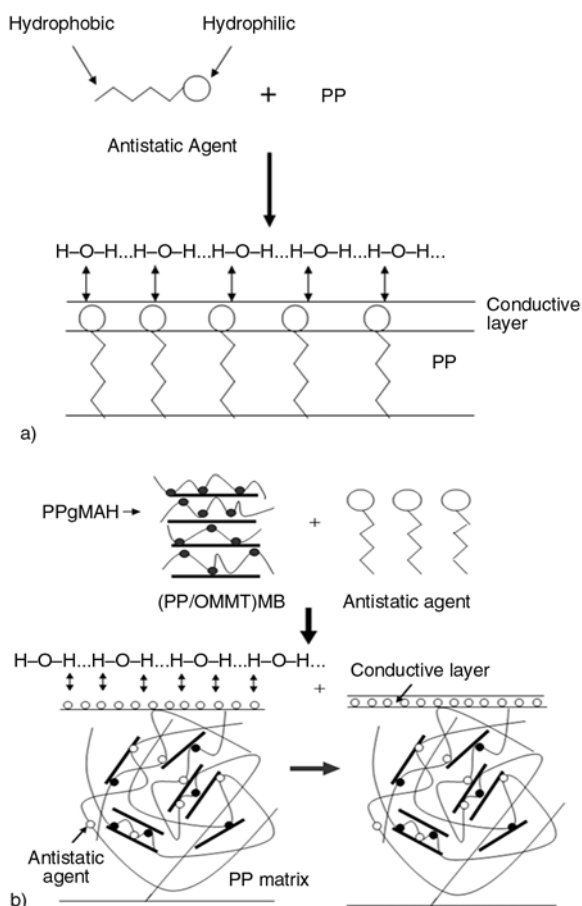
Figure 6. a – Possible interaction mechanism between PP and AA, b – Possible interaction and intercalation mechanism of PP/OMMT/AA nanocomposites

agent. Thus, it is believed that the antistatic agent is able to intercalate into the clay interlayer gallery. It can be seen that the d-spacing of (PP/OMMT)MB increased with the increasing concentration of AA. The PP/OMMT/AA9 shows a $2\theta = 3.18°$, which is corresponding to the d-spacing of 2.78 nm. According to Ratnayake and Haworth [22], the XRD results clearly show that the shifting of peaks to a lower Bragg angle as the loading of antistatic agent (AA) in PP/OMMT composites increasing. They also reported that by the addition of 0.5% (by weight) of AA in composite, the highest interlayer spacing was achieved. However, a further increase of additive concentration in composite is not effective in modifying the interlayer spacing, probably because of the migration of additional antistatic agent additive onto the surface. From Table 1, it can be seen that the intercalation and exfoliation of OMMT layered silicate in PP composites could be correlated to the surface resistivity of the composites. For the PP/OMMT/AA9, when d_{001} value of

the interlayer spacing is sufficient, it is possible for the excess amount of AA to migrate to the materials surface and thus provide the antistatic characteristics. Figure 6a shows the possible interaction mechanism between PP and AA. It can be seen that the AA can migrate to the PP surface to form a conductive layer. Figure 6b shows the possible interaction and intercalation mechanism in PP/OMMT/AA nanocomposites. Note that the low molecular weight AA can intercalate into the OMMT layer silicate. If the amount of AA is sufficient, in addition to the intercalation of AA, it is believed that some amount of the AA can migrate to the PP surface and form a conductive layer.

3.5. Field emission scanning electron microscopy (FESEM)

Figure 7a shows the FESEM micrographs taken from the impact fractured surface of neat PP. Figure 7b shows the FESEM micrographs taken from the impact fractured surface of PP/AA blends. There were two types of small particles observed from the sample fractured surface. It can be seen that some particles (shown by pink arrow in Figure 7b) are in the range of 5 to 6 µm which can be observed in Figure 7a as well. Recall that the PP used in this study is a type of PP copolymer that contains ethylene and propylene. The ethylene is distributed and dispersed in the PP matrix. Hence, the small particles protruded on the fractured surface of PP matrix could be assigned to ethylene. Besides, there are lots of small particles about 0.5–1.0 (shown by orange arrow in Figure 7b) were also observed on the fractured plane. It is believed that the small particles present on the fracture surface of PP/AA correspond to the antistatic agent. Figures 7c and 7d shows the FESEM micrographs taken from the impact fractured surface of PP/OMMT and PP/OMMT/AA composites. Particle shown by blue arrow could correspond to OMMT. EDX was used to confirm the OMMT elements. Figure 8 shows the EDX spectra taken from PP/OMMT/AA (c.f. Figure 7d), there were 5 elements can be observed, i.e. C, O, Si, Na and Ca. According to Chow *et al.* [24], the carbon is due to the octadecylamine intercalant used. O, Si, Na and Ca elements represent components of OMMT. From the FESEM micrograph taken from the PP/OMMT/AA nanocomposites, note that the anti-
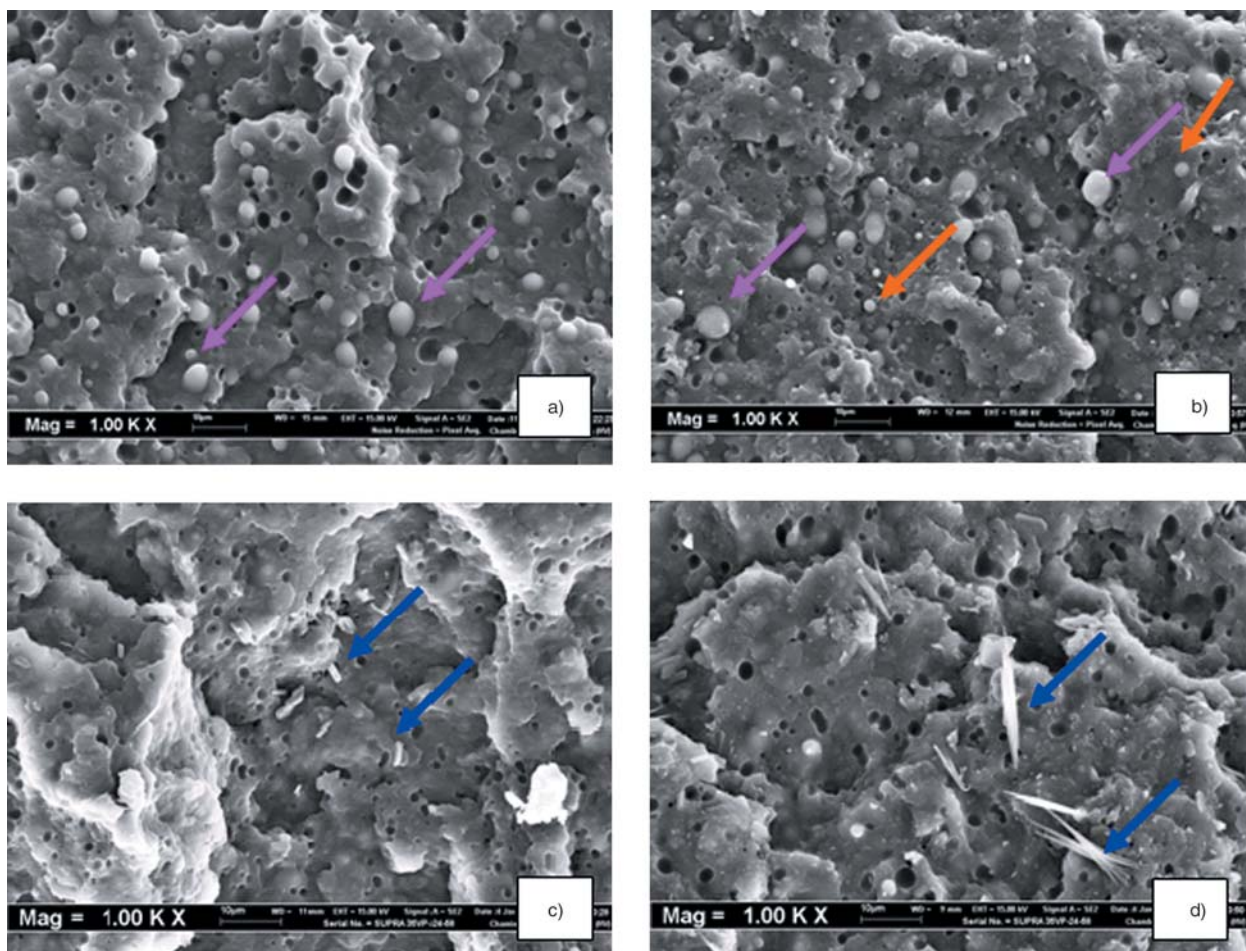
Figure 7. a – FESEM micrographs taken from the impact fractured surface of PP, b – FESEM micrographs taken from the impact fractured surface of PP/AA blends, c – FESEM micrographs taken from the impact fractured surface of PP/OMMT composites, d – FESEM micrographs taken from the impact fractured surface of PP/OMMT/AA composites
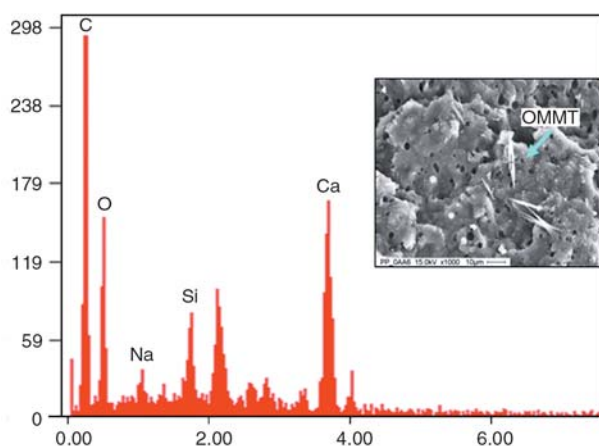

Figure 8. EDX spectra taken from the PP/OMMT/AA nanocomposites

static agent particles could not be observed on the fractured surface. According to Ratnayake and Haworth [22], they suggested that functional slip additives and antistatic agent will intercalate into clay galleries. They observed through TEM micro-graph, clay particles are separated into much smaller stacks and dispersed homogenously throughout the PP matrix when antistatic agent and PPgMAH are added. It can be attributed to the co-intercalation of AA with PPgMAH that will increase the clay dispersibility in PP matrix. Therefore, the wettability and intercalation capability of nanocomposites increases with the increasing of the polarity in PPgMAH and antistatic agent.

4. Conclusions

This study reveals the effects of antistatic agent (AA) on the mechanical properties, morphology and surface resistivity of PP and (PP/OMMT)MB nanocomposites. The AA only give minor effects (or in some case, insignificant effects) on the tensile modulus, strength, elongation at break and impact strength (notched and un-notched) of the PP and (PP/OMMT)MB nanocomposites. The incor-

poration of AA and PPgMAH may provide better wettability and interfacial interaction between OMMT and PP matrix. The surface resistivity of the PP/OMMT nanocomposites could be correlated to the concentration of AA and intercalation/exfoliation-ability of the OMMT. It is hypothesized that the AA could be intercalated into the OMMT layered silicates which could influence the surface resistivity of the PP and its nanocomposites. It is worth to note that the surface resistivity of PP/OMMT/AA9 was remained 10^{11} ohm/sq even after exposure to room temperature for 6 months.

Acknowledgements

References

[1] Harper C. A.: Modern plastics handbook. McGraw-Hill, New York (1999).

[2] Amarasekera J.: Conductive plastics for electrical and electronic applications. Reinforced Plastics, **49**, 38–41 (2005).
DOI: 10.1016/S0034-3617(05)70734-7

[3] Li C., Liang T., Lu W., Tang C., Hu X., Cao M., Liang J.: Improving the antistatic ability of polypropylene fibers by inner antistatic agent filled with carbon nanotubes. Composites Science and Technology, **64**, 2089–2096 (2004).
DOI: 10.1016/j.compscitech.2004.03.010

[4] Ma C-C., Chen Y-J., Kuan H-C.: Polystyrene nanocomposites materials: Preparation, morphology, mechanical, electrical and thermal properties. Journal of Applied Polymer Science, **98**, 2266–2273 (2005).
DOI: 10.1002/app.23221

[5] Hong C. K., Kim M-J., Oh S. H., Lee Y-S., Nah C.: Effects of polypropylene-g-(maleic anhydride/styrene) compatibilizer on mechanical and rhelogical properties of polypropylene/clay nanocomposites. Journal of Industrial and Engineering Chemistry, **14**, 236–242 (2008).
DOI: 10.1016/j.jiec.2007.11.001

[6] Hausman K.: Permanent antistatic agents offers long term performance for films and containers. Plastic, Additives and Compounding, **9**, 40–42 (2007).
DOI: 10.1016/S1464-391X(07)70070-3

[7] Qin H., Zhang S., Zhao C., Feng M., Yang M., Shu Z., Yang S.: Thermal stability and flammability of polypropylene/montmorillonite composites. Polymer Degradation and Stability, **85**, 807–813 (2003).
DOI: 10.1016/j.polymdegradstab.2004.03.014

[8] Ray S., Okamoto M.: Polymer/layered silicate nanocomposites: A review from preparation to processing. Progress in Polymer Science, **27**, 1539–1641 (2003).
DOI: 10.1016/j.progpolymsci.2003.08.002

[9] Xanthos M.: Functional fillers for plastics. Wiley, Weinheim (2005).

[10] Shi D., Yu W., Robert Li K. Y., Ke Z., Yin J. H.: An investigation on the dispersion of montmorillonite (MMT) primary particles in PP matrix. European Polymer Journal, **43**, 3250–3257 (2007).
DOI: 10.1016/j.eurpolymj.2007.05.030

[11] Valera-Zaragoza M., Ramírez-Vargas E., Medellín-Rodríguez F. J., Huerta-Martínez B. M.: Thermal stability and flammability properties of heterophasic PP-EP/EVA/organoclay nanocomposites. Polymer Degradation and Stability, **91**, 1319–1325 (2006).
DOI: 10.1016/j.polymdegradstab.2005.08.011

[12] Imren D., Boztug A., Yilmaz E., Bayram Zengin H.: Viscometric investigation of compatibilization of the poly(vinyl chloride)/poly(ethylene-co-vinyl acetate) blends by terpolymer of maleic anhydride-styrene-vinyl acetate. Journal of Molecular Structure, **891**, 329–332 (2008).
DOI: 10.1016/j.molstruc.2008.04.003

[13] Rohlmann C. O., Failla M. D., Quinzani L. M.: Linear viscoelasticity and structure of polypropylene-montmorillonite nanocomposites. Polymer, **47**, 7795–7804 (2006).
DOI: 10.1016/j.polymer.2006.08.044

[14] García-López D., Picazo O., Merino J. C., Pastor J. M.: Polypropylene-clay nanocomposites: Effect of compatibilizing agents on clay dispersion. European Polymer Journal, **39**, 945-950 (2003).
DOI: 10.1016/S0014-3057(02)00333-6

[15] Ding C., Jia D. M., He H., Guo B. C., Hing H. Q.: How organo-montmorillonite truly affects the structure and properties of polypropylene. Polymer Testing, **24**, 94–100 (2005).
DOI: 10.1016/j.polymertesting.2004.06.005

[16] Osman M. A., Rupp J. E. P., Suter U. W.: Tensile properties of polyethylene-layered silicate nanocomposites. Polymer, **46**, 1653–1660 (2005).
DOI: 10.1016/j.polymer.2004.11.112

[17] Kusmono, Mohd Ishak Z. A., Chow W. S., Takeichi T., Rochmadi: Influence of SEBS-g-MA on morphology, mechanical and thermal properties of PA6/PP/organoclay nanocomposites. European Polymer Journal, **44**, 1023–1039 (2008).
DOI: 10.1016/j.eurpolymj.2008.01.019

[18] Chow W. S, Mohd Ishak Z. A.: Mechanical, morphological and rheological properties of polyamide 6/organo-montmorillonite nanocomposites. Express Polymer Letters, **2**, 77–83 (2007).
DOI: 10.3144/expresspolymlett.2007.14

[19] Mishra J. K., Hwang K-J., Ha C-S.: Preparation, mechanical and rheological properties of a thermoplastic polyolefin (TPO)/organoclay nanocompsite with reference to the effect of maleic anhydride modified polypropylene as a compatibilizer. Polymer, **46**, 1995–2002 (2005).
DOI: 10.1016/j.polymer.2004.12.044

[20] Cai L. F., Mai Y. L., Rong M. Z., Ruan W. H., Zhang M. Q.: Interfacial effects in nano-silica/polypropylene composites fabricated by in-situ chemical blowing. Express Polymer Letters, **1**, 2–7 (2007).
DOI: 10.3144/expresspolymlett.2007.2

[21] Hull D., Clyde T. W.: An introduction to composite materials. Cambridge University Press, Cambridge (1996).

[22] Ratnayake U. N., Haworth B.: Polypropylene-clay nanocomposites: Influence of low molecular weight polar additives on intercalation and exfoliated behavior. Polymer Engineering and Science, **46**, 1008–1015 (2006).
DOI: 10.1002/pen.20573

[23] Bertini F., Canetti M., Audisio G., Costa G., Falqui L.: Characterization and thermal degradation of polypropylene-montmorillonite nanocomposites. Polymer Degradation and Stability, **91**, 600–605 (2005).
DOI: 10.1016/j.polymdegradstab.2005.02.027

[24] Chow W. S., Mohd Ishak Z. A., Kanger-Kocsis J., Apostolov A. A., Ishiaku U. S.: Compatibilizing effect of maleated polypropylene on the mechanical properties and morphology of injection molded polyamide 6/polypropylene/organoclay nanocomposites. Polymer, **44**, 7427–7440 (2003).
DOI: 10.1016/j.polymer.2003.09.006

Friction and wear of HNBR with different fillers under dry rolling and sliding conditions

D. Xu[1], J. Karger-Kocsis[1,2]*, A. K. Schlarb[1]

[1]Institut für Verbundwerkstoffe GmbH (Institute for Composite Materials), University of Kaiserslautern,
 Erwin-Schrödinger-Str. 58, D-67663 Kaiserslautern, Germany
[2]Department of Polymer Engineering, Faculty of Mechanical Engineering, Budapest University of Technology and
 Economics, Műegyetem rkp. 3., H-1111 Budapest, Hungary

Abstract. Peroxide cured hydrogenated acrylonitrile/butadiene rubber (HNBR) compounds with 20 parts per hundred rubber (phr) active fillers, such as carbon black (CB), multiwall carbon nanotube (MWCNT) and silica were produced and their friction and wear properties under unlubricated rolling and sliding conditions were evaluated. The network-related properties of the HNBR compounds were deduced from dynamic-mechanical thermal analysis (DMTA). The coefficient of friction (COF) and the specific wear rate (W_s) were determined in different home-made test rigs. The CB and MWCNT containing HNBR compounds exhibited the best resistance to rolling and sliding wear, respectively, among the HNBR systems studied. The worn surfaces were inspected in scanning electron microscope (SEM) and the wear mechanisms were analyzed and discussed in respect to the types of wear and fillers.

Keywords: rubber, reinforcement, HNBR, friction, wear

1. Introduction

Polymers are used in increasing amount in such technical parts where friction and wear properties are key factors. Wear resistant polymeric composites usually contain various fillers and reinforcements. Carbon black (CB), multiwall carbon nanotube (MWCNT) and silica are commonly used or considered as promising additives for rubbers to achieve high wear resistance.

CB is a 'preformed' nanofiller, composed of amorphous carbon, which has a high specific surface. It is mainly used as pigment and reinforcement in various rubber and plastic products. The abrasion wear properties of CB filled rubber products are excellent. However, the related products are black. When there is a special demand for colored products, silica (SiO_2) is often adopted to replace CB.

By increasing the interaction between rubber matrices and silica, using different silanes, rubber compounds with very good abrasion resistance can be produced (e.g. [1]). Multiwall carbon nanotube (MWCNT) has high stiffness, strength and aspect ratio. MWCNT-containing polymer composites have outstanding mechanical performance, strongly improved electric and thermal conductivities if the nanotubes are well dispersed (for which, in analogy with organoclays, the term exfoliated is also used) and well adhered to the matrix [2]. A large body of research works addressed already the use of CB, silica and MWCNT in wear resistant polymer systems [1, 3–13], however, only few of them were dealt with hydrogenated acrylonitrile/butadiene rubber (HNBR) [14–16].

In our previous paper [17], MWCNT and silica were introduced in 10 and 30 parts per hundred rubber (phr) into a peroxide-cured HNBR in order to enhance the resistance to both sliding and rolling wear. In the present work, the three kinds of fillers (CB, MWCNT and silica; 20 phr for each) were added in the HNBR and their effects on the dry rolling and sliding wear against steel were checked and compared to those of the unfilled HNBR. Note that this filler amount is quite low for rubber recipes. However, when MWCNT is added in more than 20 phr it is undergoing considerable attrition and breakage. Further, though the above fillers are different in their chemical build-up and physical structure, their tribological functions can still be compared because all of them are active (i.e. improving the stiffness and strength characteristics) rubber fillers. The rolling and sliding friction and wear properties were determined in orbital rolling ball (steel)-on-plate (rubber) (Orbital-RBOP), pin (steel)-on-plate (rubber) (POP), roller (steel)-on-plate (rubber) (ROP) and oscillating cylinder (steel) on plate (rubber) (fretting) test rigs. Dynamic-mechanical thermal analysis (DMTA) was used to deduce apparent network-related characteristics. The coefficient of friction (COF) and specific wear rate (W_s) were determined for each tribotest. The worn surfaces were inspected in scanning electron microscope (SEM) and the wear mechanisms were concluded and discussed as a function of both wear and filler types.

2. Experimental

2.1. Materials

The composition of the peroxide curable HNBR was as follows: HNBR (Therban® LT VP/KA 8882 of Lanxess, Leverkusen, Germany; acrylonitrile content: 21%, Mooney viscosity ML(1+4) at 100°C = 74) – 100 part, diphenylamine-based thermostabilizer (Luvomaxx CDPA of Lehmann & Voss, Hamburg, Germany) – 1.1 part, zinc-containing mercapto-benzimidazole compound (Vulcanox® ZMB 2/C5 of Lanxess) – 0.4 part, di(tert-butylperoxyisopropyl) benzene (Perkadox 14-40 B-PD of Akzo-Nobel, Düren, Germany; active peroxide content: 40%) – 7.5 part, MgO – 2 part, triallyl isocyanurate – 1.5 part, ZnO – 2 part. Note that the amount of the listed additives corresponds to

their phr content in the recipe. This mix of practical use was produced separately and provided by Lanxess. The curing time of this base mix to reach 90% crosslinking was ca. 10 min at $T = 175°C$. This peroxide curable HNBR was mixed with 20 phr CB (N550), unmodified MWCNT (Baytubes® C 150 P from Bayer MaterialScience, Leverkusen, Germany) and silica (Ultrasil® VN2 of Degussa, Frankfurt, Germany), respectively, on a two-roll mixing mill (LRM-150BE of Labtech, Bangkok, Thailand) at ca. 40°C by setting a friction ratio of 1.15.

Curing of the CB, MWCNT and silica filled HNBR to about 2 mm thick sheets (100×100 mm^2 surface) occurred at $T = 175°C$ for 15 min in a laboratory press. Specimens for the investigations listed below were cut from these sheets.

The samples prepared are referred to as HNBR-PURE, HNBR-20CB, HNBR-20MWCNT and HNBR-20ULTRASIL, respectively, in the text. The digits in the designations represent the content of fillers in phr.

2.2. Testing

2.2.1. Dynamic-mechanical thermal analysis (DMTA)

DMTA spectra were recorded on rectangular specimens (length / 40 mm / × width / 10 mm / × thickness) in tensile mode with a superimposed sinusoidal 0.01% strain at a static preload 0.01 N. The frequency was 10 Hz and the spectra were measured in a temperature range from –100 to +100°C using a Q800 device of TA Instruments (New Castle, DE, USA). From –100°C, the temperature was increased by 5°C per step and for each step the temperature was stabilized for 3 min.

2.2.2. Density determination

For the density determination the Archimedes principle (buoyancy method with water) was adopted according to the standard ISO 1183.

2.2.3. Shore A hardness

The Shore A hardness of the composites was measured according to ISO 868 using a hardness measuring device of Zwick (Ulm, Germany).

2.2.4. Rolling and sliding wear

Testing

To evaluate the rolling friction and wear of the composites, an orbital rolling ball (steel)-on-plate (rubber) (Orbital-RBOP) home-made test rig was used. In the rig, the rubber sheet was worn by a steel ball (100Cr6, diameter: 14 mm, arithmetical roughness R_a: 1 μm), which rolled along a circular path (diameter: 33 mm) being pushed by a defined normal load against the rubber sheet. The parameters set for this configuration were: normal load: 90 N, revolution: 280 rpm, duration: 3 hours (h). This device allowed us to record the COF as a function of time.

Sliding friction and wear characteristics were determined in pin (steel)-on-plate (rubber) (POP), roller (steel)-on-plate (rubber) (ROP) and oscillating cylinder (steel) on plate (rubber) (fretting) tribotests.

POP is mounted in a Wazau device (Berlin, Germany), where a steel pin (100Cr6; arithmetical roughness, R_a, less than 1 μm) with a hemispherical head (diameter: 10 mm) rotated along a circular path (diameter: 33 mm). The pin was pushed against the rubber plate with a given load. The following parameters were selected for this configuration – normal load: 2 N, sliding speed: 250 mm/s, duration: 1.5 h. Measuring both the normal and the friction force components via a torque load cell allowed to calculate the COF and its monitoring during the tests.

In ROP, a rotating steel roller (9SMnPb28k, diameter: 10 mm, width: 20 mm, $R_a \approx 0.9$ μm) was pressed against a rubber strip of 8–9 mm width in a SOP 3000 tribotester (Dr Tillwich GmbH, Horb-Ahldorf, Germany). The friction force induced by the torque was measured online and thus also the COF was recorded during the test. The test parameters were load: 2 N; sliding speed: 250 mm/s; duration: 1.5 h.

In the third tribotest (fretting) a steel cylinder oscillated on the surface of the fixed rubber specimen. The cylinder was pushed by a defined normal load against the rubber. The diameter and the contact length of the cylinder ($R_a \approx 0.9$ μm) were 15 and <12 mm (varied), respectively. The applied experimental parameters were: normal load: 10 N, frequency of the oscillation: 10 Hz, stroke: <3 mm (varied), duration: <3 h (varied).

The specific wear rate was calculated according to Equation (1):

$$W_s = \frac{\Delta V}{F \cdot L} \tag{1}$$

where ΔV [mm³] is the volume loss, F [N] is the normal load, L [m] is the overall rolling/sliding distance. The loss volume (ΔV) was calculated by measuring the depth and width of the wear tracks by white light profilometer (see later).

The test set-up of the above testing methods is depicted schematically in Figure 1.

Failure

The worn surfaces were investigated in a Micro-Prof white light profilometer (Fries Research & Technology, Bergisch Gladbach, Germany) and in SEM (JSM-6300 of Jeol, Tokyo, Japan and ZEISS Supra™ 40VP, Oberkochen, Germany). The specimens were sputtered with an Au/Pd alloy in a device of Balzers (Lichtenstein) prior to SEM investigation at high acceleration voltages.

3. Results and discussion

3.1. Network-related properties and hardness

Figure 2 demonstrates the measured storage modulus (E') and loss factor (tanδ) as a function of the temperature changing from –100 to 100°C. The position of the glass transition temperature of the HNBR composites ($T_g \approx -25$°C) was practically not affected by the incorporation and type of the fillers. One can get the impression that introducing fillers in HNBR increased the stiffness in the rubbery stage of the composites, where the MWCNT's effect is much stronger than CB and silica.

Based on the plateau modulus (E_{pl}) at $T = 25$°C the apparent mean molecular mass between crosslinks (M_c) and the network density (v_c) can be calculated by considering the rubber elasticity theory (Equations (2) and (3)):

$$M_c = \frac{3 \cdot \rho \cdot R \cdot T}{E_{pl}} \tag{2}$$

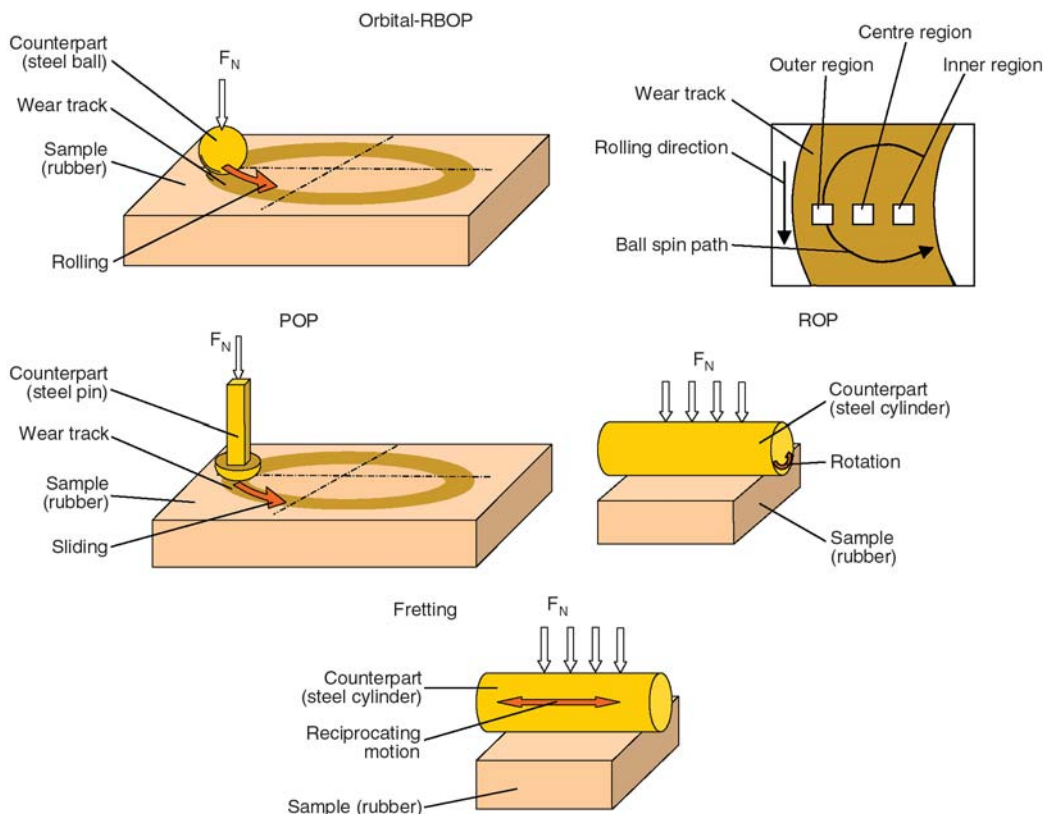$$v_c = \frac{\rho}{M_c} \tag{3}$$

Figure 1. Schemes of the test configurations of Orbital-RBOP, POP, ROP and fretting. This figure also shows the preparation of the samples for SEM investigations after Orbital-RBOP test (top right)

Table 1. Basic network-related properties and hardness of the HNBR compounds studied

	HNBR-PURE	**HNBR-20CB**	**HNBR-20MWCNT**	**HNBR-20ULTRASIL**
M_c [g/mol]	2013	1775	407	1437
v_c [mol/dm³]	0.52	0.61	2.7	0.76
tanδ at T_g	1.37	1.25	0.68	1.02
Density [g/cm³]	1.057	1.091	1.102	1.099
Shore A [°]	42	54	75	56

where E_{pl} is the modulus at the absolute temperature of 298 K, ρ is the density, R is the universal gas constant (8.314 J/(K·mol)), and T is the absolute temperature (i.e. $T = 298$ K).

The apparent M_c and v_c values are listed in Table 1. It is noteworthy that HNBR-20MWCNT has the smallest M_c and accordingly the highest v_c. This reflects that MWCNT had the strongest influence on the rubber-filler and filler-filler interactions and thus possesses the highest reinforcing efficiency (reflected in improved stiffness- and strength-related parameters) among the fillers used. This is likely due to its high aspect ratio and not to some chemical bonding to the rubber matrix.

The Shore A hardness increased when fillers were added in the HNBR. The ranking of the fillers in
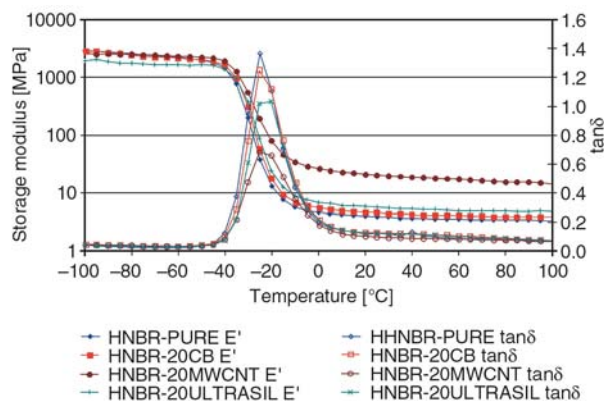
Figure 2. Storage modulus and loss factor tanδ as a function of temperature for the HNBR studied

respect to the hardness enhancement was MWCNT > Ultrasil (silica) > CB.

3.2. Friction and wear

Figure 3 shows the COF and W_s of HNBR with and without fillers measured in Orbital-RBOP (Figure 3a) and POP, ROP, fretting (Figures 3b and c) tests. Results in Figure 3a suggests that incorporation of CB, MWCNT and silica lowered the W_s and slightly enhanced the COF. CB proved to be better in improving the rolling wear resistance of HNBR compared to MWCNT and silica. The low scatter in the COF data under Orbital-RBOP is linked with the related wear mechanisms (see later).

The filled HNBR compounds have smaller W_s in POP and ROP but do not perform better in fretting than HNBR-PURE (cf. Figure 3b). The authors have no explanation for the latter observation. It is noteworthy that the W_s of HNBR-20MWCNT is
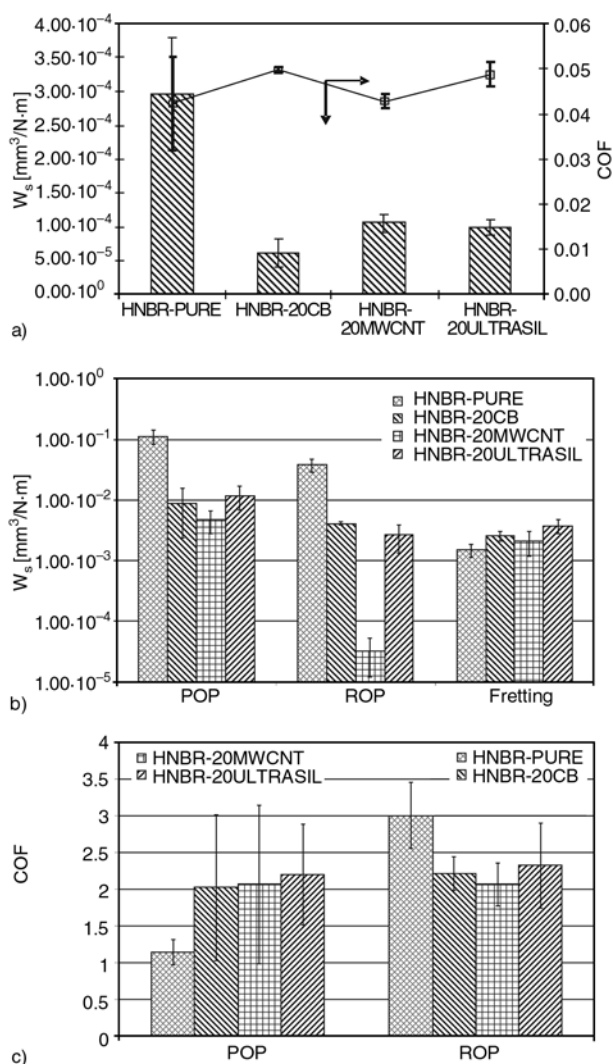
the smallest both under POP and ROP conditions compared to all other HNBR mixes.

Figure 3c shows the steady-state dynamic COF for POP and ROP tests. There are no COF data for fretting because the fretting rig was not able to record COF higher than 1.5. Filled HNBR systems have higher COF than pure HNBR in POP. However, the incorporation of fillers decreased the COF compared to HNBR-PURE under ROP testing. SEM photos reason this phenomenon very well (as shown later). The MWCNT-containing HNBR has the smallest COF compared to HNBR-20CB and -20ULTRASIL in ROP test. It is noteworthy that the above ranking reflects the tendency in the COF, which is underlying to considerable scatter.

It is notable that the best fillers among the used three in respect to rolling and sliding wear resistances are CB and MWCNT, respectively. For the rolling contact, the stress distribution can roughly be estimated by the Hertzian law [16]. As a deviation from the Hertzian law, the maximum stress is often lying beneath the surface and this is responsible for the deterioration and failure of the material (e.g. fatigue induced internal hole formation followed by material spalling). As sliding and rolling contacts are quite different the common reinforcements for rubbery materials to enhance the resistance to sliding wear may not be associated with a similar improvement for rolling wear.

3.3. Failure during rolling and sliding wear

A detailed analysis on the wear mechanisms of pure HNBR in rolling and sliding wear tests can be found in our previous paper [17]. For the sake of comparison selected SEM pictures on the worn surfaces of HNBR-PURE are still inserted in order to facilitate the understanding of the results by the readers.

3.3.1. Rolling wear

Figure 4 shows SEM pictures taken from the rolling wear track of HNBR-PURE. Since the movement of the ball in Orbital-RBOP is guided by a bearing ring, the ball has an additional circumferential rotation (spin). As a result, the wear track may show different features in various regions. This was the reason to divide the track into three regions – cf. Figure 1 [17]. Figures 4a and 4c show the worn surfaces of the regions with additional for-
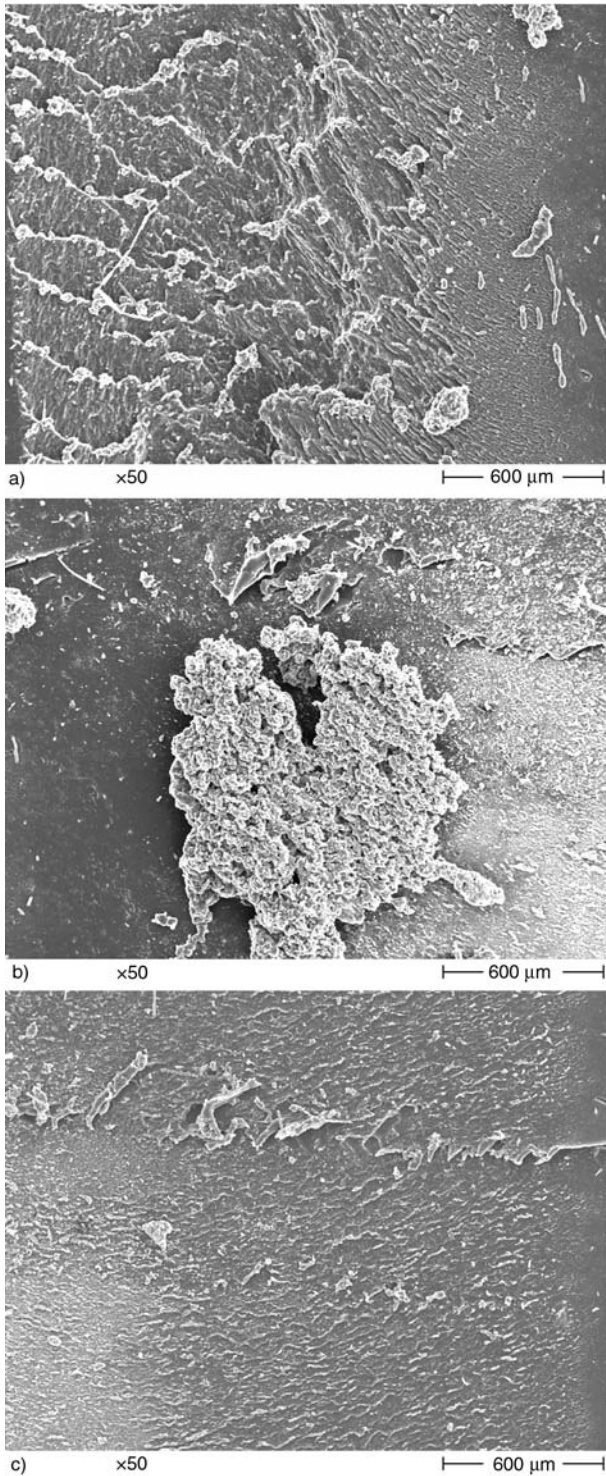

Figure 3. a – W_s (column) and COF (line) after Orbital-RBOP tests, b – W_s after POP, ROP and fretting tests, c – steady-state COF after POP, ROP and fretting tests

Figure 4. SEM photos taken from the rolling wear track of HNBR-PURE after Orbital-RBOP test. a – outer region, b – centre region, c – inner region. Note: rolling direction is downward.
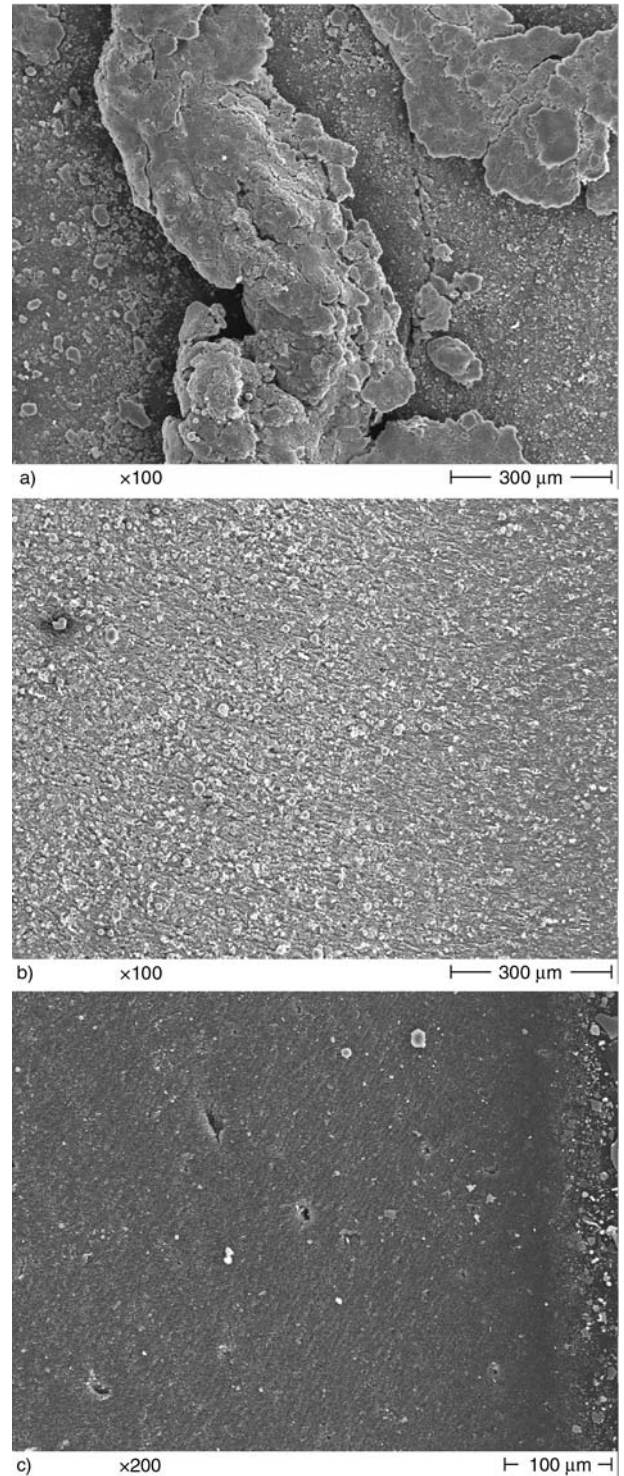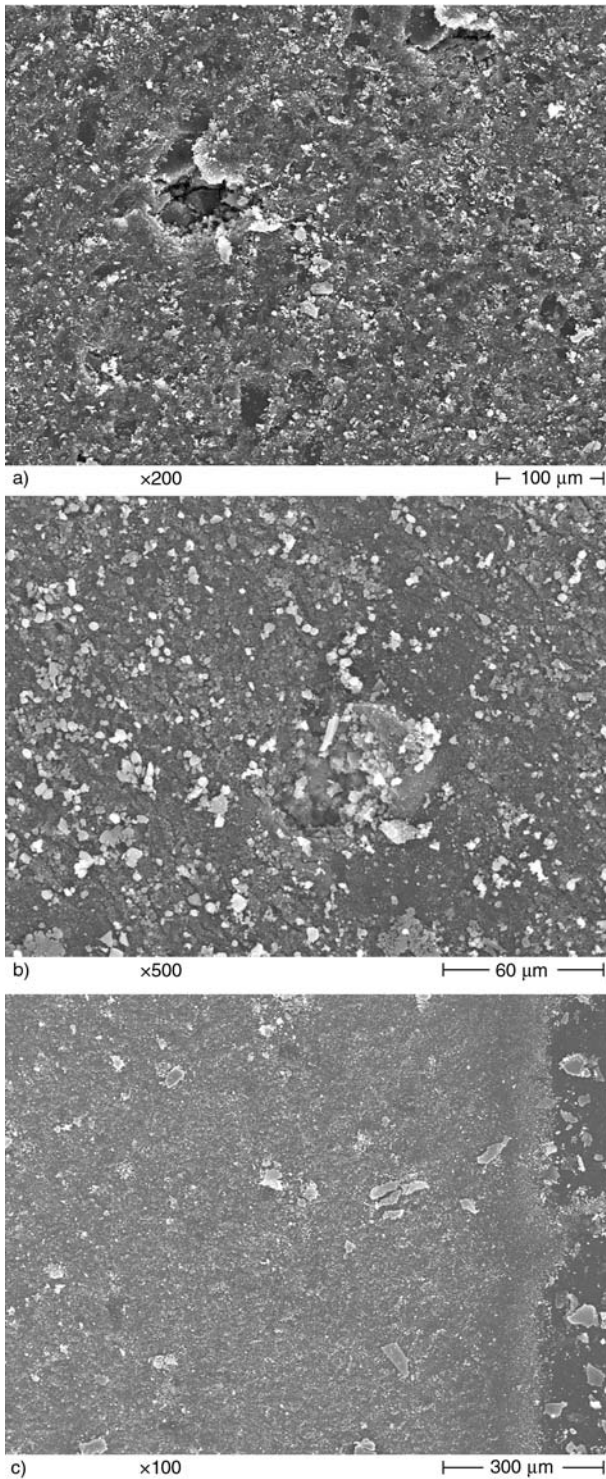

Figure 5. SEM photos taken from the rolling wear track of HNBR-20CB after Orbital-RBOP test. a – outer region, b – centre region, c – inner region. Note: rolling direction is downward.

ward (outer region – cf. Figure 1) and backward spins of the ball (inner region – cf. Figure 1), respectively. Figure 4b is the region between the outer and inner regions (centre region – cf. Figure 1).

Unlike HNBR-PURE (cf. Figure 4), the worn surface of the outer region of HNBR-20CB did not show surface waves, called Schallamach-type pattern, which results from elastic instability caused by the tangential force in the contact region

between the rubber and the steel counterpart (cf. Figure 4a) [18]. The introduction of CB may account for the disappearance of the waves, as often observed in rubbery systems with active fillers [3, 5 and 19]. Instead, large agglomerates appeared in the outer region (cf. Figure 5a). Frag-

mentation of debris is the wear characteristic in the centre region (cf. Figure 5b). Fatigue induced hole formation can be found in the inner region of the wear track (cf. Figure 5c). Recall that their onset is owing to spalling events.

Figure 6. SEM photos taken from the rolling wear track of HNBR-20MWCNT after Orbital-RBOP test. a – outer region, b – centre region, c – inner region. Note: rolling direction is downward.
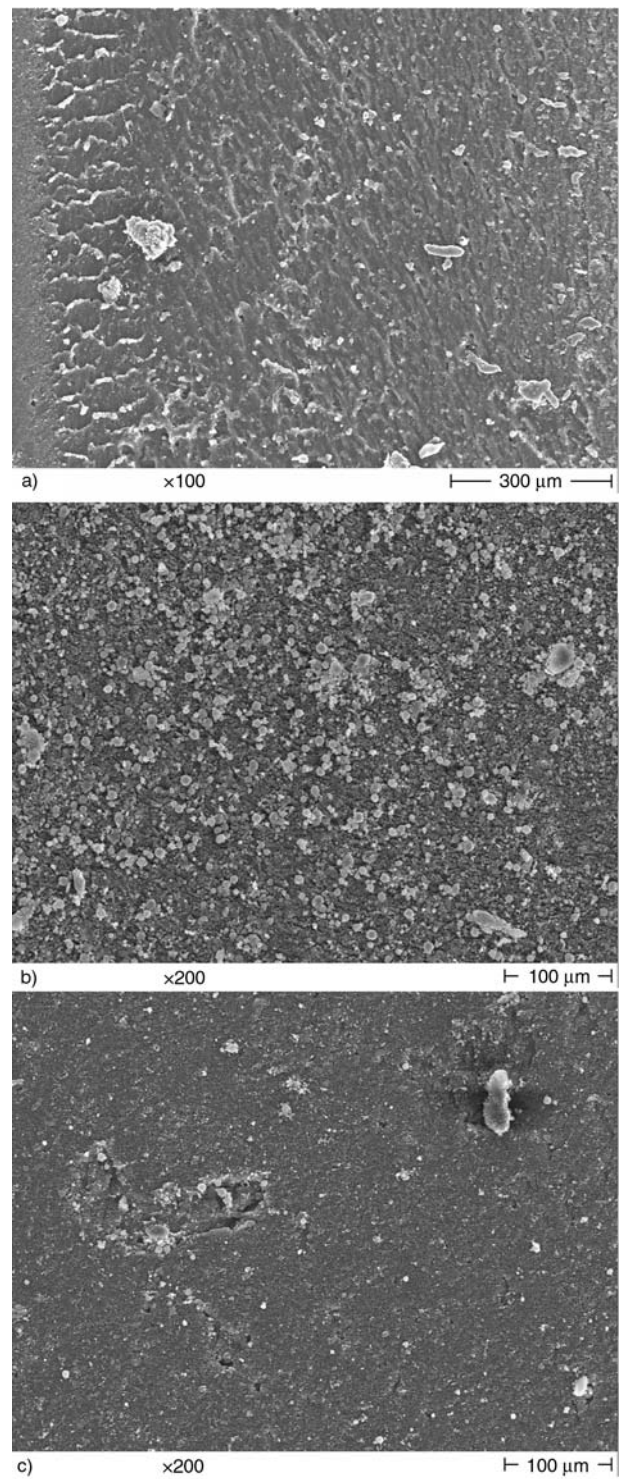
Figure 7. SEM photos taken from the rolling wear track of HNBR-20ULTRASIL after Orbital-RBOP test. a – outer region, b – centre region, c – inner region. Note: rolling direction is downward.

Figure 6 collects SEM photos taken from the three regions of the wear track of MWCNT reinforced HNBR. Fatigue induced-spalling and fragmentation are the main wear mechanisms in the outer and centre regions (cf. Figures 6a and 6b). In the inner region, flattened debris scatter over the whole area (cf. Figure 6c).

Figure 7 displays the worn surface of HNBR-20ULTRASIL. In the outer region, Schallamach pattern with roll head, flat particles and agglomerates are discernible (cf. Figure 7a). Fragmentation is the main wear mechanism in the centre region (cf. Figure 7b). 'Ironed' particles and holes due to fatigue can be observed in the inner region of the worn surface (cf. Figure 7c).

By reviewing Figures 4–7, it is noticable that the Schallamach-type pattern disappeared completely or the area of its onset narrowed when the HNBR was filled. This change in the wear mechanisms is in line with the reduced specific wear rate observed for the filled HNBR mixes (cf. Figure 3a). The debris and fragmented surface in the center region of the wear track of filler containing compounds result likely in higher COFs compared to HNBR-PURE.

3.3.2. Sliding wear

Figure 8 shows SEM photos of the worn surfaces of the HNBR compounds after POP tests. HNBR-20CB and -20ULTRASIL show abrasion type pattern with fragments (cf. Figures 8b and 8d). Note that they have very similar W_s and COF values (cf. Figures 3b and 3c). This suggests that the CB and ULTRASIL have similar reinforcing effects in the HNBR. By contrast, HNBR-PURE failed by crater formation (to show this phenomenon a high magnification SEM picture has been selected). When MWCNT was added in HNBR, rolled debris, holes and an elongated fibrillar structure appeared which dominated the whole worn surface (cf. Figure 8c).
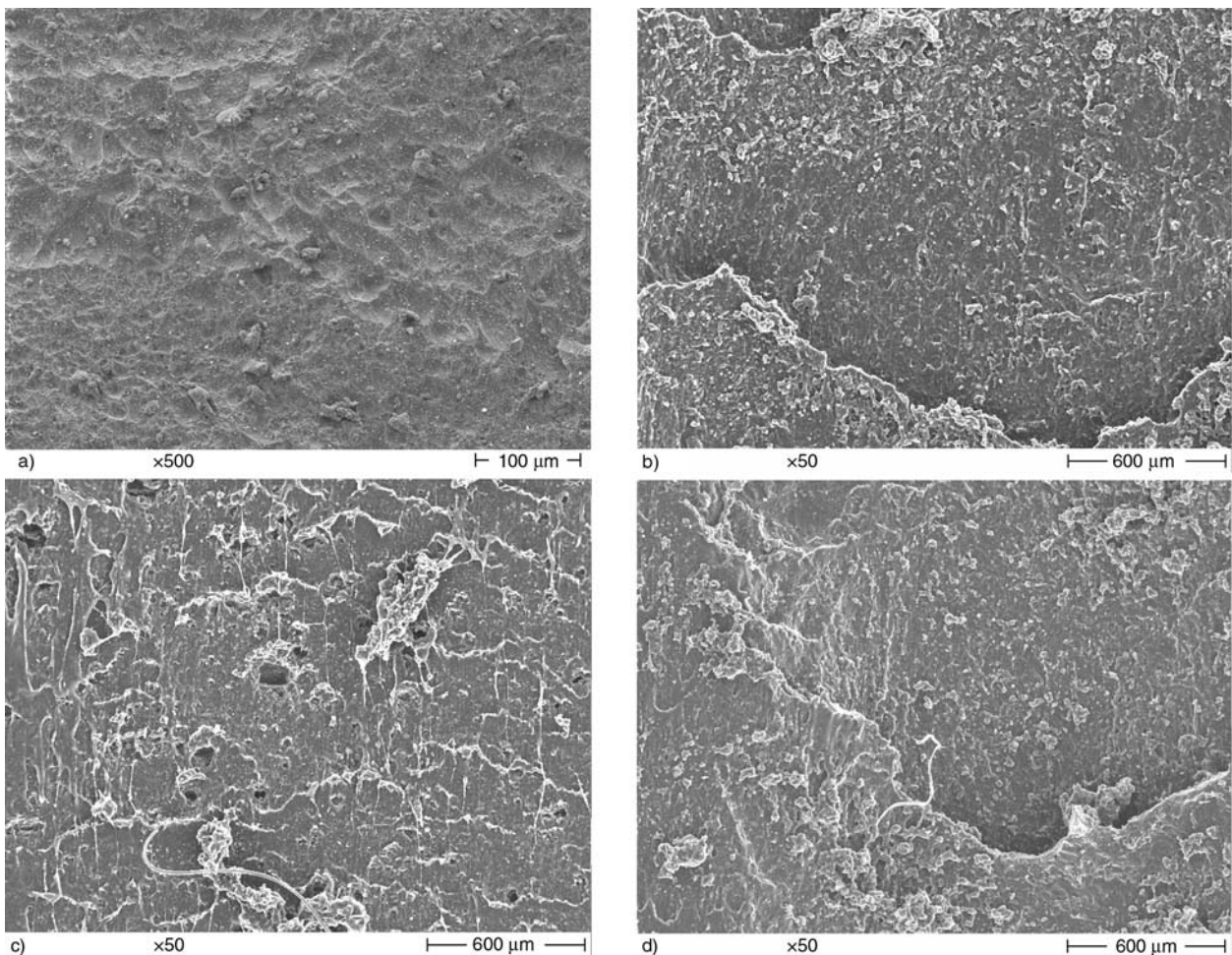

Figure 8. SEM photos taken from the worn surfaces of HNBR-PURE (a), -20CB (b), -20MWCNT (c) and -20ULTRASIL (d) after POP tests. Note: sliding direction is downward.
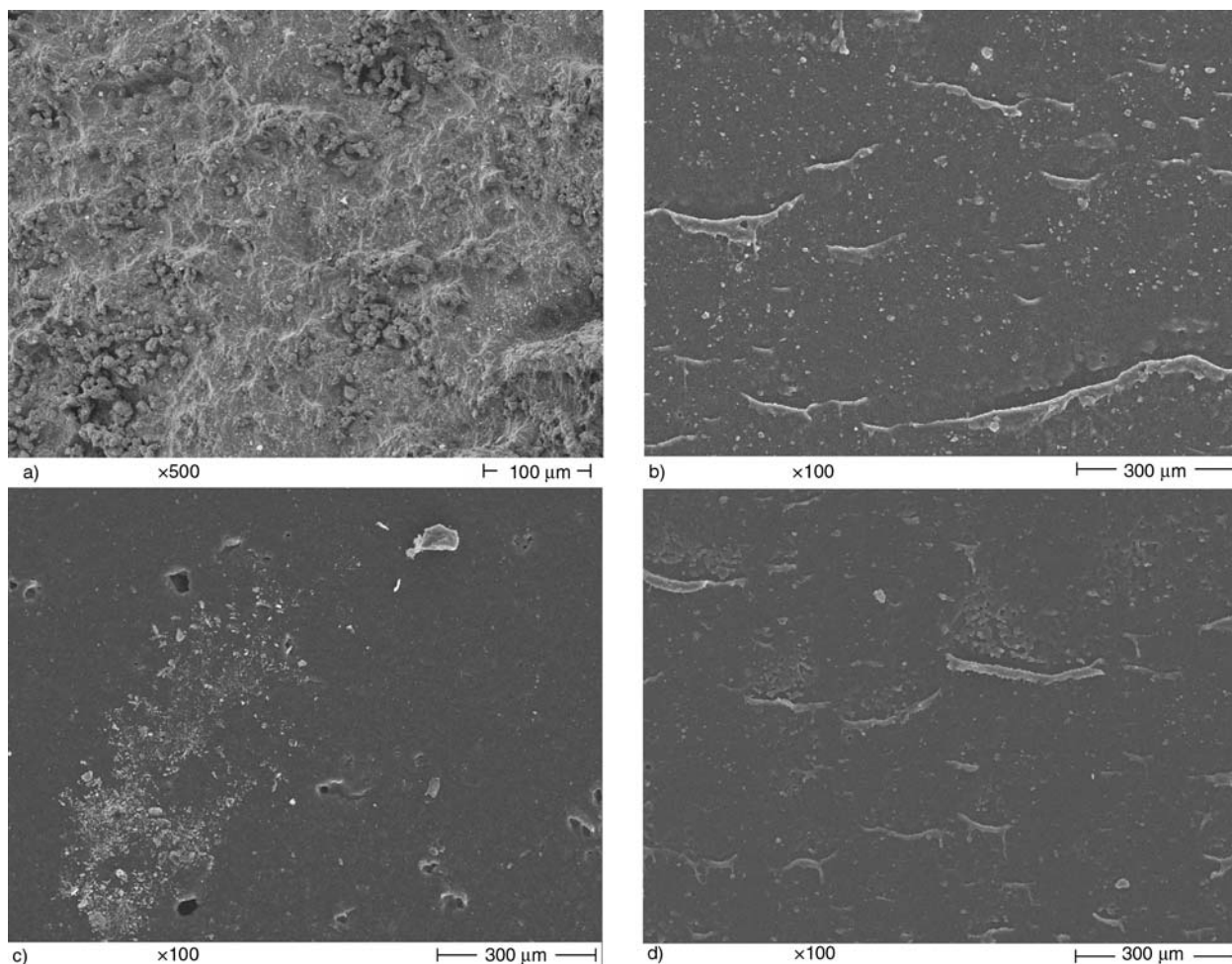
Figure 9. SEM photos taken from the worn surfaces of HNBR-PURE (a), -20CB (b), -20MWCNT (c) and -20ULTRASIL (d) after ROP tests. Note: sliding direction is downward.

The worn surfaces of HNBR without and with active fillers (CB, MWCNT and silica) after ROP tests are displayed in Figure 9. CB and silica reinforcements of HNBR produce similar worn surfaces, where slightly extended and 'ironed' rolling stripes can be observed (cf. Figures 9b and 9d). This similarity in the wear mechanisms is reflected in similar W_s and COF data of HNBR-20CB and -20ULTRASIL in ROP. The failure scenario is different for HNBR-20MWCNT (cf. Figure 9c) in which small particles and holes are found on the ROP worn surface .This may hint for some reorganization of the MWCNT at the interface under ROP conditions. However, this speculative explanation has to be checked by further testing.

In fretting tests, peeling is the common predominant wear mechanism for all three filled HNBR compounds (cf. Figure 10). However, HNBR-20MWCNT has some unique feature due to hole formation in the peeling-type wear track (cf. Fig-

ure 10c). HNBR-PURE fails by crating also under fretting (cf. Figure 10a).

Like for rolling wear, the change of the wear mechanisms is in line with the observed changes in the specific wear rates. Note that similar wear mechanisms result in similar wear losses, i.e. the related W_s values are well matched. The higher (POP) and lower (ROP) COFs of the filled HNBRs is most likely due to the rougher (POP) and smoother (ROP) surfaces produced.

4. Conclusions

HNBR compounds with 20 phr various active fillers (CB, MWCNT and silica) was investigated by different rolling and sliding wear testing configurations under dry condition. The network-related apparent characteristics of the HNBR compounds were deduced from DMTA measurements. The COF and W_s were determined and the wear mecha-
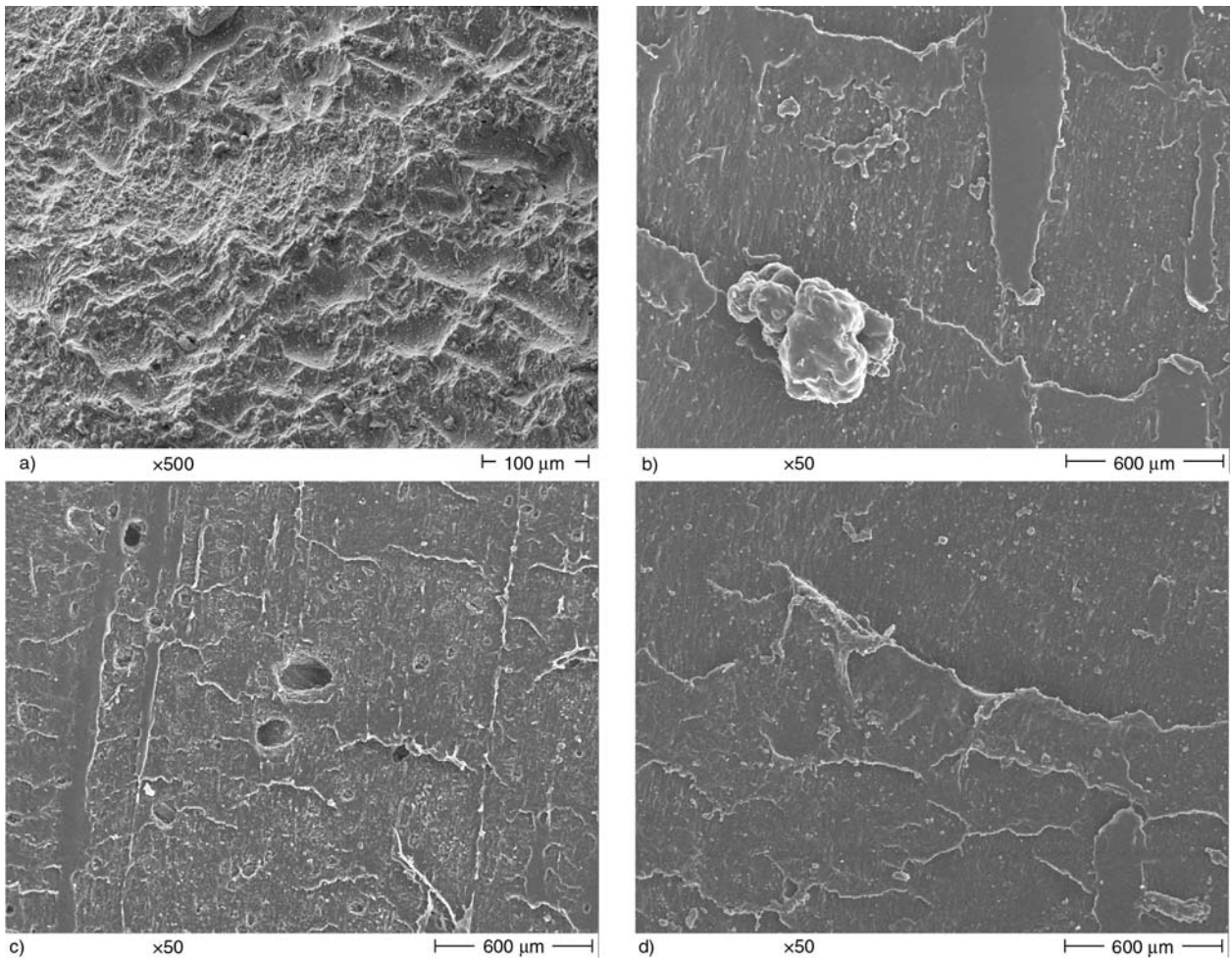
Figure 10. SEM photos taken from the worn surfaces of HNBR-PURE (a), -20CB (b), -20MWCNT (c) and -20ULTRASIL (d) after fretting tests. Note: sliding direction is vertical.

nisms under rolling and sliding conditions were identified. Results of this research work can be concluded as follow:

– MWCNT had the strongest reinforcing effect and thus the most pronounced influence on the rubber-filler and filler-filler interactions among the fillers used.

– CB- and MWCNT-containing HNBR compounds exhibited the best resistance to rolling and sliding wear, respectively. This was attributed to a difference in the stress distributions during rolling and sliding contacts causing pronounced changes in the wear mechanisms, which themselves depend on type and characteristics of the filler used.

– CB and silica have similar effects in respect to the sliding wear behavior (POP, ROP and fretting) when considering the corresponding W_s, COF data and wear mechanisms.

– Fatigue-induced hole formation is the unique characteristic for the sliding wear mechanisms of HNBR-20MWCNT. This may be linked with a weaker resistance of HNBR-20MWCNT to fatigue and with an eventual reorganization of the MWCNT at the sliding interface. This phenomenon, behind which MWCNT agglomeration is suspected, needs further investigation.

Acknowledgements

References

[1] Wang M. J.: Effect of filler-elastomer interaction on tire tread performance part III. Kautschuk Gummi Kunststoffe, **61**, 159–165 (2008).

[2] Xiong J., Zheng Z., Qin X., Li M., Li H., Wang X.: The thermal and mechanical properties of a polyurethane/multi-walled carbon nanotube composite. Carbon, **44**, 2701–2707 (2006).
DOI: 10.1016/j.carbon.2006.04.005

[3] Xu D., Karger-Kocsis J., Schlarb A. K.: Rolling wear of EPDM and SBR rubbers as a function of carbon black contents: Correlation with microhardness. Journal of Materials Science, **43**, 4330–4339 (2008).
DOI: 10.1007/s10853-008-2637-7

[4] Nayek S., Bhowmick A. K., Pal S. K., Chandra A. K.: Wear behavior of silica filled tire tread compounds by various rock surfaces. Rubber Chemistry and Technology, **78**, 705–723 (2005).

[5] Karger-Kocsis J., Mousa A., Major Z., Békési N.: Dry friction and sliding wear of EPDM rubbers against steel as a function of carbon black content. Wear, **264**, 357–365 (2008).
DOI: 10.1016/j.wear.2007.03.021

[6] Choi S-S., Park B-H., Song H.: Influence of filler type and content on properties of styrene-butadiene rubber (SBR) compound reinforced with carbon black or silica. Polymers for Advanced Technologies, **15**, 122–127 (2004).
DOI: 10.1002/pat.421

[7] Wei Z., Zhao Y-P., Ruan S. L., Gao P., Yu T. X.: A study of the tribological behavior of carbon-nanotube-reinforced ultrahigh molecular weight polyethylene composites. Surface and Interface Analysis, **38**, 883–886 (2006).
DOI: 10.1002/sia.2148

[8] Chen H. Y., Jacobs O., Wu W., Rudiger G., Schädel B.: Effect of dispersion method on tribological properties of carbon nanotube reinforced epoxy resin composites. Polymer Testing, **26**, 351–360 (2007).
DOI: 10.1016/j.polymertesting.2006.11.004

[9] Enomoto K., Yasuhara T., Kitakata S., Murakami H., Ohtake N.: Frictional properties of carbon nanofiber reinforced polymer matrix composites. New Diamond and Frontier Carbon Technology, **14**, 11–20 (2004).

[10] Wang C., Dong B., Gao G-Y., Xu M-W., Li H-L.: A study on microhardness and tribological behavior of carbon nanotubes reinforced AMMA-CNTs copolymer nanocomposites. Materials Science and Engineering: A, **478**, 314–318 (2008).
DOI: 10.1016/j.msea.2007.06.036

[11] Chen W. X., Li F., Han G., Xia J. B., Wang L. Y., Tu J. P., Xu Z. D.: Tribological behavior of carbon-nanotube-filled PTFE composites. Tribology Letters, **15**, 275–278 (2003).
DOI: 10.1023/A:1024869305259

[12] Du J. H., Bai J., Cheng H. M.: The present status and key problems of carbon nanotube based polymer composites. Express Polymer Letters, **1**, 253–273 (2007).
DOI: 10.3144/expresspolymlett.2007.39

[13] Song H-J., Zhang Z-Z., Men X-H.: Surface-modified carbon nanotubes and the effect of their addition on the tribological behavior of a polyurethane coating. European Polymer Journal, **43**, 4092–4102 (2007).
DOI: 10.1016/j.eurpolymj.2007.07.003

[14] Thavamani P., Bhowmick A. K.: Abrasion of swollen rubber vulcanizates. Plastics Rubber and Composites Processing and Applications, **18**, 35–45 (1992).

[15] Thavamani P., Bhowmick A. K.: Influence of compositional variables and testing temperature on the wear of hydrogenated nitrile rubber. Journal of Materials Science, **28**, 1351–1359 (1993).
DOI: 10.1007/BF01191977

[16] Sarkar A. D.: Friction and wear. Academic Press, London (1980).

[17] Felhős D., Karger-Kocsis J., Xu D.: Tribological testing of peroxide cured HNBR with different MWCNT and silica contents under dry sliding and rolling conditions against steel. Journal of Applied Polymer Science, **108**, 2840–2851 (2008).
DOI: 10.1002/app.27624

[18] Schallamach A.: How does rubber slide? Wear, **17**, 301–312 (1971).

[19] Felhős D., Karger-Kocsis J.: Tribological testing of peroxide-cured EPDM rubbers with different carbon black contents under dry sliding conditions against steel. Tribology International, **41**, 404–415 (2008).
DOI: 10.1016/j.triboint.2007.09.005